論文 / 著書情報
Article / Book Information

題目(和文)	
Title(English)	Joint Optimization of Structure and Control for Fully Actuated UAVs Based on Value Function Minimization
著者(和文)	田所祐一
Author(English)	Yuichi Tadokoro
出典(和文)	学位:博士(工学), 学位授与機関:東京工業大学, 報告番号:甲第11423号, 授与年月日:2020年3月26日, 学位の種別:課程博士, 審査員:三平 満司,藤田 政之,井村 順一,山北 昌毅,早川 朋久
Citation(English)	Degree:Doctor (Engineering), Conferring organization: Tokyo Institute of Technology, Report number:甲第11423号, Conferred date:2020/3/26, Degree Type:Course doctor, Examiner:,,,,
学位種別(和文)	博士論文
Type(English)	Doctoral Thesis

東京工業大学
Tokyo Institute of Technology

Doctoral Dissertation

Joint Optimization of Structure and Control for Fully Actuated UAVs Based on Value Function Minimization

Supervisor: Professor Mitsuji Sampei

Tokyo Institute of Technology
School of Engineering
Department of Systems and Control Engineering

Yuichi Tadokoro

February, 2020

Abstract

Joint Optimization of Structure and Control for Fully Actuated UAVs Based on Value Function Minimization

Supervisor: Professor Mitsuji Sampei

This dissertation investigates a joint optimization scheme of the structure and control for fully actuated unmanned aerial vehicles that can achieve general motion in 3-dimensional space. The control performance such as energy consumption and settling time is heavily affected by both the control law and the plant parameters of the controlled object. However, regular optimal control problems consider optimization only over the control input and fail to utilize the plant parameters to further improve the performance. Given this problem, the objective of this work is to simultaneously acquire both the optimal control input and optimal plant parameters that minimize an objective function. To achieve this goal, the optimal value function, which corresponds to the minimum cost of optimal control, is reinterpreted and further minimized as a function of plant parameters. This method is called "joint optimization" of the structure and control as the two optimization problems are connected via the same objective function. Both analytical and numerical methods are developed in this work, and they can be used to determine the optimal plant parameters for different control tasks, which are specified by the objective function and the set of initial states.

First, a fully actuated hexarotor is introduced as the main application of joint optimization in this dissertation. A fully actuated hexarotor has six rotors fixed on its body, and they are tilted so that the vehicle can generate force and torque in every direction and around every axis. The vehicle dynamics is modeled based on aerodynamics and rigid body dynamics, and the model is then transformed into a second-order system on the special Euclidean group $SE(3)$. A theorem shows that nonplanar structures can be transformed into planar structures without changing the force and torque acting on the center of mass. This property greatly simplifies the subsequent discussion because considering only planar structures is sufficient for the analysis of the force and torque. Moreover, related research is classified by using this simplification method, and it is shown that there exist two standard classes of fully actuated hexarotors. To measure the full-actuation performance, the dynamic manipulability of hexarotors is then defined and analyzed for the two classes of hexarotors. Theorems prove that the dynamic manipulability is suitable for the evaluation of directional characteristics of acceleration. It is suggested that the structural design of the hexarotor should be considered with its control task because the acceleration characteristics change according to the position and orientation of rotors. An overview of the experiment system is given, and a preliminary experiment is also conducted.

Secondly, an analytical method for joint optimization is presented based on an analytical optimal controller for rigid body dynamics. Before developing the optimal control method, a double-geodesic PD controller on $SE(3)$ is described, which provides the basis of the optimal controller. The closed-form solution of the optimal control input and the corresponding value function are then shown for the cases where the vehicle is under zero gravity or the force of gravity is compensated by an input transformation. Theorems prove the optimality of the present control law and stability of the closed-loop system via the Hamilton-Jacobi-Bellman equation and the Lyapunov theorem. An analogy to linear optimal control is also given. The analytical value function is then minimized with respect to the plant parameters. An application to a fully actuated hexarotor shows that the optimal design for nongravity cases corresponds to the maximization of the dynamic manipulability, and it is validated also by simulations.

Finally, a numerical method for joint optimization is studied to consider more general dynamics and objective functions. In particular, we tackle the application to a fully actuated hexarotor considering the input energy cost for gravity compensation. A nonlinear model predictive control method is proposed based on an exact discretization of the rigid body dynamics using a geometric integrator via the Cayley map for $SE(3)$. The exact discretization allows picking a coarse sampling period without losing the precision of the integrated dynamics. Moreover, the recursive discretization technique is combined with the geometric integrator to drastically reduce the computational effort of optimization. On-board simulations of flight control show that the present numerical optimal control method runs on a low-cost single-board computer in real time while considering the gravity compensation cost. An experiment using the fast model predictive controller further validates the effectiveness of the proposed method. The numerical controller is then reused to calculate the value function for the specified plant parameters and initial states. Parameter optimization of rotor tilt angles is then carried out by using particle swarm optimization so that the simulated value function is minimized to the nearly-global optimum. The result shows that the fast numerical control method not only provides a real-time controller but also is meaningful for reducing the computation time of the parameter optimization. It is also demonstrated that parameter optimization based on dynamic manipulability maximization is not energy-efficient when considering the cost of gravity compensation.

Acknowledgment

I would like to express my deepest gratitude to my supervisor, Prof. Mitsuji Sampei, for his guidance. His extensive knowledge in related control problems was instrumental for this dissertation. As a supervisor, he has given me insightful suggestions to make this work more complete. His balanced thought between academic and practical work encouraged me determining the direction of this research. Also, I would like to thank him for teaching me the importance of thinking widely while deepening ideas.

I am indebted to Dr. Tatsuya Ibuki for his unrelenting support and advice in every stage of the research process. In particular, he introduced me to the interesting field of geometrical methods for rigid body systems in which I decided to be specialized. Co-working with him was also instrumental in improving my presentation and writing skills.

Special appreciation is due to the secretary of our laboratory, Ms. Yoko Nishiyama, for her valuable support in daily research activities. Many thanks to my colleagues for having many technical discussions that helped me to better understand the related theory and technologies. Thanks also to my friends for having good times together.

Finally, I would like to thank my whole family for their love and for always caring about me. I must thank my parents who have supported me both mentally and financially. I am proud of my brother who has frequently discussed technical topics with. His eagerness to learn encouraged me a lot, and I truly feel fortunate to have a brother like him. I would also like to thank my grandparents who have always shown empathy for me and shared my pleasure. Without them, I would not have been able to continue my research work in the hardest time.

Contents

List of Figures

List of Tables

Chapter 1

Introduction

1.1 Motivation

The aging society has been becoming a serious problem for developed countries. According to the government, the labor force population in Japan is steadily decreasing, and the active population in 2050 is estimated to be approximately only half of the overall population [1]. The number of people who maintain the existing infrastructures will also decrease, which would cause occupational safety problems. For example, inspection and maintenance of high-rise buildings or power lines are dangerous labors that may put the workers at risk of falling. It is reported that the most common cause of fatal occupational injuries in Japan is the fall accident [2]. To prevent such tragedies and to achieve a sustainable society, it is important to assist or automate these hazardous tasks by technology.

Multirotor unmanned aerial vehicles (UAVs), also widely known as "drones", are expected to help to solve this issue because of their ability to hover, the high dynamical performance, and the affordable price. However, the standard type of UAV is underactuated, i.e., the horizontal force cannot be generated without tilting the body, and this property limits the application of UAVs. To overcome this problem, fully actuated UAVs are studied recently. Fully actuated UAVs attract academy and industry as a versatile platform for 3-dimensional physical interaction with environments. The vehicle has at least 6 rotors, actuators that consist of electric motors and propellers, fixed on the body, and they are tilted so that the vehicle can accelerate in every direction and around every axis. Throughout this dissertation, we consider the design and control of a fully actuated UAV.

The design and control of a dynamical system are tightly coupled through the system model because the both affect control performance such as energy consumption and settling time. However, regular control problems consider optimization of the control performance only over the control input, and they fail to utilize the plant parameters for the further improvement. This is because optimal control problems assume that the design of the plant should be performed prior to the control design. Given this problem, we suggest that the

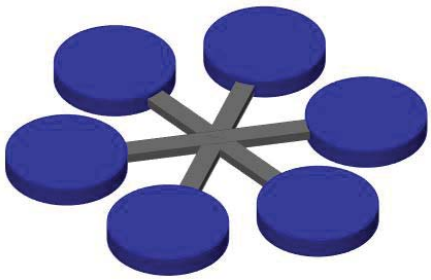

Fig. 1.1: Parallel hexarotor. This structure cannot exert direct force in horizontal directions.

design of the controlled object should be determined by the control objectives, and thus we tackle optimization of structure and control in this dissertation.

The objective of the optimization is to simultaneously acquire both the optimal control input and optimal plant parameters that minimize an objective function. To achieve this goal, we reinterpret and minimize the value function of the optimal control problem as a function of plant parameters. This method is called "joint optimization" of structure and control because the two optimization problems are connected via the same objective function. In this dissertation, we consider the cases where the task specifications of control are described with an objective function and the set of initial states, and we aim to obtain the optimal structure and control suited to the specifications. We develop both analytical and numerical optimal control methods for rigid body dynamical systems, and the minimum cost will be further minimized with respect to the plant parameters, which yields the optimal plant and controller simultaneously.

What makes it important to consider the structural optimization of the fully actuated UAV is that the acceleration properties vary according to the structure of the vehicle. Specifically, the positions and orientation of the rotors are the key parameters of the directions in which the vehicle can accelerate with less energy consumption. When considering different types of tasks, the directions in which the vehicle is "good at" accelerating should be chosen differently. For example, aerial transportation needs larger capacity of payloads than other applications. On the other hand, an aerial vehicle should be robust against horizontal external force when it performs a building inspection task. This structural design problem motivates our work, and will be tackled in the subsequent discussions.

1.2 Background and Literature Review

1.2.1 Fully Actuated Multirotor UAV

Multirotor UAVs are increasingly utilized as inexpensive equipments for industrial applications such as environment monitoring [3] and building inspection [4]. Compared to conventional unmanned helicopters, they are light-weight and mechanically simple, and thus they attract many researchers and engineers in this decade. One of the primal challenges for multirotor UAVs is aerial manipulation. The multirotors are equipped with robotic arms for control tasks such as assembly [5] and perching [6]. However, it is known that conventional parallel multirotors, such as one shown in Fig. 1.1, are not suitable for object manipulation because they cannot generate force horizontally without tilting the body. In order to compensate for the body angles, they have to carry additional actuators for their manipulator arms. Moreover, parallel multirotors lack the wind disturbance rejection performance for the same reason, which makes it difficult to conduct outdoor tasks. Since the demands for aerial manipulation are increasing, as tackled by [5] and [7], it is important for vehicles to be able to generate horizontal force without changing the attitude.

To achieve this ability, alternative types of the UAV structures are proposed in [8–20]. There, multi-rotor UAVs with 6 rotors called hexarotor are considered, and their rotor arrangement and tilt angles are changed from the typical hexarotor structure. For example, Toratani [10] suggests a nonplanar structure shown in Fig. 1.2(a), and Kaufman et al. [17] present a nonparallel structure in Fig. 1.2(b). This makes the hexarotors fully actuated; all the 6 degrees of freedom associated with the translational and rotational motion become independently controllable. A geometric control method and the experimental result are reported by Ryll et al. [21], and it is shown that the full-actuation property brings advantages in interaction tasks. These kinds of structures, however, have been found heuristically, and it is thus difficult to explain which type of the structure is suitable for a specific application.

A systematic approach to obtain a suitable structure is a design optimization scheme. Various methods for hexarotor UAV design optimization have been tackled recently. Kiso et al. [22] present a structural design optimization method for a certain class of hexarotor UAVs using the maximum acceleration and the dynamic manipulability as the performance index of the vehicle. Rajappa et al. [12] minimize control effort by using numerical simulations for a predefined reference trajectory to design the optimal structure. Mehmood et al. [14] insist that the maximum translational and rotational acceleration should be optimized, and they numerically solve the optimization problem subject to some constraints on the rotor thrust force. In these articles, however, the rotor arrangement is not considered, and they end up treating a very limited class of the hexarotor structure. Furthermore, they show only numerical results for certain parameters, and no analytical or physical explanation of optimality is explicitly given.

In the author's previous research, we have presented the analysis of the hexarotor struc-

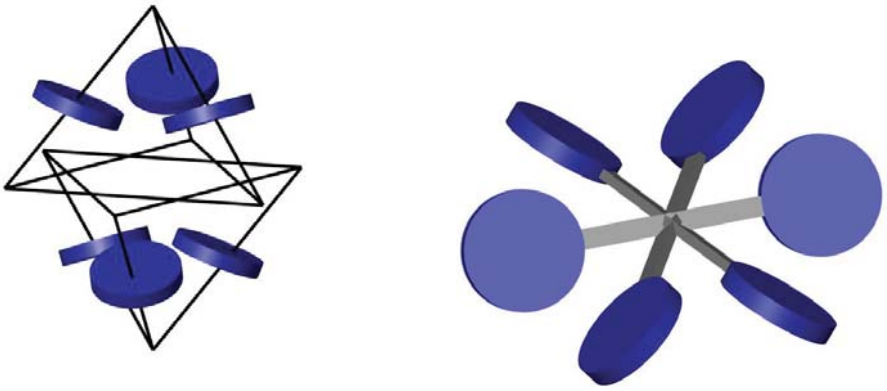

(a) (b)

Fig. 1.2: Example of nonregular hexarotor structure. (a) The rotors are tilted symmetrically and placed on the edges of a double-tetrahedron [10]. (b) The structure is planar and the rotors are tilted in a symmetric manner [17].

ture and a design optimization method using the dynamic manipulability measure [23] and dynamic manipulability ellipsoid [24]. In [25], we have also shown that the many structures from related research can be classified into two special classes of the hexarotor based on the analysis of the dynamical model. This dissertation uses the results shown in these papers to motivate the application of the joint optimization scheme of the structure and control.

1.2.2 Optimal Control of Rigid Body Motion

To control the mobile robot systems such as a fully actuated UAV, we need to consider control methods tailored for rigid body kinematics and dynamics. The rigid body motion is described with a dynamical model in the special Euclidean group $SE(3)$. The dynamics must be constrained on the group, and thus we need to consider specific control laws to achieve regulation and tracking. For example, [26] presents coordinate-free geometric proportional-derivative (PD) controllers on $SE(3)$ and its subgroup $SO(3)$, the special orthogonal group, based on the metrics defined on the groups. Lee et al. [27] study a trajectory tracking controller of a quadrotor aerial vehicle on $SE(3)$ using an intrinsic attitude tracking error defined in $SO(3)$. Such a control strategy can also be applied to optimal control problems. Examples from [28] and [29] consider the cost of control input for continuous-time kinematic systems on Lie groups. Lee et al. [30] tackle an optimal control problem of a discrete-time kinematic system on $SO(3)$. Liu et al. [31] show an analytic solution of a quadratic optimal control problem on a compact Lie group such as $SO(3)$ by using the logarithm map. The author of this dissertation has presented an analytic optimal control method for $SE(3)$ considering a quadratic objective function with specific weight matrices [32]. It utilizes the double-geodesic PD controller by Bullo and Murray [33] to obtain an analytical solution of the optimal control problem on $SE(3)$. It also shows an application of the control of a fully actuated hexarotor aerial vehicle, which can be identified with a fully actuated rigid body.

In general, however, it is difficult to solve optimal control problems analytically. For example, [32] cannot consider external force such as the force of gravity, and the objective function is limited to a certain form. Hence, we need numerical methods if we consider constraints or complex objective functions. The key to numerical optimal control for rigid body motion is proper discretization of the dynamics constrained on Lie groups. The simplest possible way of discretization is a forward Euler approximation in a vector space [34]. Although this approach can be sufficient for many other cases, it is not recommended for rigid body systems because the Lie group structure is not preserved after the integration. In related research [35–37], geometric integrators are used to overcome this problem. Lee et al. [35] investigate structure-preserving optimal control of discrete-time rigid body systems. They propose a computational approach based on a Lie group variational integrator (LGVI) and Newton methods to solve a minimum-energy control problem. Kobilarov and Marsden [36] study a generalized method of LGVI-based discrete optimal control for both fully actuated and underactuated systems on any Lie group. In these studies, conditions regarding the variational principle and optimality are combined into a system of nonlinear equations, and the optimal control problem becomes equivalent to a nonlinear root-finding problem. However, LGVI-based optimal control methods usually require optimization over both states (or costates) and inputs. This results in a larger-scale problem that can be intractable on embedded controllers in real time due to the curse of dimensionality. Moreover, these methods are only concerned with minimum-energy control problems where the objective function is limited to the total of the squared input norms.

For the purpose of developing a more versatile optimal control method for free-floating mobile robots such as spacecraft or fully actuated hexarotors [25], we adopt nonlinear model predictive control (NMPC) with a geometric integrator. In particular, we focus on fast computation of NMPC for embedded controllers in real time. To develop such a numerical optimal control method, we need to reduce the number of decision variables while preserving the Lie group structure. Instead of optimizing the sequence of both states and inputs, we employ the so-called recursive discretization technique [38, Chapter 10] to eliminate states from the decision variables. To apply the technique, we use a geometric integrator based on the Cayley map for $SE(3)$ [37, 39] instead of an LGVI. The geometric integrator with the Cayley map preserves the Lie group structure, and it enables us to pick a coarse sampling interval for the prediction and to reduce the number of decision variables. Next, we calculate the analytic gradient of the objective function with respect to the sequence of inputs, exploiting the sparsity of intermediate Jacobian matrices. The novel usage of the geometric integrator together with the recursive discretization technique reduces the computational effort while maintaining the precision of the predicted trajectory.

The contribution is notable because this work includes a real-time on-board NMPC experiment for an aerial vehicle system that has fast dynamics and inherent instability. In fact, many NMPC schemes for mobile robot systems presented in [36, 40–43], for example,

show that various control objectives are achieved but have no experimental validations. Moreover, experiments of NMPC usually employ high-performance processors, e.g. Intel Core i7 CPUs, for calculation on the ground [44–46]. To the author's knowledge, there are only a few exceptions such as a study on NMPC for aerial manipulation using an aerial vehicle [47] and their later work on obstacle avoidance control [48]. Although they perform experiments with NMPC computation on an embedded computer, the optimal control law is used to generate the reference trajectory, and it is not used for real-time control. In this dissertation, on the other hand, we tackle real-time control of such an unstable system with an NMPC running on an embedded controller. Furthermore, we use the fast optimal control method to simulate the optimal trajectory and to calculate its minimal cost, and we determine the optimal hexarotor structure for different control tasks by minimizing the cost with respect to the plant parameters.

1.2.3 Simultaneous Design of Structure and Control

For typical design of mechanical systems, we usually design the plant parameter and control separately. However, it is not often considered whether the designed structure is suitable for the designed control law and vice versa. Since the performance evaluation is not shared among the structural and control designs in many cases, there possibly exist suboptimality problems caused by trade-offs between the design and control.

This problem is a classical problem in the field of vibration control of flexible structures, as discussed in [49–55]. These studies usually deals with linear time-invariant systems, and thus they consider frequency-domain characteristics such as poles and zeros [51, 53] or closed-loop $\mathcal{H}_2$ and $\mathcal{H}_\infty$ norms [54]. These methods expect the plant parameters to maximize the easiness of control rather than to suit a specific task. On the other hand, several studies minimize costs of optimal control such as linear quadratic regulation [50, 55] and minimum time control [52]. These methods can be considered as task-oriented methods, which optimize the actual performance for the specified tasks. In [50], a linear combination of the structural cost and the linear quadratic control cost is optimized. This approach produces Pareto optima, namely a set of optimal structures and control inputs, and thus we need to arbitrarily select a desired solution from the set.

For robotic systems, [56] tackles design optimization of modular robotic devices for a given reference trajectory and a set of available parts. [57] optimizes the inertia of a quadrotor together with the linearized attitude controller. [12] optimizes the UAV structure for a predefined reference trajectory but does not optimize the parameters of the control law, as it only evaluates the input cost for the nominal trajectory tracking.

1.3 Contributions

The main contribution of this work is to give both analytical and numerical solutions to the joint optimization problem of the structure and control for fully actuated hexarotor UAVs. The control task is specified with an objective function and a set of initial states. Compared to other design optimization methods for the UAV structures, our approach does not need the trajectory to track. In other words, our method simultaneously designs the optimal control inputs, the corresponding optimal trajectories, and the optimal plant parameters for specified control tasks. Out method also considers the nonlinear dynamics and a nonlinear objective function for the task specifications. The optimization problem tackled in this dissertation does not fit with any of the aforementioned related reserch because of the nonlinear dynamics and the unknown optimal trajectory.

Other contributions are listed below:

- We analyze the acceleration characteristics for fully actuated hexarotor UAVs. We show that any nonplanar hexarotor is equivalently represented by planar structures. Some important properties of the dynamic manipulability is also presented.
- We propose an analytical solution to a special case of a nonlinear optimal control problem on $SE(3)$. The optimal control law is novel because the analytical solution is not trivial, and such methods for the systems on $SE(3)$ are not reported by others.
- We present a fast NMPC method for rigid body dynamics using a geometric integrator. We show that the present exact discretization method based on the Cayley map for $SE(3)$ allows us to reduce the number of decision variables of optimization while maintaining the prediction horizon duration.
- We also show that the fast optimal control method achieves real-time computation on a low-cost embedded computer by on-board simulations and an experiment.

1.4 Outline of Dissertation

In Chapter 2, we formulate the concept of joint optimization of the structure and control along with mathematical preliminaries of rigid body dynamics and optimal control. We first introduce the mathematical representation of a rigid body pose (position and orientation). In particular, a Lie group $SE(3)$ and its parametrization on a Lie algebra $\mathfrak{se}(3)$ will be used to represent the pose and its dynamics. The Hamilton-Jacobi-Bellman equation and model predictive control scheme are described as the basics of nonlinear optimal control to prepare for the definition of the main problem. Finally, as the goal of this work, we define the joint optimization problem of the structure and control with a few simple examples to illustrate the idea.

As a motivating application of the joint optimization scheme, we describe a fully actuated hexarotor system in Chapter 3. A fully actuated hexarotor is an unmanned aerial vehicle that is capable of linear and angular acceleration in any direction and axis, and it is modeled as a fully actuated rigid body system. Through an analysis of dynamic manipulability of the hexarotor, we show that the directional properties of acceleration varies depending on the rotors' positions and tilt angles. Several characteristics of the dynamical model are also derived to reduce the complexity of the design optimization problem. At the end of the chapter, an experimental vehicle and its testbed are introduced.

In Chapter 4, we study an analytical method of joint optimization for a fully actuated hexarotor under zero gravity. An optimal control problem of a rigid body dynamics on $SE(3)$ is defined and solved analytically for special cases. We also show that the resulting optimal control law resembles the double-geodesic PD controller presented in the literature. We then consider plant parameter optimization that minimizes the corresponding value function of the optimal control law. The result shows that the optimal design in this case is to maximize the dynamic manipulability of the hexarotor, and finally the effectiveness of the joint optimization scheme is verified with simulations.

The method in Chapter 5 extends the method in Chapter 4 to more general applications. In particular, we tackle a joint optimization problem of a fully actuated hexarotor under gravity. Towards the goal, we first develop a numerical optimal control method for the rigid body dynamics using the Cayley map on $SE(3)$. The numerical optimization can be efficiently computed, and we show that the NMPC law based on this method runs on an embedded controller in real time. The method is then diverted to numerically obtain the optimal parameters of the fully actuated hexarotor. The numerical method can additionally take the cost for gravity compensation into account, and the parameter optimization results in more practically reasonable structures than that obtained in Chapter 4. The effectiveness of the proposed method is verified through both simulations and an experiment.

Finally, Chapter 6 concludes this dissertation.

Nomenclature

Physical Constant

$\mathcal{I}_c \in \mathbb{R}^{3\times3}$	Inertia tensor
$\rho \in \mathbb{R}_{\geq0}$	Mass density of the air
$G \in \mathbb{R}_{\geq0}$	Gravitational acceleration constant
$m \in \mathbb{R}_{\geq0}$	Mass

Coordinate Frame

Σ_{r_i}	ith rotor's frame
Σ_c	Vehicle body frame on the center of mass
Σ_o	Inertial frame

Mathematial Notation

$(\cdot)^\top$	Transpose
(a, b)	Open interval $\{x \mid a < x < b\}$ or ordered pair
$[a, b]$	Closed interval $\{x \mid a \leq x \leq b\}$ or Lie bracket
$\|x\|_A^2$	$= x^\top Ax$
I_n	$n \times n$ identity matrix
$O_n,\ O_{n\times m}$	$n \times n$ and $n \times m$ zero matrix
$SE(3) = SO(3) \ltimes \mathbb{R}^3$	Set of 3-dimensional homogeneous transformation matrices
$SO(3)$	Set of 3-dimensional rotation matrices
$g_{ab} \in SE(3)$	Homogeneous transformation matrix (or pose in short) of frame Σ_a relative to frame Σ_b

$p_{ab} \in \mathbb{R}^3$	Position of frame Σ_a relative to frame Σ_b
$R_{ab} \in SO(3)$	Rotation matrix of frame Σ_a relative to frame Σ_b
$v_a^b \in \mathbb{R}^6$	Body velocity of frame Σ_a
$\omega_a^b \in \mathbb{R}^6$	Body angular velocity of frame Σ_a
$V_a^b = \left[v_a^{b\top}\ \omega_a^{b\top}\right]^\top \in \mathbb{R}^6$	Body twist of frame Σ_a
$v_a^s \in \mathbb{R}^6$	Spatial velocity of frame Σ_a
$\omega_a^s \in \mathbb{R}^6$	Spatial angular velocity of frame Σ_a
$V_a^s = \left[v_a^{s\top}\ \omega_a^{s\top}\right]^\top \in \mathbb{R}^6$	Spatial twist of frame Σ_a
$F_a \in \mathbb{R}^6$	Wrench acting on frame Σ_a
$R_x(\theta), R_y(\theta), R_z(\theta) \in SO(3)$	Rotation matrices respectively representing rotation by the angle θ in x, y, and z axes
$\mathrm{S}_\theta,\ \mathrm{C}_\theta$	Shorthand notations of $\sin\theta,\ \cos\theta$

Fully Actuated Hexarotor

$\beta_i \in (-\frac{\pi}{2}, \frac{\pi}{2})$	Inward/outward tilt angle of the ith rotor
$\gamma_i \in (-\frac{\pi}{2}, \frac{\pi}{2})$	Sideward tilt angle of the ith rotor
$\kappa \in \mathbb{R}_{>0}$	Counter torque constant of the propeller
$\sigma \in \mathbb{R}_{>0}$	Decomposed element of the dynamic manipulability
$\tau_i \in \mathbb{R}$	Counter torque of the ith rotor
$\varsigma_i \in \mathbb{R}_{>0}$	Rotation direction of the ith rotor
$f_i \in \mathbb{R}$	Thrust force of the ith rotor
$r \in \mathbb{R}_{>0}$	Distance between a rotor and the center of mass
$w_{dr} \in \mathbb{R}_{>0}$	Rotational dynamic manipulability measure of the hexarotor
$w_{dt} \in \mathbb{R}_{>0}$	Translational dynamic manipulability measure of the hexarotor
$w_d \in \mathbb{R}_{>0}$	Dynamic manipulability measure of the hexarotor

Other Symbols

J	Objective function
N	Number of prediction steps
T	Sampling period / Control period
U	Value function

Chapter 2

Preliminaries

This chapter defines mathematical symbols and introduces notions of rigid body motion and nonlinear optimal control. Based on the fundamentals, we set up a concept of design optimization that simultaneously determines both physical parameters of the controlled object and the control law. We call this type of problem *joint optimization of the structure and control*.

The rest of this chapter is organized as follows. In Section 2.1, we provide mathematical foundations of rigid body motion. The nonlinear optimal control problem is then defined, and two solution methods are explained in Section 2.2. In Section 2.3, we define the goal of this work, joint optimization of the structure and control, with a few simple examples that motivates the need of this work. Section 2.4 summarizes this chapter.

2.1 Mathematical Representation of Rigid Body Motion

In this section, we introduce mathematical foundations of rigid body motion. The states of a rigid body can be expressed with an element of the special Euclidean group and its corresponding algebra. We give the notion of these mathematical tools and formulas regarding them in this section.

In this dissertation, O_n and $O_{n\times m}$, respectively, denote the $n \times n$ and $n \times m$ zero matrices, and I_n denotes the $n \times n$ identity matrix. All the coordinate frames are Cartesian and right handed. We suppose that the body is not deformable.

2.1.1 Dynamical Systems on $SE(3)$

Rigid Body Pose and $SE(3)$

The *pose*, namely the position and orientation, of a rigid body in the 3-dimensional Euclidean space is expressed as an ordered pair of a 3-dimensional position vector and a 3-dimensional

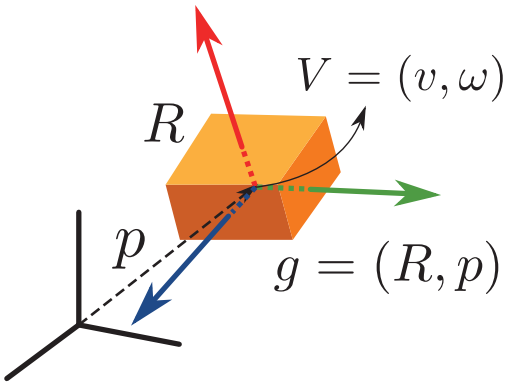

Fig. 2.1: Rigid body pose

rotation matrix, as illustrated in Fig. 2.1. The set of all 3-dimensional rotation matrices forms *special orthogonal group* $SO(3)$, and it is defined as follows:

$$SO(3) := \left\{ R \in \mathbb{R}^{3\times 3} \mid R^\top R = R R^\top = I_3,\ \det R = 1 \right\}.$$

Let $p \in \mathbb{R}^3$ and $R \in SO(3)$ be the 3-dimensional position and orientation of a rigid body, respectively. Then the pose of a rigid body is written in a matrix form

$$g = \begin{bmatrix} R & p \\ O_{1\times 3} & 1 \end{bmatrix} \in \mathbb{R}^{4\times 4}.$$

This matrix is referred to as the *homogeneous transformation matrix*, and it represents both the pose and coordinate transformation in 3-dimensional Euclidean space. The set of all the homogeneous transformation matrices is called *special Euclidean group* $SE(3)$. The following definition of $SE(3)$ is more formal and considered with the Lie group structure of $SE(3)$:

$$SE(3) := SO(3) \ltimes \mathbb{R}^3,$$

where $\ltimes$ denotes semidirect product of groups. In this dissertation, we use a notation $g \in SE(3)$ to express both the ordered pair (R, p) and the homogeneous transformation matrix depending on the context.

The Lie algebras $\mathfrak{so}(3)$ and $\mathfrak{se}(3)$ related to the groups $SO(3)$ and $SE(3)$, respectively, consist of matrices

$$\widehat{\omega} = (\omega)^\wedge = \begin{bmatrix} 0 & -\omega_3 & \omega_2 \\ \omega_3 & 0 & -\omega_1 \\ -\omega_2 & \omega_1 & 0 \end{bmatrix} \in \mathfrak{so}(3)$$

and

$$\widehat{V} = (V)^\wedge = \begin{bmatrix} \widehat{\omega} & v \\ O_{1\times 3} & 0 \end{bmatrix} \in \mathfrak{se}(3),$$

where $v \in \mathbb{R}^3$, $\omega = [\omega_1\ \omega_2\ \omega_3]^\top \in \mathbb{R}^3$, and $V = \begin{bmatrix} v^\top & \omega^\top \end{bmatrix}^\top \in \mathbb{R}^6$. v and ω can be seen as the rate of change in linear and rotational components of g, which are the linear and angular velocities of the rigid body, respectively. Here, the "wedge" operator $(\cdot)^\wedge$ is used to identify the elements of the Lie algebras with real vectors. We also define the "vee" operator $(\cdot)^\vee$ as the inverse of the wedge operator. An element of $\mathfrak{so}(3)$ is *skew-symmetric* because it satisfies $\widehat{\omega}^\top = -\widehat{\omega}$.

First Order System on $SE(3)$

$$\dot{g} = g\widehat{V}^b \tag{2.1}$$

where $V^b = [v^{b\top}\omega^{b\top}]^\top = (g^{-1}\dot{g})^\vee \in \mathbb{R}^6$ is the *twist* (linear and angular velocity) in the body frame. This system is said to be *left invariant* as the equation is invariant under left translation, i.e.,

$$\frac{d}{dt}hg = (hg)\widehat{V}^b,$$

where $h \in \mathbb{R}^4$ is a constant matrix. It is also possible to obtain a corresponding right invariant system as follows:

$$\dot{g} = \widehat{V}^s g.$$

Here, V^s denotes the twist in the spatial frame. In this dissertation, we use the body twist V^b rather than the spatial twist if the frame notation is not present, unless otherwise noted.

Second Order System on $SE(3)$

A second order dynamical system on $SE(3)$ has a form

$$\begin{aligned} \dot{g} &= g\widehat{V}^b \\ \dot{V}^b &= u_{\text{total}}, \end{aligned} \tag{2.2}$$

where u_{total} denotes the total linear and angular acceleration including the control input and acceleration due to the force applied to the body.

Newton-Euler Equation of Rigid Body Dynamics

Consider a rigid body with the mass $m \in \mathbb{R}$ and the inertia tensor $\mathcal{I} \in \mathbb{R}^{3\times3}$. Let $g \in SE(3)$ and $V^b \in \mathbb{R}^6$ be the pose and the body twist of the rigid body, respectively. Assume that the *wrench* (force and torque) $F \in \mathbb{R}^6$ and the force of gravity expressed in the body frame

$$F_{\text{grav}} = \begin{bmatrix} R^\top \begin{bmatrix} 0 & 0 & -mG \end{bmatrix}^\top \\ O_{3\times1} \end{bmatrix} \tag{2.3}$$

are acting on the center of mass. Here, $G \in \mathbb{R}$ denotes the gravitational acceleration constant. Then, the rigid body dynamics evolve according to the first order left invariant system on $SE(3)$ and the Newton-Euler equation of motion [58].

$$\begin{aligned} \dot{g} &= g\widehat{V}^b \\ \begin{bmatrix} mI_3 & O_3 \\ O_3 & \mathcal{I} \end{bmatrix} \dot{V}^b + \begin{bmatrix} m\widehat{\omega}^b v^b \\ \widehat{\omega}^b(\mathcal{I}\omega^b) \end{bmatrix} &= F - F_{\text{grav}} \end{aligned} \tag{2.4}$$

We transform the equations of motion by canceling the second term of (2.4), namely the Coriolis force and gyroscopic torque, via feedback linearization. The dynamics are finally expressed as the following second order system on $SE(3)$ in the form of equation (2.2):

$$\begin{aligned} \dot{g} &= g\widehat{V}^b \\ \dot{V}^b &= u_c - u_{\text{grav}}, \end{aligned} \tag{2.5}$$

where

$$u_c = \begin{bmatrix} mI_3 & O_3 \\ O_3 & \mathcal{I} \end{bmatrix}^{-1} F - \begin{bmatrix} \widehat{\omega}^b v^b \\ \mathcal{I}^{-1}\widehat{\omega}^b(\mathcal{I}\omega^b) \end{bmatrix}$$

is the acceleration control input of the body applied to the center of mass, and $u_{\text{grav}} = \frac{1}{m}F_{\text{grav}}$.

2.1.2 Coordinate Frames and Transformations

Properties of Homogeneous Transformation Matrices

Consider coordinate frames Σ_a, Σ_b, and Σ_c, and assume that the poses of the coordinate frames Σ_b and Σ_c relative to the frame Σ_a are written as g_{ab} and g_{ac}, respectively. Likewise, the pose of Σ_a and Σ_c looked from Σ_b frame are, respectively, written as g_{ba} and g_{bc}. Then, the homogeneous matrices have the following properties:

- The inverse of the homogeneous transformation matrix represents transformation in the opposite direction: $g_{ba} = g_{ab}^{-1}$.

- The pose of Σ_b relative to frame Σ_c is given by the product of transformations: $g_{bc} = g_{ba}g_{ac}$.

Transformation of Twist and Wrench

We now show the relation between multiple twist or wrench that are observed and expressed in different coordinate frames. First of all, we introduce the adjoint representation of the group element $g \in SE(3)$ as follows:

$$\mathrm{Ad}_g = \begin{bmatrix} R & \widehat{p}R \\ O_3 & R \end{bmatrix}.$$

Then, V_{ac}^b, which is the body twist of Σ_c relative to frame Σ_a, is given as

$$V_{ac}^b = \mathrm{Ad}_{g_{bc}^{-1}} V_{ab}^b + V_{bc}^b.$$

If the frames Σ_b and Σ_c are attached on the same rigid body, then $V_{ac}^b = \mathrm{Ad}_{g_{bc}^{-1}} V_{ab}^b$.

Now, suppose that Σ_b and Σ_c are attached on the same rigid body, and wrench F_c is acting on Σ_c. From an equation of the instantaneous work $V_{ac}^{b\top} F_c = V_{ab}^{b\top} F_b$, we obtain

$$(\mathrm{Ad}_{g_{bc}^{-1}} V_{ab}^b)^\top F_c = V_{ab}^{b\top} F_b.$$

Since $\mathrm{Ad}_{g_{bc}^{-1}} = \mathrm{Ad}_{g_{cb}}$, the relation between wrench F_b and F_c is formulated as

$$F_b = \mathrm{Ad}_{g_{cb}}^\top F_c. \tag{2.6}$$

Note that when we calculate the sum of wrench applied to different locations on a rigid body, we must transform all of it to an arbitrary coordinate frame before taking the sum. We will use this formula (2.6) in Section 3.1 to calculate the total wrench that is generated by the actuators.

2.1.3 Several Parametrization of $SE(3)$

Elements of $SE(3)$ can be expressed in different forms other than the homogeneous transformation matrices. Some methods of the parametrization of $SE(3)$ exist, and we describe some of them that are used in this dissertation. The motivation of parametrization is to reduce the number of parameters from 4×4. The minimum possible number is 6, which is the intrinsic degrees of freedom of rigid body translation and rotation. In other words, a homogeneous transformation matrix has 10 independent constraints among 16 elements of the matrix. However, due to a topological property of $SO(3)$, the pose cannot be expressed with only 6 parameters without suffering from singularity. We also illustrate this property

for each parametrization method.

Position Vector and Euler Angles

Euler angles or Roll-Pitch-Yaw angles, a variant of Euler angles, are the most common parametrization of 3-dimensional rotation. The original Euler angles are defined as follows by the sequence of rotation in axes with the order Z-X-Z:

$$R = R_z(\alpha)R_x(\beta)R_z(\gamma),$$

where α, β, and γ are the angles. Likewise, the Roll-Pitch-Yaw angles (also known as Tait-Bryan angles) are usually defined as follows:

$$R = R_z(\alpha)R_y(\beta)R_x(\gamma).$$

$R_x(\theta), R_y(\theta)$, and $R_z(\theta) \in SO(3)$ are rotation matrices representing rotation by the angle θ in x, y, and z axes, respectively.

This parametrization is useful when the object rotates around zero angles, and thus many applications such as airplanes or underactuated multirotors rely on this representation. However, it suffers from the so-called "gimbal lock" phenomenon, where two of the three rotation axes become parallel when the dynamical equation is described with these parameters.

Exponential Coordinates

The exponential maps $\exp : \mathfrak{se}(3) \to SE(3)$, $\mathfrak{so}(3) \to SO(3)$ are, respectively, given as follows [58]:

$$\exp(\widehat{\psi}) = \begin{bmatrix} \exp(\widehat{\eta}) & \frac{(I_3 - \exp(\widehat{\eta}))\widehat{\eta}\xi + \eta\eta^\top\xi}{\|\eta\|^2} \\ O_{1\times 3} & 1 \end{bmatrix}, \tag{2.7}$$

$$\exp(\widehat{\eta}) = I_3 + \frac{\sin(\|\eta\|)}{\|\eta\|}\widehat{\eta} + \frac{1-\cos(\|\eta\|)}{\|\eta\|^2}\widehat{\eta}^2 \tag{2.8}$$

if $\|\eta\| \neq 0$, and otherwise,

$$e^{\widehat{\psi}} = \begin{bmatrix} I_3 & \xi \\ O_{1\times 3} & 1 \end{bmatrix}, \; e^{\widehat{\eta}} = I_3.$$

The exponential map for $SE(3)$ described in (2.7) can be regarded as the extended version of Rodrigues' formula of rotation, which is identical to the equation (2.8).

The logarithm map $\log : SE(3) \to \mathfrak{se}(3)$ is the inverse of the exponential map [58, 59], and it is used to obtain the twist $\widehat{\psi} \in \mathfrak{se}(3)$ that is required to move the pose from the identity, i.e., $g = \exp(\widehat{\psi})$. For $SO(3)$, the logarithm of a rotation matrix R can be calculated

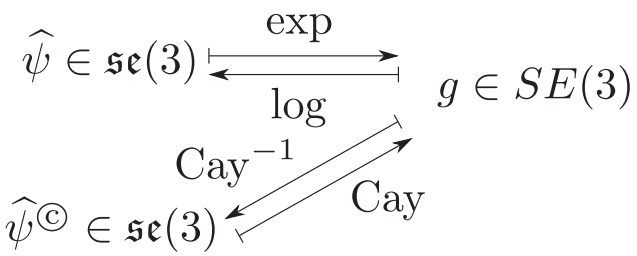

Fig. 2.2: Relation among $\psi, \psi^{\copyright}$, and g.

as follows:

$$a = \frac{1}{2}\left(R - R^{\top}\right)^{\vee}$$
$$\log(R) = \begin{cases} \frac{\sin^{-1}(\|a\|)}{\|a\|}\widehat{a} & \text{for } \|a\| \neq 0 \\ O_3 & \text{for } \|a\| = 0 \end{cases}.$$

By applying the "vee" operator, we can obtain the 3-dimensional vector form of the rotation matrix R. This parametrization of $SO(3)$ is known as the axis-angle representation or the rotation vector. As the name suggests, $\log(R)^{\vee}$ corresponds to the axis vector of rotation multiplied by the angle.

For $SE(3)$, we have

$$\log(g) = \begin{bmatrix} \log(R) & \left(I_3 - \frac{1}{2}\log(R) + (1 - \alpha(\|\log(R)^{\vee}\|))\frac{(\log(R))^2}{\|\log(R)^{\vee}\|^2}\right)p \\ O_{1\times 3} & 0 \end{bmatrix} \in \mathfrak{se}(3),$$

where $\alpha(y) = (y/2)\cot(y/2)$, for $\log(R) \neq O_3$, and we also have

$$\log(g) = \begin{bmatrix} O_3 & p \\ O_{1\times 3} & 0 \end{bmatrix}$$

for $\log(R) = O_3$. By applying the "vee" operator, we obtain the twist vector

$$\psi = \log(g)^{\vee} \in \mathbb{R}^6. \tag{2.9}$$

The vector ψ can be considered as a 6-dimensional parametrization of the pose g.

Remark 2.1. This parametrization becomes singular when the attitude is at $\mathrm{tr}R = -1$. The singular attitudes corresponds to the rotation by $\pm\pi$ rad in any axis. Only for poses with such orientation, there exist two possible values representing the same pose.

Cayley Map

Several definitions of the Cayley map exist in the literature. In this dissertation, we refer to [39] for the definition. Let $\widehat{\psi}^{\copyright} \in \mathfrak{se}(3)$ and $g \in SE(3)$. The Cayley map for $SE(3)$ is a

mapping from the Lie algebra $\mathfrak{se}(3)$ to the group $SE(3)$ defined as follows:

$$\begin{aligned} \mathrm{Cay}(\widehat{\psi}^{\copyright}) &= (I_4 - \widehat{\psi}^{\copyright})^{-1}(I_4 + \widehat{\psi}^{\copyright}) = g, \\ \mathrm{Cay}^{-1}(g) &= (g + I_4)^{-1}(g - I_4) = \widehat{\psi}^{\copyright}. \end{aligned} \tag{2.10}$$

We call $\psi^{\copyright} \in \mathbb{R}^6$ the *Cayley parameter* of g in this dissertation. The Cayley parameter is another 6-dimensional parametrization of the pose of a rigid body. The symbol $(\cdot)^{\copyright}$ denotes a vector regarding the Cayley map and its derivatives. Fig. 2.2 shows the relation among these symbols that we use throughout this dissertation.

In contrast to the exponential map, the Cayley map does not represent the mapping from the physically meaningful twist to the pose. It is thus important to obtain transformations between the actual twist ψ and the Cayley parameter $\psi^{\copyright}$. Here, we define the Cayley parameter corresponding to $\psi = \log(g) = \left[\xi^\top \ \eta^\top\right]^\top$ as $\psi^{\copyright} = \left[\xi^{\copyright\top} \ \eta^{\copyright\top}\right]^\top$. We separately consider the translational and rotational parts denoted by ξ and η, respectively. Direct calculation of $\psi^{\copyright} = \mathrm{Cay}^{-1}(\exp(\widehat{\psi}))^\vee$ yields

$$\xi^{\copyright} = \underbrace{\left(\frac{\eta\eta^\top}{2\|\eta\|^2} - \frac{\tan\frac{\|\eta\|}{2}}{\|\eta\|} \frac{\widehat{\eta}^2}{\|\eta\|^2} \right)}_{:=\mathcal{A}(\eta)\in\mathbb{R}^{3\times 3}} \xi, \tag{2.11}$$

$$\eta^{\copyright} = \frac{\tan\frac{\|\eta\|}{2}}{\|\eta\|}\eta. \tag{2.12}$$

if $\eta \neq O_{3\times 1}$. Likewise, $\eta^{\copyright} = O_{3\times 1}$ and $\xi^{\copyright} = \frac{1}{2}\xi$ hold if $\eta = O_{3\times 1}$. Note that $\lim_{\|\eta\|\to 0} \psi^{\copyright} = \psi^{\copyright}|_{\eta = O_{3\times 1}}$ holds, and thus (2.11) and (2.12) are continuous at $\eta = O_{3\times 1}$.

Fig. 2.3 shows the relation between the axis-angle representation $\eta = \log(R)^\vee$ and the Cayley parameter $\eta^{\copyright}$ in (2.12). The axis-angle representation for the rotation matrix R except for $\mathrm{tr}(R) = -1$ is in $B_\pi := \{\eta \in \mathbb{R}^3 \mid \|\eta\| < \pi\}$, namely, an open ball of radius π, and the conversion to the Cayley parameter corresponds to stretching of the ball to the whole space $\mathbb{R}^3$. $\eta^{\copyright}$ corresponds to the classical Rodrigues parameter, which is one of the representations of 3-dimensional rotation [60]. In fact, we have the same relation between the Rodrigues parameter $\eta^{\copyright}$ and the corresponding rotation matrix R, as in (2.10).

$$R = (I_3 - \widehat{\eta}^{\copyright})^{-1}(I_3 + \widehat{\eta}^{\copyright})$$

Therefore, we can interpret $\psi^{\copyright}$, the Cayley parameter for $SE(3)$, as an extended version of the Rodrigues parameter.

Remark 2.2. The Cayley parametrization also has singular orientations when the atittude satisfies $\mathrm{tr}R = -1$. With such orientation, the norm of the rotational part becomes infinity, and the parameter loses the information of the rotation axis.

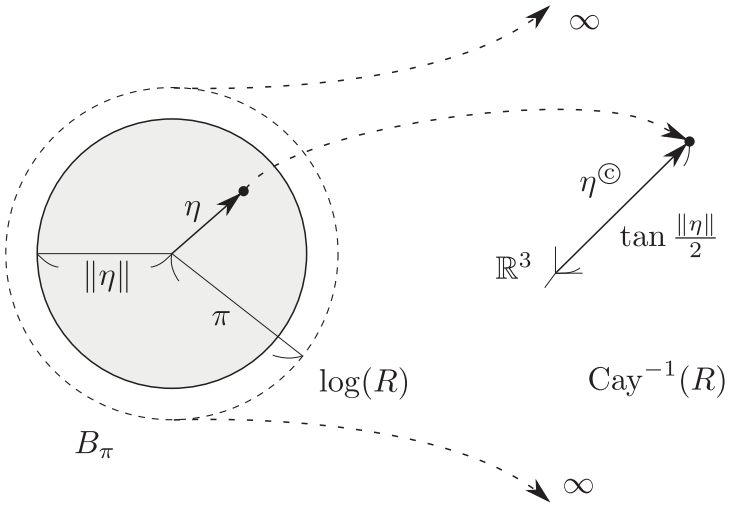

Fig. 2.3: Relation of $\log(R)$ and $\mathrm{Cay}^{-1}(R)$. The conversion from the axis-angle representation to the Cayley parameter corresponds to stretching of an open ball to $\mathbb{R}^3$.

2.2 Nonlinear Optimal Control

In this section, we briefly describe analytical and numerical methods for solving nonlinear optimal control problems. An optimal control problem seeks the control input and the corresponding trajectory that minimize a function, which is called *objective function* or cost function, subject to the system dynamics. Two methods are described to provide the foundation of our later discussions.

2.2.1 Hamilton-Jacobi-Bellman Equation

Consider the following optimal control problem:

$$\min_{u(x,t)} \int_0^{t_f} L(x(t), u(t))dt + L_f(x(t_f)) \quad \text{subject to} \quad \dot{x}(t) = f(x(t), u(t)), \tag{2.13}$$

where $t_f > 0$ is the terminal time, $x(t) \in \mathbb{R}^n$ is the state variable, $u(t) \in \mathbb{R}^m$ is the input vector, $L : \mathbb{R}^n \times \mathbb{R}^m \to \mathbb{R}$ is an incremental cost function, and $L_f(x(t_f)) \in \mathbb{R}$ is the terminal cost. Note that the dynamical model of the controlled system is expressed as equality constraints in the optimization problem. The Hamilton-Jacobi-Bellman (HJB) partial differential equation [61] is

$$\frac{\partial U(x,t)}{\partial t} + \min_{u(x,t)} \{\nabla U(x,t) \cdot f(x,u) + L(x,u))\} = 0$$

where the scalar function $U(x,t)$ is called *value function*, which represents the minimum value of the cost when the optimal control input u^* is applied. The boundary conditions of

the value function are

$$U(x(0),0) = \min_{u(x,t)} \int_0^{t_f} L(x(t),u(t))dt + L_f(x(t_f))$$

and $U(x(t_f),t_f) = U_f(x(t_f))$. The part that is minimized in the above equation is called *Hamiltonian*, and the minimizer of the Hamiltonian becomes the optimal control input. In this dissertation, we assume that the value function is time-invariant, and the terminal condition is $t_f = \infty$ and $U_f(t_f) = 0$. For this special case, we obtain the following HJB equation.

$$\min_{u(x)} \left\{ \dot{U}(x) + L(x,u) \right\} = 0 \tag{2.14}$$

According to the Bellman's dynamic programming principle, the optimal control problem (2.13) becomes equivalent to solving the HJB equation (2.14) with respect to the unknown value function U. It is proved that the HJB equation is the necessary and sufficient condition of the optimality of the control input.

The shortcoming of this approach is that it requires the exact solution of the HJB differential equation. Although we can expect that the value function takes the similar form to the objective function, it is difficult to obtain in general.

2.2.2 Model Predictive Control

Instead of solving the HJB equation, we can use numerical optimization algorithms to acquire the optimal control input that minimize the objective function. Now, we consider a finite-horizon discrete-time nonlinear optimal control problem

$$\min_{\boldsymbol{u},\boldsymbol{x}} \sum_{k=1}^{N} L(x_k,u_k) + U_f(x_N) \quad \text{subject to} \quad x_{k+1} = f(x_k,u_k), \tag{2.15}$$

where $\boldsymbol{u} = (u_0,\ u_1,\ \ldots,\ u_{N-1})$ and $\boldsymbol{x} = (x_1,\ x_2,\ \ldots,\ x_N)$ denote the sequence of the control input and the state trajectory, respectively, and N denotes the number of time steps to be concerned. By solving this problem numerically, we can obtain the optimal control input sequence $\boldsymbol{u}^*$ and the corresponding trajectory $\boldsymbol{x}^*$. If the dynamical model precisely describes the system dynamics, the optimal trajectory is achieved by applying the input sequence at each time step.

However, this optimal control approach is a feedforward method, and it is vulnerable to disturbances applied to the controlled system. The *model predictive control* (MPC) scheme repetitively solves the numerical optimal control problem (2.15) to overcome this issue. Fig. 2.4 illustrates the scheme. Here, T denotes the sampling period of the prediction. The time frame of duration NT considered in the optimal control problem is called *prediction*

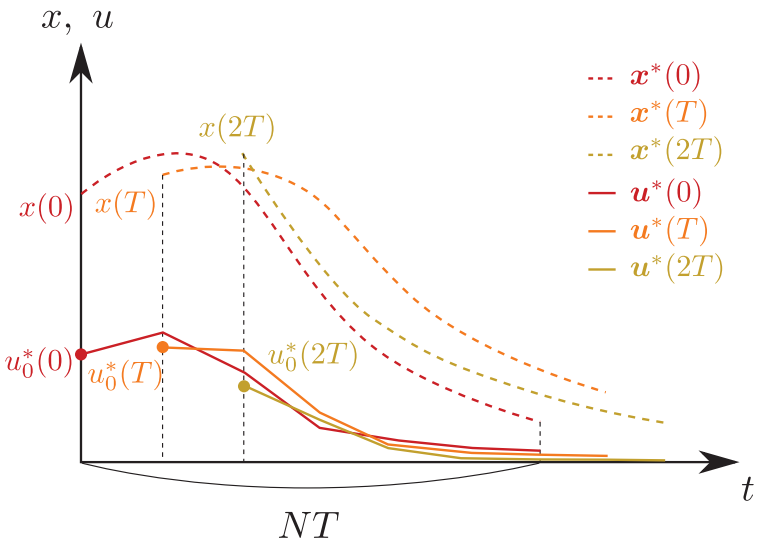

Fig. 2.4: Model predictive control scheme. The optimal control input sequence $\boldsymbol{u}^*(t)$ and the corresponding solution trajectory $\boldsymbol{x}^*(t)$ at time t is calculated by solving a finite horizon optimal control problem with the initial state $x(t)$. The first value of the optimal input sequence is applied to the system. This process is executed in every time step.

horizon. We can choose arbitrary control period in general. In this dissertation, however, we set the control period to T for simplicity. In each control period at time t, we solve the optimization problem numerically for the observed initial state $x(t)$ and obtain the optimal input sequence $\boldsymbol{u}^*(t)$ and the corresponding solution trajectory $\boldsymbol{x}^*(t)$. Then, the initial value of the input sequence, namely, $u_0^*(t)$, is applied to the system until the next control period. This approach is also referred to as the *receding horizon* scheme.

The main drawback of this approach is that the optimization problem must be solved in each control period, while it is difficult to guarantee. This is the reason that the use of MPC schemes on embedded systems for real-time applications is limited. In Chapter5, we will develop a fast nonlinear MPC (NMPC) method specialized in the rigid body dynamics in the 3-dimensional space. The presented approach uses the so-called recursive discretization technique among many approaches to remedy the issue. The recursive discretization [1] technique [38, Chapter 10] is a method to minimize the number of decision variables of the optimal control problem (2.15). The method uses a fact that the state trajectory in the objective function and constraints can be expressed as a function of the initial state and the sequence of control inputs. This idea is closely related to the direct shooting method, which the objective function is evaluated by actually simulating the trajectory for a given sequence of inputs.

Moreover, in this dissertation, a geometric integrator based on the Cayley map for $SE(3)$ is introduced to compute the exact change in the pose. The method allows us to pick coarse sampling periods while maintaining the accurate trajectory prediction and to further reduce

[1] Here, "discretization" does not mean the discretization that converts a continuous-time system to a discrete-time system, and the name is according to the convention.

the number of decision variables. At present, general purpose NLP solver has a polynomial time complexity, and thus it is important to work on a small number of variables to achieve fast computation.

2.3 Problem Settings of Joint Optimization of Structure and Control

The purpose of this section is to define a design optimization problem of both the physical parameters and the control input for dynamical systems.

Control performance such as input energy and settling time can be affected by both the control law and the plant parameters of the controlled object. Although it is natural to consider plant optimization for the improvement of the control performance, it is not investigated well while the optimal control is eagerly developed in theory and applications. In the view of this motivation, we propose an optimal plant design method based on optimal control, that is, minimization of the value function corresponding to the optimal control problem. This approach gives optimally determined plant parameters with associated optimal control law simultaneously. We call this approach *joint optimization* because the two different optimization problems, design optimization and optimal control, are connected via the same objective function.

Now, we illustrate the idea of joint optimization with a simple example of a first-order integrator system.

Example 2.1. Let $x \in \mathbb{R}$ and $u \in \mathbb{R}$ be the state variable and the control input, respectively. Consider the first-order integrator system $\dot{x} = \theta u$, where $\theta > 0$ is a plant parameter representing the input gain. The objective function to minimize along the trajectory of the dynamics is defined as

$$J = \frac{1}{2}\int_0^\infty \left(qx^2 + ru^2\right) dt,$$

where $q > 0, r > 0$ are the weight constants. Then, the HJB equation for this optimal control problem is formulated as

$$\min_u \left\{ \frac{1}{2}qx^2 + \frac{1}{2}ru^2 + \frac{\partial U}{\partial x}\theta u \right\} = 0,$$

and the value function U and the optimal control input u^* are readily calculated as

$$U(x \mid \theta) = \frac{\sqrt{qr}}{2\theta}x^2$$
$$u^* = -\frac{\theta}{r}\frac{\partial U}{\partial x}.$$

To obtain the optimal plant parameters, we can minimize either the maximum or average value of U over the initial state set X_0 with respect to the plant parameter. In this simple example, maximizing θ yields minimization of U regardless of the initial state.

The result of Example 2.1 might seem trivial because the state will converge faster when the gain parameter θ is larger. However, this result does not simply apply to every case. In the next example, we illustrate the dependence of optimal parameters on initial states by considering a little more complex case where the plant parameters are mutually constrained.

Example 2.2. Let $x, u \in \mathbb{R}^2$. Consider a 2-dimensional linear system

$$\dot{x} = \begin{bmatrix} \theta_1 & 0 \\ 0 & \theta_2 \end{bmatrix} u,$$

where $\theta_1 \in \mathbb{R}$ and $\theta_2 \in \mathbb{R}$ are the plant parameters, and assume that they are constrained by $\theta_1 + \theta_2 = 1$. Now we consider the following cost function to minimize:

$$J = \frac{1}{2} \int_0^\infty \left(x^\top Q x + u^\top R u \right) dt,$$

where $Q = \mathrm{diag}(q_{11}, q_{22}) \in \mathbb{R}^{2\times 2}$ and $R = \mathrm{diag}(r_{11}, r_{22}) \in \mathbb{R}^{2\times 2}$ are positive definite weight matrices. As the solution of this optimal control problem, the value function and the corresponding optimal control input are calculated as follows:

$$U(x \mid \theta) = x^\top \begin{bmatrix} \frac{\sqrt{q_{11} r_{11}}}{2\theta_1} & 0 \\ 0 & \frac{\sqrt{q_{22} r_{22}}}{2\theta_2} \end{bmatrix} x,$$
$$u^* = -R^{-1} \begin{bmatrix} \frac{\sqrt{q_{11} r_{11}}}{2\theta_1} & 0 \\ 0 & \frac{\sqrt{q_{22} r_{22}}}{2\theta_2} \end{bmatrix} x.$$

Note here that the minimum value of U with respect to $\theta = [\theta_1 \ \theta_2]^\top$ depends on the initial state because of the plant parameter constraint. For example, if the weight matrices are $Q = I_2, R = I_2$, and the initial state is $x_0 = [a \ b]^\top$, the minimum cost for the optimal control is $U = \frac{a^2}{2\theta_1} + \frac{b^2}{2\theta_2}$. Tedious calculation leads to the optimal plant parameters

$$\theta_1 = \frac{a}{a \pm b}, \ \theta_2 = \frac{\pm b}{a \pm b}.$$

As seen by this simple example, the optimal parameters vary according to the initial states even if the objective function is not changed.

From this observation, we suggest that the control task should be defined not only by an objective function but also by a set of initial states. We finally define the joint optimization problem of the structure and control as follows:

Definition 2.1. Assume that the system dynamics are parameterized with d design parameters $\theta \in \mathbb{R}^d$, and suppose that the control task is described by an objective function $J(x, u \mid \theta)$, constraints $C(x, u \mid \theta) = 0,\ D(x, u \mid \theta) \leq 0$, and a set of initial states X_0. The effort of optimal control is defined as the minimum value of the objective function J (i.e., the value function $U(x_0 \mid \theta)$) with respect to the constraints and dynamics, for an initial state $x_0 \in X_0$. Then, joint optimization of the structure and control is to minimize the effort of optimal control U over the initial state set X_0 by modifying the design parameters θ.

Note that the minimization can be either performed for the mean or maximum value of the optimal control effort U.

2.4 Chapter Summary

In Section 2.1, we have introduced the mathematical foundation of rigid body dynamics. First-order and second-order systems on the special Euclidean group $SE(3)$ are discussed and it is shown that the Newton-Euler equation of rigid body motion can be transformed into a second-order system on $SE(3)$. We have also described some parametrizations of rigid body pose to formulate state vectors corresponding to the matrix element of $SE(3)$. Some useful formulas are provided at the end of the section.

In Section 2.2, we have treated the basics of nonlinear optimal control problem. We have introduced Hamilton-Jacobi-Bellman equation as the necessary and sufficient condition of optimality. The model predictive control scheme is also introduced as a numerical approach for the optimal feedback control problem. The two solution methods will be later used in the analytical and numerical optimal control methods in Chapter 4 and 5, respectively.

As the main goal of this work, we have set up the concept of joint optimization of the structure and control in Section 2.3. The idea of the joint optimization scheme is to reuse the value function of the optimal control problem as the objective function to minimize with respect to the plant parameters. Two simple examples are given to illustrate the concept.

Chapter 3

Fully Actuated Hexarotor UAV

This chapter introduces dynamical model and the properties of a fully actuated hexarotor UAV, which is the main application of this research. A hexarotor UAV is a multirotor UAV equipped with six rotors. The standard-type hexarotor shown in Fig. 1.1 can generate force only in the upper direction, and thus the vehicle is underactuated; it can only control 4 degrees of freedom out of 6. In this work, we change the position and orientation of each rotor as seen in Fig. 3.1 to make the vehicle fully actuated. The full-actuation property allows us to control the translational and rotational motion independently, resulting in general 3D motion capability and enhanced robustness against horizontal external force. In this chapter, we analyze how the full-actuation property varies according to the rotor positions and tilt angles, aiming to find the optimal structure of the fully actuated hexarotor.

The rest of this chapter is organized as follows. In Section 3.1, we derive the dynamical model of a fully actuated hexarotor UAV based on aerodynamics and rigid body dynamics. Then, the relation between the thrust force generated by each rotor and the total wrench applied to the center of mass is analyzed in Section 3.2. We prove that nonplanar structures can be transformed into planar structures without changing the relation. The fact greatly simplifies the subsequent discussion because considering only planar structures is sufficient for the analysis regarding the wrench. Moreover, related research is classified by using this simplification method, and it is then shown that there exist two standard classes of fully actuated hexarotors. In Section 3.3, we define the dynamic manipulability of the hexarotor as an index of full-actuation performance. The analysis on the dynamic manipulability shows that it is suitable for the characteristics evaluation of the structure itself. Section 3.4 describes our experimental vehicle and its testbed along with the result of a preliminary experiment. This chapter is written based on the author's previous work [23–25] [1].

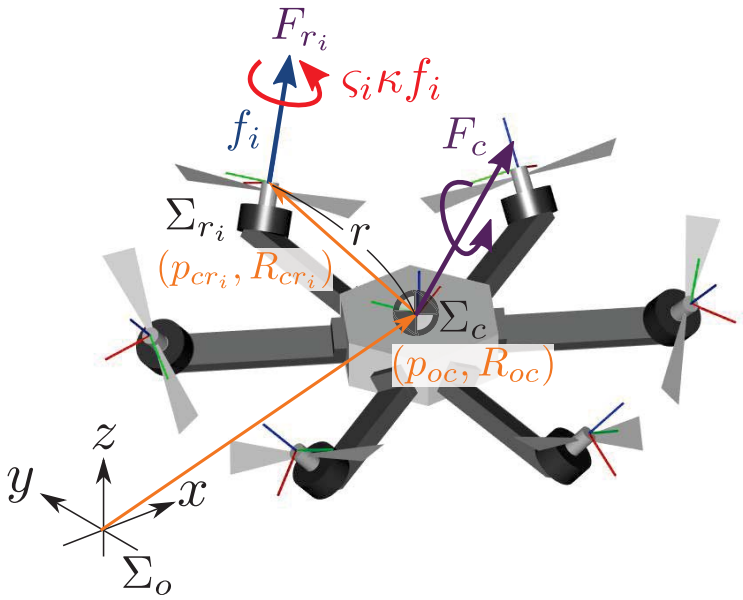

Fig. 3.1: Hexarotor model. In this work, we consider nonplanar/nonparallel structures. The six rotors can be tilted and placed arbitrarily, but they are fixed during flight.

3.1 Modeling

In this dissertation, each rotor is modeled such that it can generate desired amount of thrust force f_i in one direction. The counter torque τ_i is simultaneously generated proportionally to the thrust force, as shown in Fig. 3.2. This relation is explained by a well known approximation of the aerodynamic phenomenon around the rotor. The following model is obtained by assuming that the flow rate is constant [62]:

$$\begin{aligned} f_i &= \rho A (\Omega_i r)^2 C_f, \\ \tau_i &= \varsigma_i \rho A (\Omega_i r)^2 r C_\tau, \end{aligned}$$

where $\rho \in \mathbb{R}$ is the mass density of the air, and $\varsigma_i \in \{-1, 1\}$ is the rotation direction of the ith rotor. $r, A, \Omega_i \in \mathbb{R}$ are the radius, surface area, and the angular velocity of the propeller, respectively. $C_f \in \mathbb{R}$ and $C_\tau \in \mathbb{R}$ are coefficients determined by the shape of the propeller. Since ρ, r, A, C_f, and C_τ are constant, we obtain

$$\begin{aligned} f_i &= k_f \Omega_i^2 \\ \tau_i &= \varsigma_i k_\tau \Omega_i^2 = \varsigma_i \kappa f_i, \end{aligned}$$

where $\kappa = \frac{k_\tau}{k_f}$. Quite a few studies use this approximation model of the rotor thrust force and torque (for example, [8, 12, 14, 15, 18]). In this dissertation, we additionally assume that the

[1] ©2018 IEEE. Partly reprinted, with permission, from [25].

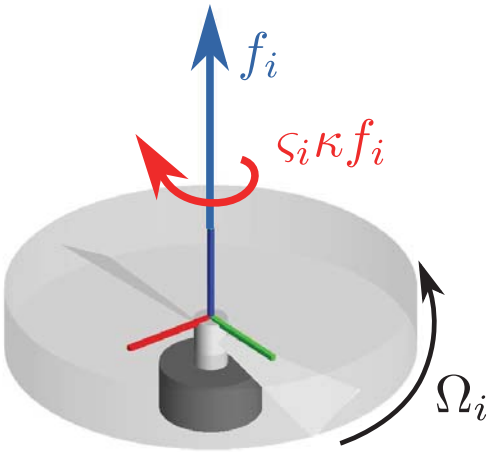

Fig. 3.2: Rotor model. The rotors can generate desired amount of thrust force in each direction. At the same time, counter torque around the same axes are also generated proportionally to the force.

rotor can generate the command force instantaneously and neglect the delay of the thrust force due to the inertia of a propeller. We suppose also that the aerodynamic interference among rotors is sufficiently smaller than the thrust force.

Figure 3.1 illustrates the hexarotor model and symbols. We suppose that the rotors can be arbitrarily placed and tilted, allowing nonplanar or nonparallel structures other than one presented in the figure. Note that the structure is fixed during flight, and thus the vehicle has 6 inputs for controlling the 6 degrees of freedom of the rotation and translation of a 3-dimensional rigid body. The vehicle is said to be fully actuated if the rotor inputs span the 6-dimensional space.

We now derive a dynamical model of a hexarotor UAV based on rigid body dynamics. We first transform the rotor wrench (force and torque) expressed in the ith rotor frame Σ_{r_i}

$$F_{r_i r_i} = \begin{bmatrix} 0 & 0 & f_i & | & 0 & 0 & \kappa_i f_i \end{bmatrix}^\top = \begin{bmatrix} f_{r_i r_i} \top \,|\, \tau_{r_i r_i}^\top \end{bmatrix}^\top$$

into the wrench F_{cr_i} expressed in the vehicle body frame at the center of mass Σ_c.

$$F_{cr_i} = \mathrm{Ad}_{g_{r_i c}}^\top F_{r_i r_i}. \tag{3.1}$$

Here, we have used the transformation formula of wrench in equation (2.6). By taking sum of F_{cr_i}, we obtain the net wrench applied to the center of mass of the vehicle as follows:

$$F_c = \sum_{i=1}^{6} F_{cr_i} = \begin{bmatrix} f_c \\ \tau_c \end{bmatrix}.$$

Then, the Newton-Euler equation of this system is derived as follows:

$$\begin{bmatrix} mI_3 & O_3 \\ O_3 & \mathcal{I} \end{bmatrix} \begin{bmatrix} \dot{v}_c^b \\ \dot{\omega}_c^b \end{bmatrix} + \begin{bmatrix} m\widehat{\omega}_c^b v_c^b \\ \widehat{\omega}_c^b(\mathcal{I}\omega_c^b) \end{bmatrix} = F_c + F_{\text{grav}}, \tag{3.2}$$

where F_{grav} is defined in (2.3) with $R = R_{oc}$. v_c^b and ω_c^b are the body translational and angular velocity of the vehicle, respectively. Note that the equation of motion (3.2) is formulated in the vehicle's body frame Σ_c.

Note also that the equilibrium of this system is defined as

$$V^b = O_6,\ \dot{V}^b = O_6, \tag{3.3}$$

and arbitrary body orientations are admissible as the equilibrium points if and only if the vehicle is fully actuated. The control objective is, however, to stabilize the equilibrium at $R_{oc} = I_3,\ p_{oc} = O_{3\times 1}$, and (3.3). This does not lose the generality since we can attach the body frame Σ_c in arbitrary directions relative to the shape of the vehicle.

3.2 Structure

We now parametrize the system model (3.2) with a set of plant parameters. We refer to this set as a *hexarotor structure* since the plant parameters affects the actual mechanical structure.

Definition 3.1. Consider a hexarotor expressed with rotor positions $p_{cr_i} \in \mathbb{R}^3$, rotor orientations $R_{cr_i} \in SO(3)$ and counter torque directions $\varsigma_i \in \{-1, 1\}$ for $i \in \{1, \ldots, 6\}$, vehicle mass $m \in \mathbb{R}$ and an inertia matrix $\mathcal{I} \in \mathbb{R}^{3\times 3}$. A quintuple

$$\mathfrak{s} = (\{p_{cr_1}, \ldots, p_{cr_6}\}, \{R_{cr_1}, \ldots, R_{cr_6}\}, \{\varsigma_1, \ldots, \varsigma_6\}, m, \mathcal{I}) \in \mathfrak{S},$$
$$\mathfrak{S} := (\mathbb{R}^3)^6 \times (SO(3))^6 \times \{-1, 1\}^6 \times \mathbb{R} \times \mathbb{R}^{3\times 3}$$

is called hexarotor structure.

Dynamical characteristics of the vehicle can be described with these variables since they appear in the equation of motion (3.2) as constants. We draw attention to the fact that the relationship between the thrust force and vehicle acceleration varies according to the hexarotor structures, and we analyze the relationship especially for varying positions and orientations of the rotors in this work.

3.2.1 Transformation of Nonplanar Structures

By analyzing the effect of the positions of rotors on the wrench applied to the center of mass, we can see that every hexarotor structure can be transformed into planar structures.

Suppose the orientation of a rotor is constant. For the ith rotor, the thrust force and counter torque are expressed in the body frame Σ_c as in (3.1). By extracting the terms regarding p_{cr_i}, we have

$$\Phi_i = R_{cr_i}(R_{cr_i}^T p_{cr_i})^\wedge f_{r_i r_i}. \tag{3.4}$$

This part is related to torque at the center of mass and is generated only by the rotor thrust force. Furthermore, it is shown that the other parts, translational force and torque due to the rotor counter torque, are not affected by the rotor position. This provides the following important property of the rotors:

Theorem 3.1. Consider a hexarotor UAV model in (3.2). The wrench F_c applied to the center of mass does not change according to the position translation of rotors in the thrust force directions.

Proof. We first substitute the rotor position p_{cr_i} with the following equation using $e_3 = [0\ 0\ 1]^\top$:

$$p_{cr_i} = p'_{cr_i} + cR_{cr_i}e_3.$$

Here, $c \in \mathbb{R}$ is a parameter, and $R_{cr_i}e_3 \in \mathbb{R}^3$ is a directional unit vector of the thrust force. The above equation expresses the translation of the rotor in the thrust force direction. Assigning this to (3.4) yields

$$\begin{aligned}\Phi_i &= R_{cr_i}\left(R_{cr_i}^\top p'_{cr_i} + ce_3\right)^\wedge f_{r_i r_i} \\ &= R_{cr_i}(R_{cr_i}^\top p'_{cr_i})^\wedge f_{r_i r_i} + R_{cr_i}\left(ce_3 \times f_{r_i r_i}\right).\end{aligned} \tag{3.5}$$

By the fact $e_3 \times f_{r_i r_i} = e_3 \times f_i e_3 = O_{3\times 1}$, it is shown that the equation (3.5) does not depend on c. Therefore, the force and torque are not affected by the translation of rotors along the thrust force axes. □

Remark 3.1. Note that there exist physical parameters varying according to the rotor translation. For example, the position of the center of mass and the moment of inertia might vary but we assume that the change is sufficiently small and negligible. This assumption is reasonable, since practically the dominant mass of the vehicle is from the battery, and other electric components are usually placed near the battery.

By using this property of the UAV, we can obtain a simplified planar structure from nonplanar structures, as shown in Fig. 3.3. We now introduce the following lemma to show that any nonplanar structure can be transformed into a planar structure by this process.

Lemma 3.1. For any set of six lines $\ell_1, \ldots, \ell_6$ on the Euclidean space, there exists at least one plane P that passes through the origin and has an intersection with each line.

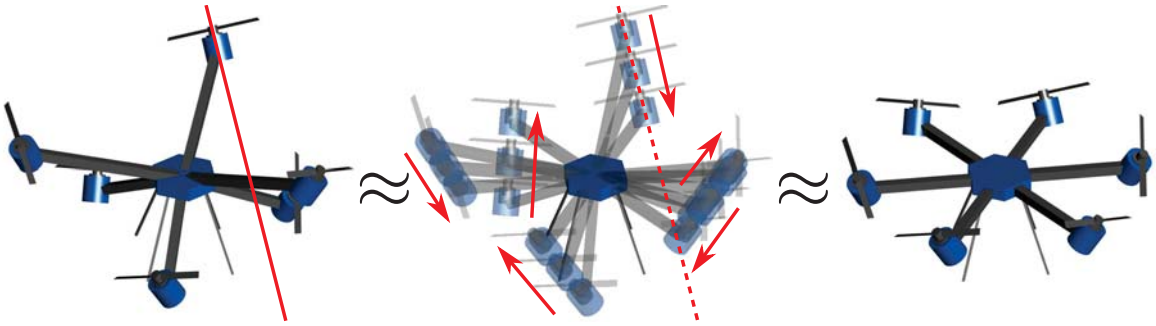

Fig. 3.3: Simplification of a nonplanar structure. By using the unvarying property of the relationship between the rotor thrust force and wrench, we can translate the rotors along their thrust force directions to find an equivalent planar structure.

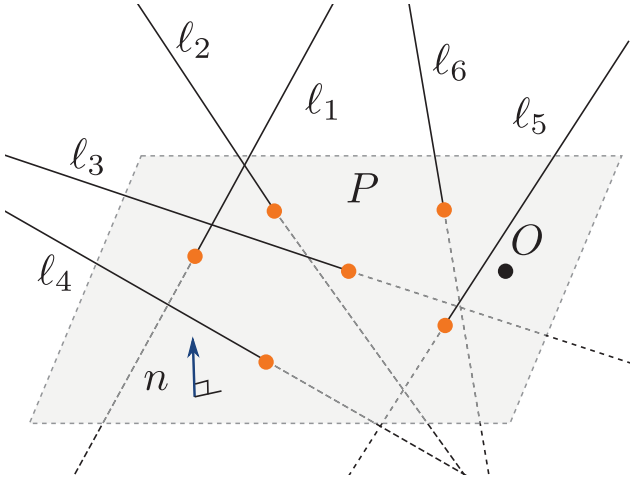

Fig. 3.4: Illustration of Lemma 3.1. According to Lemma 3.1 and Proposition 3.1, every nonplanar hexarotor structure can be transformed into a planar structure while keeping the relation between thrust force and vehicle acceleration.

Proof. It is directly proved by the following facts:

1. There exists a vector that is not perpendicular to a finite number of vectors.
2. A plane that passes through the origin can be uniquely determined for a normal unit vector n.
3. A line ℓ intersects with a plane P if and only if ℓ is not perpendicular to the normal vector n of P.

From 1., there exists a vector n that is not perpendicular to any six lines $\ell_1, \ldots, \ell_6$. A plane P through the origin with its normal vector n is uniquely determined by 2. Then, it follows from 3. that all the six lines intersect with the plane P since they are not perpendicular to the normal vector n. □

The statement is illustrated in Fig. 3.4. From Lemma 3.1, there always exists a plane that has intersections with all the six thrust force axes. Therefore, combined with Proposition 3.1,

it shows that every hexarotor structure can be transformed into a planar structure. The transformation does not alter the relation between thrust input force and vehicle output acceleration. This important property is summarized in the following corollary.

Corollary 3.1. Consider a hexarotor whose positions of rotors are not located on a plane. Then, there exist a planar structure that has the same relation between the thrust force of each rotor and the vehicle wrench at the center of mass.

This corollary greatly reduces the complexity of the problems regarding the wrench as it becomes sufficient to consider only planar structures.

3.2.2 Special Types of Hexarotor Structures

From Corollary 3.1, we can narrow down the target to planar hexarotors. We also suppose several additional assumptions on symmetry to define two special classes of hexarotors.

Symmetric-Coplanar-Tilted-Rotor Structure

We now assume the following symmetry to define a special type of the hexarotor structure.

Definition 3.2. The hexarotor structure satisfying the following conditions for all the rotors ($i \in \{1, \dots, 6\}$) is called *symmetric-coplanar-tilted-rotor (SCTR) structure*.

1. $R_{cr_i} = R_z(\frac{i-1}{3}\pi) R_y(\beta_S) R_x((-1)^{i-1}\gamma_S)$
2. $p_{cr_i} = R_z(\frac{i-1}{3}\pi) \left[r \ 0 \ 0\right]^\top$
3. $\varsigma_i = (-1)^{i-1}$
4. $\mathcal{I}_c = \mathrm{diag}(\mathcal{I}_h, \mathcal{I}_h, \mathcal{I}_v)$

Here, R_x, R_y, $R_z \in SO(3)$ are rotation matrices around x, y, and z axes, respectively. β_S, $\gamma_S \in (-\pi/2, \pi/2)$ are rotor tilt angles, and $r > 0$ is the distance between a rotor and the center of the mass of the vehicle.

For SCTR structures, rotors are placed on the vertexes of a regular hexagon with the radius r, and they are tilted by β_S and γ_S around two axes, as shown in Fig. 3.5. We also assume symmetry of the inertia tensor $\mathcal{I}_c$, which is natural for symmetric hexarotors.

Parallel-Coplanar-Tilted-Rotor Structure

Likewise, we define another special type of the hexarotor structure with different rotor tilt angles.

Definition 3.3. The hexarotor structure satisfying the following conditions for all the rotors ($i \in \{1, \dots, 6\}$) is called *parallel-coplanar-tilted-rotor (PCTR) structure*.

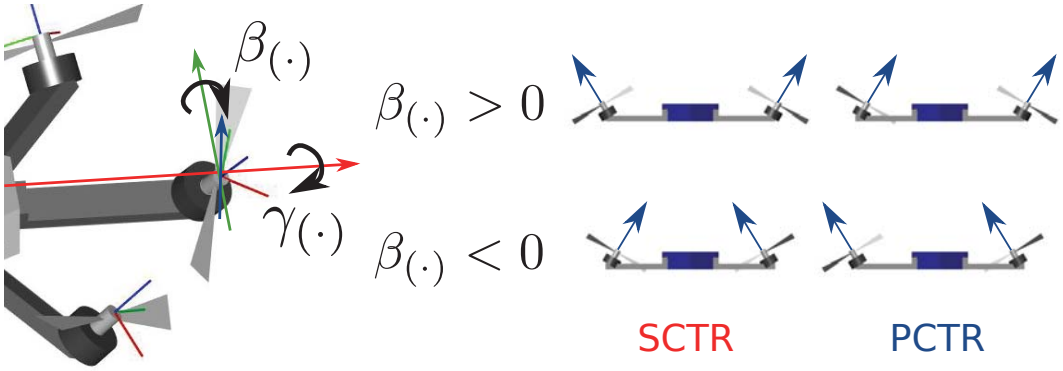

Fig. 3.5: Rotor tilt angles. Rotors are tilted in two axes, and the angles are denoted by $\beta_{(\cdot)}$ and $\gamma_{(\cdot)}$. $\beta_{(\cdot)}$ is the inward/outward angle, and $\gamma_{(\cdot)}$ is the sideward angle. The rotation direction of $\beta_{(\cdot)}$ is different among the two classes of hexarotor structures.

Table 3.1: Classification of related research

SCTR	**PCTR**	**NA**
Jiang [8], Giribet [9], Kotarski [11], Rajappa [12], Mehmood [14, 15]	Toratani [10], Jiang [8], Shimizu [18], Okuma [13], Convens [19]	Park [20]
Kaufman [17], Crowther [16] ($\beta_S = \beta_P = 0$)		—

1. $R_{cr_i} = R_z(\frac{i-1}{3}\pi)R_y((-1)^{i-1}\beta_P)R_x((-1)^{i-1}\gamma_P)$

2), 3), and 4) in Definition 3.2.

As in the first condition, the direction of the outward/inward tilt angle β_P is different from that of the SCTR structure, and it is illustrated in Fig. 3.5. In the PCTR structure, thrust force directions of diagonal rotors are identical. For the special cases $\beta_{(\cdot)} = 0$, the structure belongs to both SCTR and PCTR.

3.2.3 Classification of Hexarotors

In fact, many structures from related research can be classified into SCTR and PCTR structures. Table 3.1 shows the classification summary of hexarotor structures from the following articles: [8–20]. In the following, we describe how to identify the class by giving examples about some of these articles.

Case 1: SCTR Structure

For example, the hexarotor structure illustrated in Fig. 3.6 is proposed by Kotarski et al. [11] and is equivalent to an SCTR structure. Although the rotors are displaced alongside the beams as shown in the figure, the structure can be directly transformed into a planar structure with rotor translation in the thrust force direction.

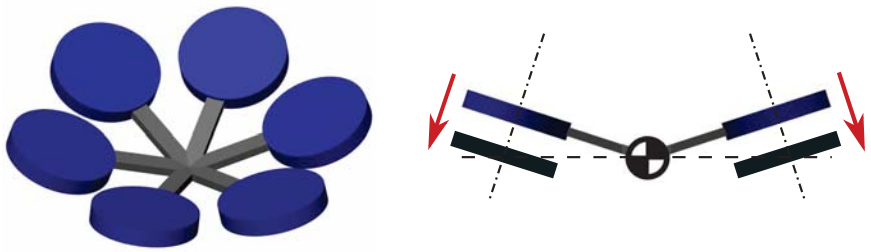

Fig. 3.6: Nonplanar hexarotor in Kotarski et al. [11]. The rotors are tilted and displaced alongside the beams. This structure belongs to SCTR.

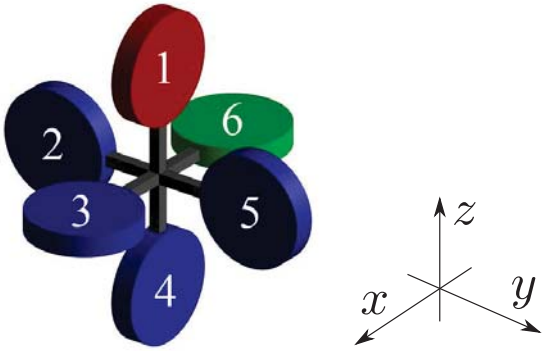

Fig. 3.7: Nonplanar hexarotor in Okuma et al. [13]. The rotors are placed and oriented so that the force and torque vectors can be simply decoupled. The 1st and 6th rotors are, respectively, colored with red and green.

Case 2: PCTR Structure

Another example is the structure presented by Okuma et al. [13] (Fig. 3.7). It is a nonplanar structure that is capable of uniform acceleration in every direction and around every axis. We show that this nonplanar structure belongs to PCTR.

First, p_i and t_i, respectively, denote the position of the ith rotor and the thrust force direction, and they are defined as

$$p_1 = -p_4 = e_3,\ p_2 = -p_5 = -e_2,\ p_3 = -p_6 = e_1,$$
$$t_1 = t_4 = e_2,\ t_2 = t_5 = e_1,\ t_3 = t_6 = e_3.$$

Here, we use the notation $e_1 = [1\ 0\ 0]^\top,\ e_2 = [0\ 1\ 0]^\top,\ e_3 = [0\ 0\ 1]^\top$. We then translate the rotors by ± 1 toward each thrust force direction as in Fig. 3.8 so that the rotor arrangement becomes planar. The translated rotor positions denoted by p'_i become as follows.

$$p'_1 = -p'_4 = e_3 - e_2,\ p'_2 = -p'_5 = e_1 - e_2,\ p'_3 = -p'_6 = e_1 - e_3$$

These position vectors and their linear combinations are perpendicular to a vector $n = [1\ 1\ 1]^\top/\sqrt{3}$ since the inner products are zero. Therefore, all the six rotors are placed on a

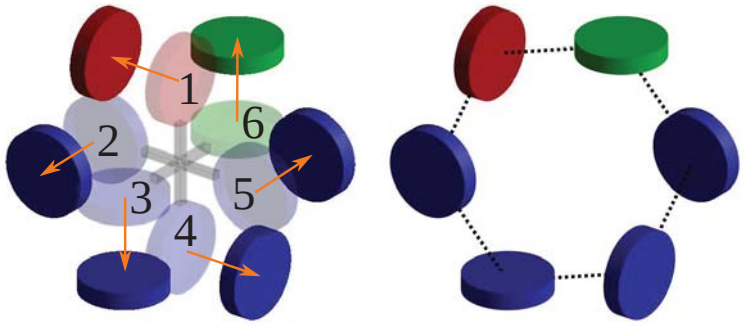

Fig. 3.8: Rotor translation. We can translate the rotors towards a hexagon, and the rotor angles match the conditions in Definition 3.3. Therefore, the structure in Fig. 3.7 belongs to PCTR.

plane normal to n. Moreover, $p'_1, \ldots, p'_6$ form a regular hexagon on the plane as illustrated in Fig. 3.8.

We now calculate the rotation matrix representing the orientation of the frame fixed to the plane. We take the vector n, the normal vector of the plane, as the new z-axis and the direction vector toward p'_1 as the new x-axis. By the orthogonality and the determinant constraint of the rotation matrix, we obtain

$$R_{o\pi} = \begin{bmatrix} 0 & \frac{2}{\sqrt{6}} & \frac{1}{\sqrt{3}} \\ -\frac{1}{\sqrt{2}} & -\frac{1}{\sqrt{6}} & \frac{1}{\sqrt{3}} \\ \frac{1}{\sqrt{2}} & -\frac{1}{\sqrt{6}} & \frac{1}{\sqrt{3}} \end{bmatrix}$$

as the rotation matrix representing the new vehicle frame relative to the original frame.

To determine the rotor tilt angles, we then solve the following equation about the PCTR structure for β_P and γ_P.

$$R_{o\pi}^{\top} t_i = R_z\left(\frac{(i-1)\pi}{3}\right) R_y\left((-1)^{i-1}\beta_P\right) R_x\left((-1)^{i-1}\gamma_P\right) e_3$$

We finally obtain the solution

$$\beta_P = 2\tan^{-1}\left(\sqrt{\frac{2}{3}} - \sqrt{\frac{5}{3}}\right), \ \gamma_P = \tan^{-1}\sqrt{\frac{1}{5}},$$

and thus the nonplanar structure in Fig. 3.7 belongs to PCTR.

Case 3: Not Applicable

The structure proposed by Park et al. [20] is not classified in the two classes, as shown in Table 3.1, because the values of the rotor position and orientation obtained by optimization are not provided in the paper. The structure might belong to PCTR since the rotors are

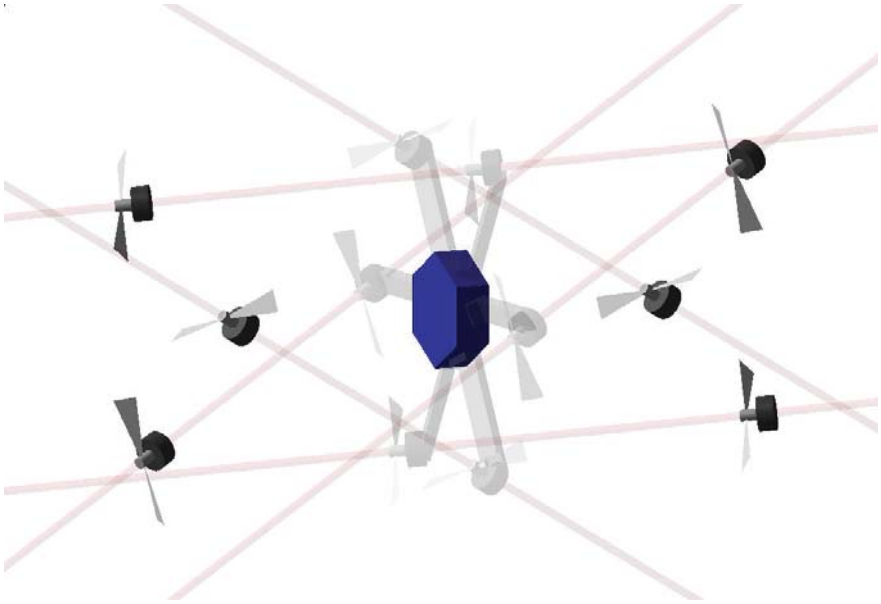

Fig. 3.9: Elongated structure. Structure similar to [20] can be derived from a kind of parallel-coplanar-tilted-rotor structure.

tilted in a similar manner, as shown in Fig. 3.9.

Remark 3.2. Although most of the related research seems to treat different types, the structure is classified into the SCTR or PCTR structure. This suggests that there exists room for further investigation into different types of fully actuated hexarotors. However, it is difficult to obtain meaningful force relations for asymmetrically or randomly placed rotors. Moreover, an asymmetrical structure has a practical problem of unbalanced load among rotors, leading to energy inefficiency or frequent breakdown of a certain rotor. For these reasons, we consider these special classes throughout this dissertation.

3.3 Manipulability Analysis

We now evaluate the full-actuation capability of a hexarotor by considering the mapping from the rotors' thrust force to the vehicle acceleration. This leads to the definition of dynamic manipulability of the hexarotor, which is newly defined in this research. The dynamic manipulability is used to visualize and compare the acceleration characteristics of hexarotor structures.

3.3.1 Dynamic Manipulability of Hexarotor UAV

The dynamic manipulability is an index quantifying the ability of omnidirectional acceleration and has been widely used in the field of robot manipulators since it was proposed by Yoshikawa [63]. The definition of conventional dynamic manipulability for a robot manipulator requires a matrix called manipulator Jacobian describing the relationship between the

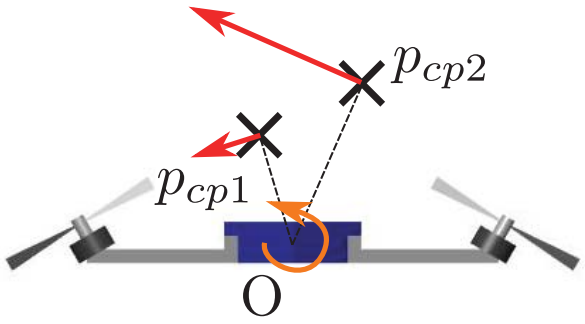

Fig. 3.10: Effect of p_{cp}. Output points p_{cp} are considered since the translational motion depends on the output point.

joint velocity and the Cartesian velocity of the output point. However, hexarotors do not have any joints. Therefore, an adapted version of the dynamic manipulability suited to the hexarotor is considered in this work.

We now consider a point attached to the vehicle coordinate frame Σ_c as the output point of the UAV. This is because the translational acceleration of the point depends on the position relative to the center of mass, as shown in Fig. 3.10. We also assume that the initial state of the vehicle is at the origin with gravitational compensation applied. This means that the position, attitude angles, the translational and rotational velocity are all zero, and the vehicle remains still in the air. The translational and angular acceleration at an output point $p_{cp} \in \mathbb{R}^3$ in Σ_c are written as

$$\begin{bmatrix} \dot{v}_p^b \\ \dot{\omega}_p^b \end{bmatrix} = \begin{bmatrix} I_3 & -\hat{p}_{cp} \\ O_3 & I_3 \end{bmatrix} \begin{bmatrix} mI_3 & O_3 \\ O_3 & \mathcal{I}_c \end{bmatrix}^{-1} F_c.$$

By differentiating this by the rotors thrust force $f = [f_1, \ldots, f_6]^\top \in \mathbb{R}^6$, we obtain the following matrix describing the relationship between the rotor thrust force and the vehicle acceleration:

$$\Gamma = \frac{\partial}{\partial f} \begin{bmatrix} \dot{v}_p^b \\ \dot{\omega}_p^b \end{bmatrix} = \begin{bmatrix} \Gamma_t \\ \Gamma_r \end{bmatrix} \in \mathbb{R}^{6\times 6}. \tag{3.6}$$

Here, $\Gamma_t, \Gamma_r \in \mathbb{R}^{3\times 6}$ are submatrices of Γ corresponding to the translation and rotation. Using these matrices, we finally define the DMM of the hexarotor UAV as follows.

Definition 3.4. Consider a point $p_{cp} \in \mathbb{R}^3$ attached to Σ_c. Then, the absolute value of the determinant of the matrix Γ in (3.6) at p_{cp}, namely $w_d = |\det(\Gamma)| = \sqrt{\det(\Gamma\Gamma^\top)} \geq 0$, is called *DMM of the hexarotor UAV at the output point* p_{cp}. Moreover, $w_{dt} = \sqrt{\det(\Gamma_t\Gamma_t^\top)} \geq 0$ and $w_{dr} = \sqrt{\det(\Gamma_r\Gamma_r^\top)} \geq 0$ are called *translational and rotational DMM at the output point* p_{cp}, respectively.

The DMM of the hexarotor evaluates the input-to-output relationship between the rotors

thrust force and the vehicle acceleration, whereas that of a robot manipulator associates the joint torque with the end effector acceleration. This definition is a natural application of DMM to the hexarotor UAV. In the case of $w_d = 0$, the UAV cannot accelerate in a certain direction or around a certain axis because the degrees of freedom are lost, and DMM of robot manipulators also has the same property.

Definition 3.5. The set of feasible acceleration $u = [\dot{v}^\top \ \dot{\omega}^\top]^\top$ of the output point $p_{cp} \in \mathbb{R}^3$ with unit spherical input thrust force $f_1, \ldots, f_6$ becomes a 6-dimensional ellipsoid

$$u^\top (\Gamma\Gamma^\top)^{-1} u = 1$$

and is called dynamic manipulability ellipsoid (DME) of the hexarotor at p_{cp}.

We can calculate the principal axes of the DME by singular value decomposition of the Jacobian matrix Γ. The singular vectors represent the directions of the acceleration, and the associated singular values are the magnitude for each direction. Moreover, the volume of the DME is proportional to DMM, indicating that the manipulability increases as the ellipsoid becomes large.

Remark 3.3. In the definition of DMM and DME, the force of gravity is compensated, and the thrust force is not limited. Hence, the value of DMM does not depend on the orientation of the body frame Σ_c. On the other hand, the DME is rotated according to the body frame rotation while the shape and the scale of the DME does not change. Therefore, the dynamic manipulability is a suitable measure for the evaluation of the structure itself.

3.3.2 Properties of Manipulability for Special Structures

In this section, we derive the DMM of the hexarotor UAV with the SCTR or PCTR structure in detail for the preparation of the main results of this chapter.

Lemma 3.2. DMM w_d of a hexarotor UAV with the SCTR or PCTR structure at the output point p_{cp} can be written as follows.

$$w_d = \sqrt{\det\left((\Gamma_t + (\widehat{p}_{cp} - \widehat{p}_{cq})\Gamma_r)\Gamma_t^\top\right) \det\left(\Gamma_r \Gamma_r^\top\right)} \tag{3.7}$$

Here, $p_{cq} = [0 \ 0 \ z_q]^\top$ is a special point fixed to the vehicle frame, and z_q is

$$z_q = \frac{\mathcal{I}_h r \cos(\beta_S)\cos^2(\gamma_S)\sin(\beta_S)}{m\left(\kappa^2 - \kappa^2\cos^2(\beta_S)\cos^2(\gamma_S) + r^2\cos^2(\beta_S)\cos^2(\gamma_S) + \kappa r\cos(\beta_S)\sin(2\gamma_S)\right)}$$

for SCTR structures, and $z_q = 0$ for PCTR structures.

Proof. Suppose that $\Gamma_r\Gamma_r^\top$ is a nonsingular matrix. Then, by using the property of the determinant of block matrices [64], we obtain

$$\begin{aligned}\det(\Gamma\Gamma^\top) &= \det\begin{bmatrix}\Gamma_t\Gamma_t^\top & \Gamma_t\Gamma_r^\top\\ \Gamma_r\Gamma_t^\top & \Gamma_r\Gamma_r^\top\end{bmatrix} \\ &= \det\left(\Gamma_t\Gamma_t^\top - \Gamma_t\Gamma_r^\top(\Gamma_r\Gamma_r^\top)^{-1}\Gamma_r\Gamma_t^\top\right)\det(\Gamma_r\Gamma_r^\top).\end{aligned} \tag{3.8}$$

Moreover, assigning the relationship between Γ_r and Γ_t, that is,

$$\Gamma_t = \frac{1}{m}\frac{\partial}{\partial f}f_c - \hat{p}_{cp}\Gamma_r, \tag{3.9}$$

to (3.8) yields

$$\begin{aligned}\Gamma_t\Gamma_r^\top(\Gamma_r\Gamma_r^\top)^{-1} &= \left(\frac{1}{m}\frac{\partial}{\partial f}f_c - \hat{p}_{cp}\Gamma_r\right)\Gamma_r^\top(\Gamma_r\Gamma_r^\top)^{-1} \\ &= \frac{1}{m}\left(\frac{\partial}{\partial f}f_c\right)\Gamma_r^\top(\Gamma_r\Gamma_r^\top)^{-1} - \hat{p}_{cp}.\end{aligned}$$

Finally, direct calculation considering assumptions of the SCTR or PCTR structure yields

$$\begin{aligned}\frac{1}{m}\left(\frac{\partial}{\partial f}f_c\right)\Gamma_r^\top(\Gamma_r\Gamma_r^\top)^{-1} &= (\begin{bmatrix}0 & 0 & z_q\end{bmatrix}^\top)^\wedge = \hat{p}_{cq}, \\ \Gamma_t\Gamma_r^\top(\Gamma_r\Gamma_r^\top)^{-1} &= \hat{p}_{cq} - \hat{p}_{cp}.\end{aligned} \tag{3.10}$$

Then, combining (3.8) and (3.10) results in (3.7). □

Remark 3.4. In the proof above, we assume that the matrix $\Gamma_r\Gamma_r^\top$ is nonsingular. This assumption is always true in this work since only fully actuated hexarotors are considered.

Remark 3.5. p_{cq} is an unique point in Σ_c associated with the structure of the UAV. In the special case $\gamma = 0$ and $\kappa \ll 1$, this point can be interpreted as the center of percussion of the vehicle. At such a point, the horizontal acceleration is eliminated. In other words, the following acceleration cancels each other.

1. The horizontal acceleration by the sum of thrust force.

2. The horizontal acceleration of the point generated by the torque applied to the center of mass.

Therefore, the translational and rotational motion is considered to be decoupled at the unique point p_{cq}.

3.3.3 Invariance of DMM

The two special types of the hexarotor structure provides an important property; invariance of the DMM under the output point of the vehicle. If the hexarotor has this characteristic, the DMM is not influenced by the output point. Therefore, we can say that it can be used as an performance index describing the structure itself and is uniquely determined by the structure. First, we have the following lemma:

Lemma 3.3. Rotational DMM w_{dr} of a hexarotor UAV with the SCTR or PCTR structure is invariant under the output point p_{cp}.

Proof. The proof is straightforward. By the definition of Γ, Γ_r is written as

$$\Gamma_r = \frac{\partial}{\partial f}\left(\mathcal{I}_c^{-1}\tau_c\right),$$

where $\mathcal{I}_c \in \mathbb{R}^{3\times 3}$ is a constant matrix, and $\tau_c \in \mathbb{R}^3$ is the torque applied to the center of mass. Therefore, Γ_r does not depend on the output point, and as a result, $w_{dr} = \sqrt{\det(\Gamma_r\Gamma_r^\top)}$ is invariant under p_{cp}. □

We now state the one of the main analysis results for the hexarotor UAVs with the SCTR or PCTR structure, using Lemmas 3.2 and 3.3.

Theorem 3.2. DMM w_d of a hexarotor UAV with the SCTR or PCTR structure is invariant under the output point p_{cp}.

Proof. We show that $\det\left((\Gamma_t + (\hat{p}_{cp} - \hat{p}_{cq})\Gamma_r)\Gamma_t^\top\right)$ is invariant since the invariance of $\det(\Gamma_r\Gamma_r^\top)$ has been proved in Lemma 3.3. First, the equation (3.9) yields

$$(\Gamma_t + (\hat{p}_{cp} - \hat{p}_{cq})\Gamma_r)\Gamma_t^\top = \left(\frac{1}{m}\frac{\partial}{\partial f}f_c - \hat{p}_{cq}\Gamma_r\right)\left(\frac{1}{m}\frac{\partial}{\partial f}f_c - \hat{p}_{cp}\Gamma_r\right)^\top.$$

Then, by extracting the terms regarding p_{cp} from the above equation, we obtain

$$\begin{aligned}\left(\frac{1}{m}\frac{\partial}{\partial f}f_c - \hat{p}_{cq}\Gamma_r\right)(-\hat{p}_{cp}\Gamma_r)^\top &= -\frac{1}{m}\frac{\partial}{\partial f}f_c\left(\Gamma_r^\top - \Gamma_r^\top(\Gamma_r\Gamma_r^\top)^{-1}\Gamma_r\Gamma_r^\top\right)\hat{p}_{cp}\\ &= O_3.\end{aligned}$$

This equation shows that $\det\left((\Gamma_t + (\hat{p}_{cp} - \hat{p}_{cq})\Gamma_r)\Gamma_t^\top\right)$ is invariant under p_{cp}. Therefore, DMM of a hexarotor UAV with the SCTR or PCTR structure is invariant under the output point. □

Now, we briefly summarize Lemma 3.3 and Theorem 3.2. These theorems show that the total DMM w_d and rotational DMM w_{dr} are invariant under p_{cp}. On the other hand, the translational DMM w_{dt} varies depending on the output point since the translation motion of the vehicle depends on the position of the output point.

3.3.4 Separation and Decomposition of DMM

Based on the previous discussions, another important theorem and its corollary are acquired.

Theorem 3.3. The DMM of the hexarotor with the SCTR or PCTR structure at the special output point $p_{cq} = [0\ 0\ z_q]^\top$ is decomposed into elements about six translational and rotational axes.

$$w_d = \sigma_{tx}\sigma_{ty}\sigma_{tz}\sigma_{rx}\sigma_{ry}\sigma_{rz}$$

Here, $\sigma_{t(\cdot)}$ and $\sigma_{r(\cdot)}$ are the DMMs about translational and rotational axes, respectively, for $(\cdot) \in \{x, y, z\}$, and z_q is determined uniquely to the structure.

Corollary 3.2. DMM w_d of a hexarotor UAV with the SCTR or PCTR structure at p_{cq} in the equation (3.7) is equal to the product of w_{dt} and w_{dr}, that is,

$$w_d = w_{dt} w_{dr}. \tag{3.11}$$

Proof. By substituting the output point $p_{cp} = p_{cq}$ into (3.7), the DMM w_d at the special point becomes

$$w_d = \sqrt{\det(\Gamma_t \Gamma_t^\top)\det(\Gamma_r \Gamma_r^\top)} = w_{dt} w_{dr},$$

which leads to (3.11). Moreover, $\Gamma_t\Gamma_t^\top$ and $\Gamma_r\Gamma_r^\top$ become diagonal, and $\Gamma_r\Gamma_t^\top = O_3$ holds for both SCTR and PCTR structures. Since the determinant of a diagonal matrix is the product of the diagonal elements, the DMM at the special point p_{cq} can be decomposed into the product of the DMMs about each axis, and now we have

$$w_{dt} = \sigma_{tx}\sigma_{ty}\sigma_{tz},\ w_{dr} = \sigma_{rx}\sigma_{ry}\sigma_{rz}.$$

The values of $\sigma_{t(\cdot)}$ and $\sigma_{r(\cdot)}$ are written in Appendix A.2. □

From Corollary 3.2, two important results can be stated when we choose p_{cq} as the output point of DMM.

1. The translational and rotational DMM can be separately considered. We can use each DMM in mechanical or control design to characterize the translational and rotational maneuverability of the hexarotor.

2. Scalar multiplication of each DMM does not affect the shape of the total DMM w_d except for the scale. Namely, we can ignore the difference of units between translation and rotation.

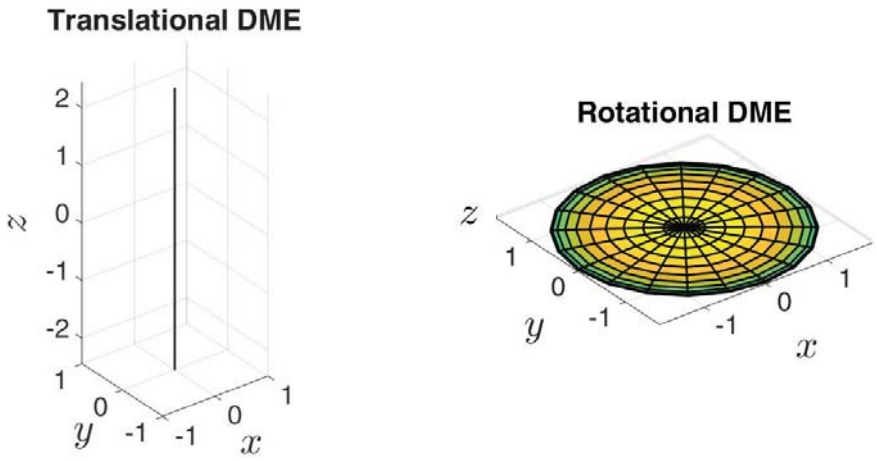

Fig. 3.11: DME of conventional parallel hexarotor. The translational DME has no volume since the vehicle can only accelerate in the z-axis. The total DMM is zero, and this means that the vehicle is underactuated.

Therefore, the translational, rotational, and the total DMM at p_{cq} can be used as full-actuation performance indices characterizing the structure of the UAV itself.

Moreover, the singular values of Γ at p_{cq} correspond to the square root of the diagonal elements of $\Gamma\Gamma^\top$, and the singular vectors are the standard bases of 6-dimensional space. As a result, we can visualize the 6-dimensional DME by two 3-dimensional DMEs about translation and rotation since they are decoupled at p_{cq}. The rotor distance r, mass m, and inertia $\mathcal{I}_v, \mathcal{I}_h$ are all set to 1, and the counter torque constant κ is 0.01 m in the following examples.

First, we show the translational and rotational DMEs of a conventional parallel hexarotor in Fig. 3.11. The translational DME has no volume, and thus the total DMM becomes $w_d = 0$. This means that the vehicle cannot accelerate in horizontal directions, and the system is underactuated.

The nonparallel structure in Fig. 1.2(b) is proposed by [17], and it belongs to both SCTR and PCTR. The rotor is tilted so that it becomes perpendicular to the next rotor, and the tilt angles are $\beta = 0,\ \gamma = \tan^{-1}\sqrt{2}$. The DMEs of the structure are shown in Fig. 3.12. The translational DME is spheric since the vehicle can evenly accelerate in any directions. On the other hand, we observe the largest singular value for the z-axis of the rotational DME meaning that it can rotate more quickly around z-axis than the other axes. The value of the DMM is $w_d = 5.7768$, which is 85% of the maximum DMM. This indicates that the vehicle has both capabilities of isotropic translational acceleration and agile rotation.

The nonplanar structure from [13] shown in Fig. 3.7 belongs to PCTR structure, as stated in the previous section. The structure is designed so that the vehicle can translate and rotate evenly in any directions and around any axes. Both the translational and rotational DMEs are spherical, as shown in Fig. 3.13, and this proves the design concept. However, the total DMM $w_d = 2.8284$ is less than half of that of the nonparallel structure in the second example,

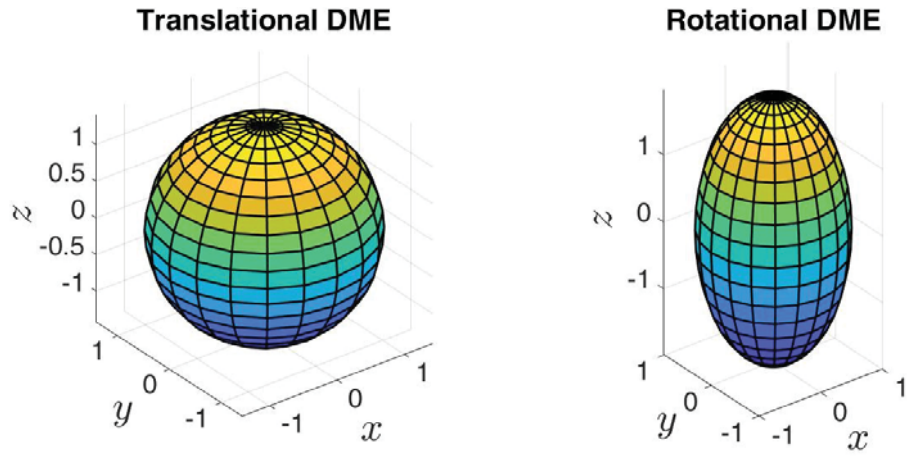

Fig. 3.12: DME of nonparallel hexarotor proposed by [17]. As the structure is designed to be capable of uniform translational acceleration, the translational DME is a sphere. In contrast, the rotational DME is stretched toward the z-axis.

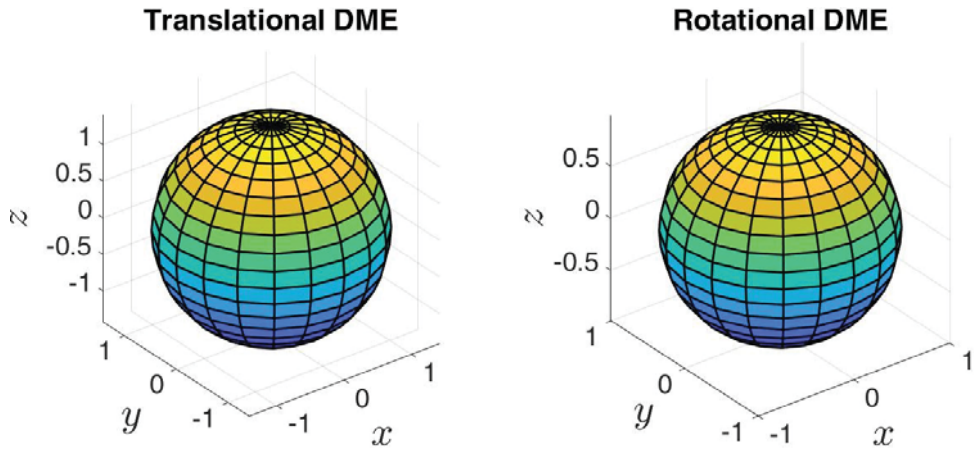

Fig. 3.13: DME of nonplanar structure proposed by [13]. The structure belongs to PCTR. It is designed for uniform acceleration in every direction, and the spherical DMEs reflect the design principle.

in trade for the isotropic acceleration characteristics.

From the examples above, we can state that the DME and DMM are well suited to the evaluation of acceleration characteristics of hexarotor with SCTR and PCTR structures. Moreover, by using Theorem 3.1 and Lemma 3.1, we have shown that we can treat not only planar structures but also many nonplanar structures.

3.4 Experimental System

In this section, we describe the experimental system and perform a preliminary experiment. The experimental system is designed so that all the computation regarding control can be performed on the vehicle. Due to the small space of the room, we also need to make the

Fig. 3.14: Experimental vehicle.

vehicle as small as possible. Therefore, the challenge of the system design is the tradeoff between power, in the sense of both mechanics and computation, and dimensions of the vehicle.

3.4.1 System Description

Hardware

Fig. 3.14 is a picture of the experimental vehicle. Mechanical constants of the vehicle are shown in Table 3.2. The main frame and rotor arms of the vehicle are made of carbon fiber reinforced polymer, and they are connected with 3D printed adapter parts. We can reconfigure the rotor tilt angles freely by replacing the adapter parts.

Each rotor is made out of a Turnigy MultiStar Viking 1808 brushless DC motor with the KV value 2600 and a 4-inch propeller whose pitch is 4 inch. The motors are driven by MultiOne 20A speed controllers at the PWM frequency 400 Hz. The battery is a Hyperion G7 silicon-graphene lithium battery packed with 3 cells (nominal voltage 11.1V) with the capacity 1300 mAh.

Software

Figure 3.15 shows the system diagram of the experimental system. The control laws are implemented on a Raspberry Pi 3B+ single-board computer and a 3D Robotics Pixhawk

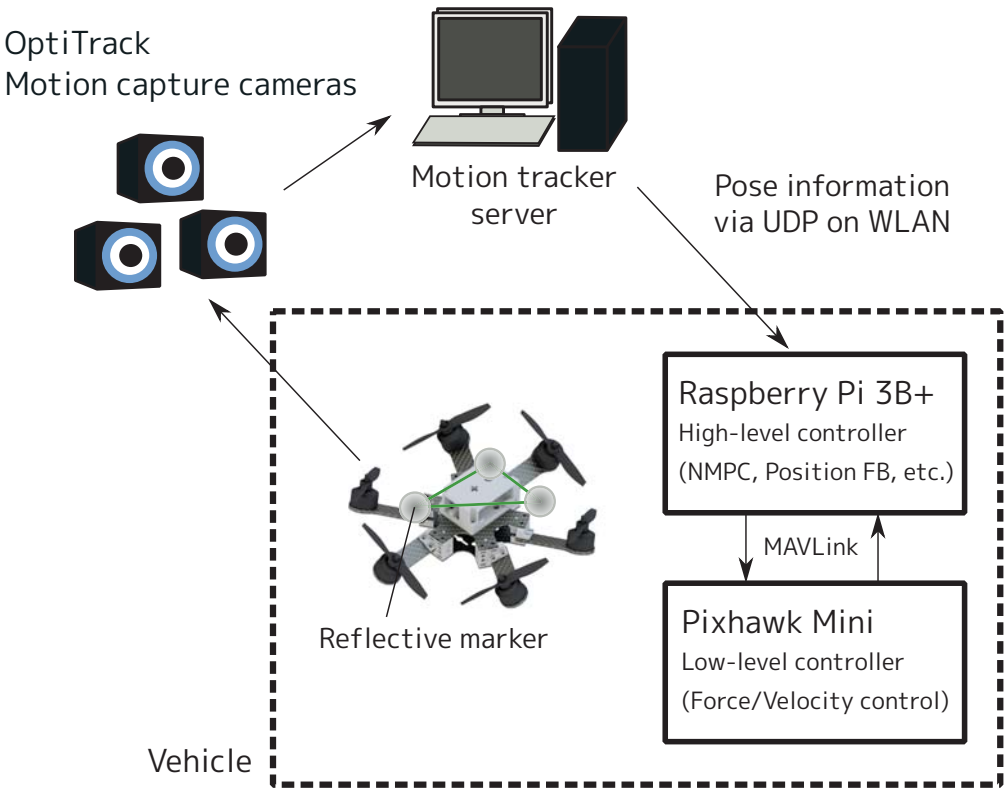

Fig. 3.15: Experimental system.

Table 3.2: Mechanical constants

m	0.63	kg
$\mathcal{I}_h$	2.5×10^{-3}	kg·m^2
$\mathcal{I}_v$	4.6×10^{-3}	kg·m^2
r	0.11	m
κ	0.016	m
$f_{\max}$	3	N

Mini flight controller [65] by using Simulink and Embedded Coder support packages from MathWorks [66], [67]. On Raspberry Pi, a high-level controller such as nonlinear model predictive control or position feedback control is performed. On the other hand, a low-level force or velocity controller runs on Pixhawk Mini. The pose of the vehicle is measured by OptiTrack motion tracking system [68] by observing the reflective markers on the body. The pose data is sent to the high-level flight controller via UDP on wireless LAN. The twist is estimated using a backward Euler method, and it is smoothed by a low-pass filter. Raspberry Pi and Pixhawk Mini communicate with each other in MAVLink protocol [69] on a USB virtual serial port to command the control input and gather the sensor data.

Safety Feature

The "arming" command that enables or disables the rotors' outputs is continuously sent from Raspberry Pi to Pixhawk Mini. Timestamp is attached with the pose information, and the safety program checks if new data are available or not. To ensure safety, if the arming command or pose information is not received for a certain time period, the flight controller safely stops all the rotors regardless of the control input signals.

3.4.2 Preliminary Experiment

As a preliminary experiment, we check that the vehicle is capable of simultaneous linear and angular acceleration. Regular types of multirotors such as shown in Fig. 1.1 are underactuated, and they cannot accelerate horizontally without using body tilt. To prove the full-actuation property of the fully actuated hexarotor, we tackle position feedback control *without* tilting the body. We have used the hexarotor structure only with the sideward tilt angle $\gamma = 0.4234$ rad, which can be classified as SCTR or PCTR structure.

The pose controller runs on Raspberry Pi, and Pixhawk controls the body acceleration and angular velocity with a PID controller. The high-level pose controller is based on a double-geodesic PD controller on $SE(3)$, which will be described in Section 4.2, and it generates the reference acceleration and angular velocity of the vehicle. The low-level PID controller then computes the reference wrench F_c of the vehicle body, and the wrench is transformed and distributed to the thrust force of the 6 rotors by using the following equation:

$$f = \begin{bmatrix} f_1 \\ \vdots \\ f_6 \end{bmatrix} = \begin{bmatrix} R_{cr_1} e_3 & \dots & R_{cr_6} e_3 \\ \widehat{p}_{cr_1} R_{cr_1} e_3 + \varsigma_1 \kappa R_{cr_1} e_3 & \dots & \widehat{p}_{cr_6} R_{cr_6} e_3 + \varsigma_6 \kappa R_{cr_6} e_3 \end{bmatrix}^{-1} F_c. \tag{3.12}$$

Note that the inverted matrix in (3.12) is nonsingular if and only if the vehicle is fully actuated. We cannot measure the thrust force of each rotor in this system, and hence the translational acceleration is controlled by a feedforward input. All the computations are done in real time on the hexarotor, and no computation is performed on the ground.

In this experiment, the vehicle is first commanded to stay at the initial position, and then at $t = 41$ s, the reference y coordinate is changed to 1. The reference attitude and twist are set to $R_{oc} = I_3$ and $V_c^b = O_{6\times 1}$, respectively. Figures 3.16 and 3.17, respectively, show the time evolution of the states (pose and twist) and inputs. As seen in the lower plot in Fig. 3.16(a), the rotation angles around x and y axes remain smaller than 0.05 rad. At the same time, the acceleration in y direction is realized, as shown in Fig. 3.17(a). In Fig. 3.17(b), the time response of the y-acceleration to the reference value is presented. Although the transient error is observed, we can see that the vehicle immediately responds to the change in reference acceleration. This result reflects the full-actuation capability of

the presented hexarotor. This is also confirmed by the pose trajectory during the experiment illustrated in Fig. 3.18.

Note that the state information in the high-level controller has a latency of approximately 0.15 s, as shown in Fig. 3.19. ω_{pix} and ω_{rpi} in the plot denote the angular velocity around the z axis estimated on the low-level controller (Pixhawk) and high-level controller (Raspberry Pi), respectively. This is because the pose information is transferred with a time delay from the motion tracker server to the high-level controller. To bypass this latency, we send the inertial sensor values from the Pixhawk to the Raspberry Pi so that the high-level controller can access the latency-free information on the angular velocity and acceleration.

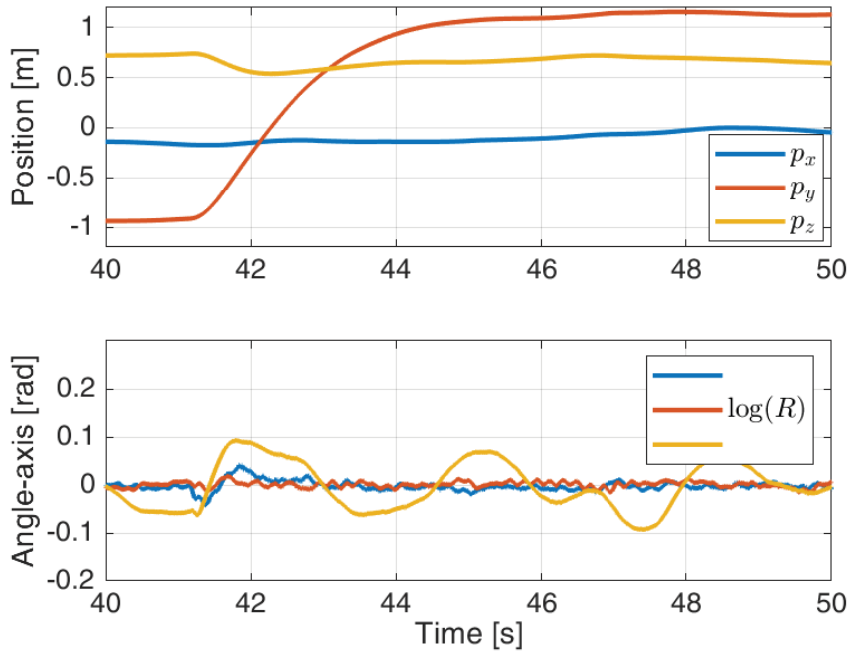

(a) Pose

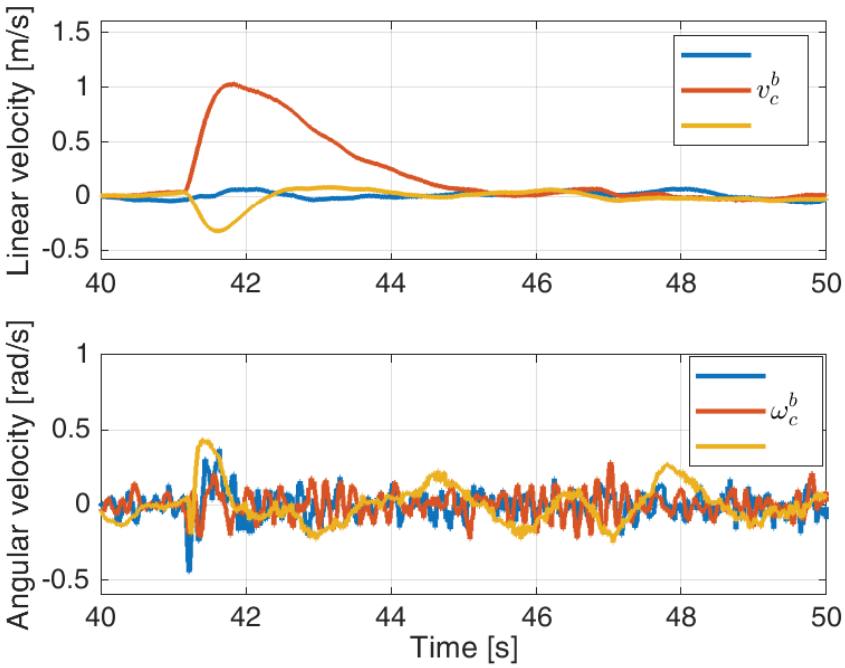

(b) Twist

Fig. 3.16: Time evolution of states (preliminary experiment)

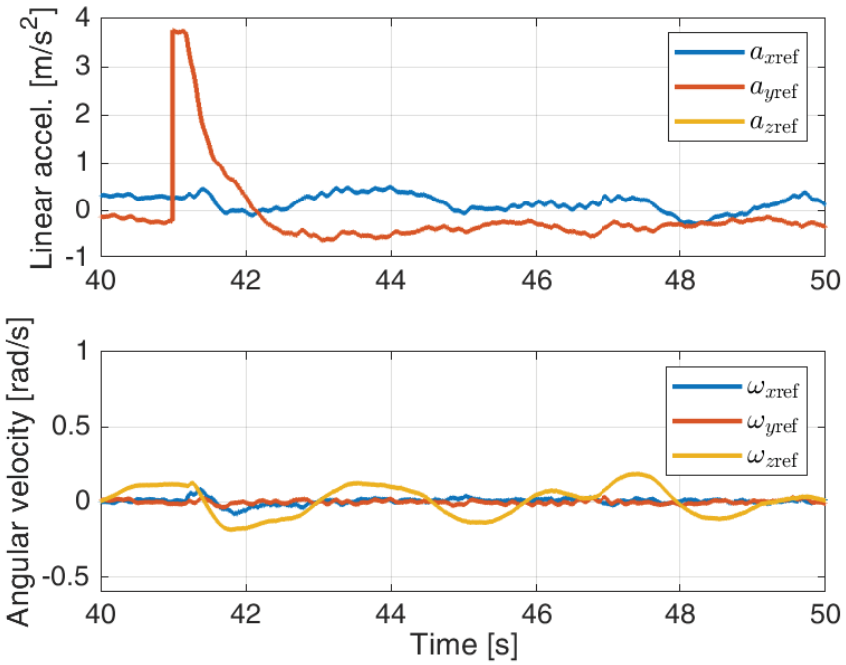

(a) Control input

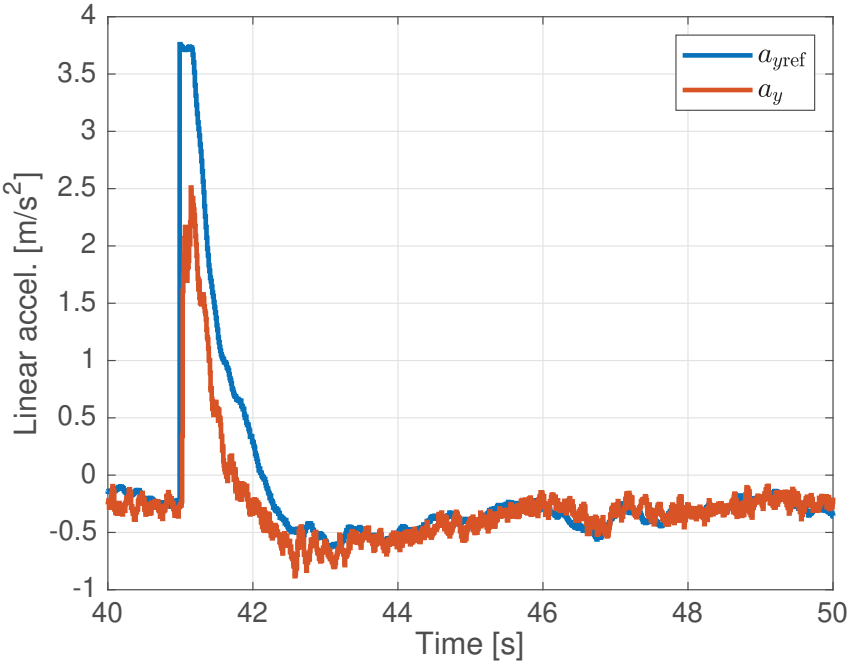

(b) Response

Fig. 3.17: Time evolution of inputs (preliminary experiment)

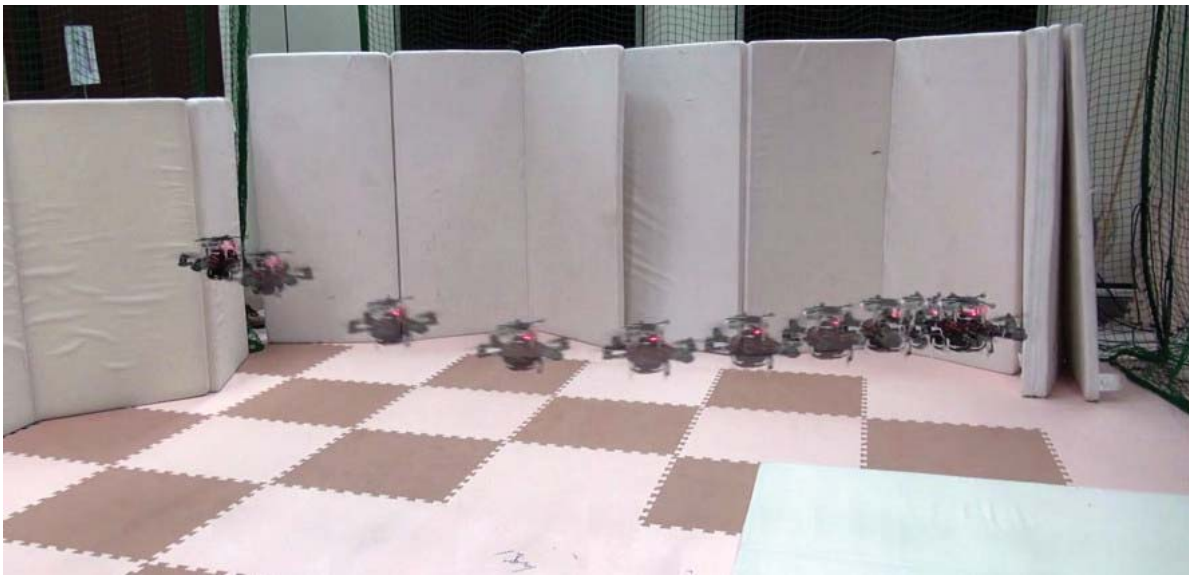

Fig. 3.18: Sequence of poses during the preliminary position control experiment. 11 frames sampled every 0.4 s from the video is manually composited for the illustration purpose. The experiment confirms that the fully actuated hexarotor can linearly accelerate independently from the angular acceleration.

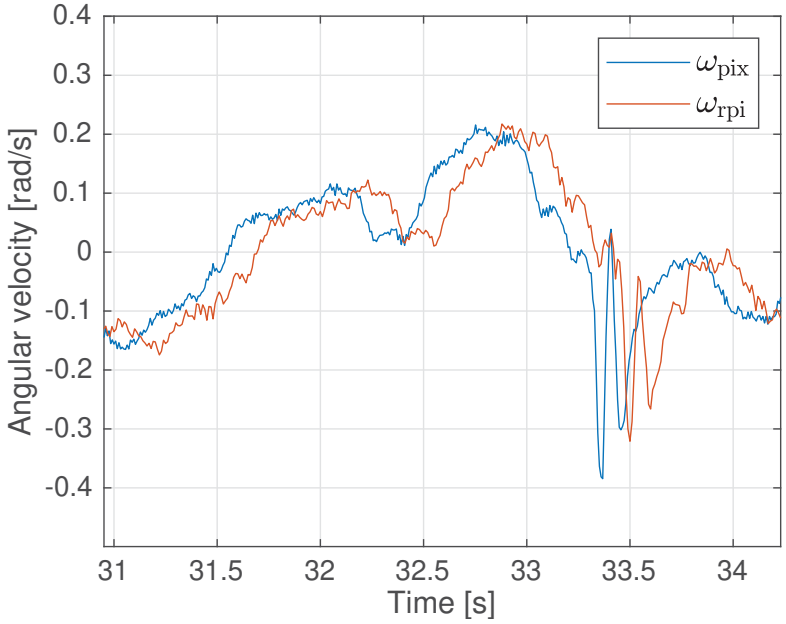

Fig. 3.19: Latency of the state information. Due to the communication delay from the motion capture system, the state information has a latency of approximately 0.15 s.

3.5 Chapter Summary

In Section 3.1, we have introduced the dynamical model of a fully actuated hexarotor unmanned aerial vehicle based on rigid body dynamics and aerodynamics.

In Section 3.2, Theorem 3.1 and Lemma 3.1 prove that any nonplanar structures can be simplified and transformed into planar structures while preserving the force and torque applied to the center of mass. We have also defined two special classes of fully actuated hexarotors and it is shown that many hexarotor structures from related research can be classified into these two classes.

Section 3.3 defines dynamic manipulability of the hexarotor as the performance index of full-actuation capability. We have analyzed the manipulability considering the change of rotor arrangement and tilt angles, and Theorems 3.2 and 3.3 prove 2 important properties of the dynamic manipulability of the hexarotor; invariance and decomposition. With these properties, we can ensure that the dynamic manipulability expresses the characteristics of the vehicle structure itself.

We have also introduced our experimental vehicle and its testbed in Section 3.4. The preliminary experiment shows that the vehicle can accelerate in any direction while maintaining the attitude, which reflects the full-actuation capability of the presented hexarotor.

Chapter 4

Analytic Optimization Method

This chapter develops an analytic joint optimization scheme for a fully actuated hexarotor under zero gravity. An optimal control problem provides the best control law regarding an objective function for a specified dynamical system. We focus on the fact that the objective function can be further minimized with respect to the plant parameters. As the byproduct of the optimal control problem, we obtain the value function, which calculates the optimized value of the objective function. Towards the optimal plant parameter design, the minimization of the value function is considered in an analytical way. The analytical method has an advantage over the numerical method that will be developed in Chapter 5 because we can derive a state feedback controller with stability assurance rather than the numerical sequence of control inputs. This joint optimization method based on the analytic value function is one of the main results of this work.

The rest of this chapter is organized as follows. Before showing the main results, we demonstrate the idea of the analytic joint optimization method by showing parameter optimization based on LQR in Section 4.1. Then, in Section 4.2, we derive an optimal control law for a dynamical system on the special Euclidean group $SE(3)$. Based on the Bellman's principle of dynamic programming, we obtain the HJB equation as the necessary and sufficient conditions of optimality. We show the analytical solutions, the optimal control input and the corresponding value function, by directly solving the HJB equation. Section 4.3 considers a joint optimization problem based on the analytic optimal control. At the end of the section, an application to a fully actuated hexarotor UAV shows that the minimization of the value function results in maximization of dynamic manipulability of the hexarotor. Section 4.4 summarizes this chapter. This chapter is written based on the author's previous work [32] [1].

[1] ©2018 IEEE. Partly reprinted, with permission, from [32].

4.1 Joint Optimization for Linear Systems

In this section, we show an outline of the analytical joint optimization method by considering a general parametrized linear system. Consider a linear system

$$\dot{x} = A(\theta)x + B(\theta)u,$$

where $x \in \mathbb{R}^{n_x}$ and $u \in \mathbb{R}^{n_u}$ are, respectively, the state and control input, $\theta \in \mathbb{R}^{n_\theta}$ is a vector of plant parameters, $A(\theta) \in \mathbb{R}^{n_x \times n_x}$, and $B(\theta) \in \mathbb{R}^{n_x \times n_u}$. We assume that the system is $(A(\theta), B(\theta))$ controllable. We now solve an LQR problem minimizing an objective function

$$J = \int_0^\infty \left(x^\top Q_x x + u^\top Q_u u\right) dt,$$

where $Q_x \in \mathbb{R}^{n_x \times n_x}$ and $Q_u \in \mathbb{R}^{n_u \times n_u}$ are weight matrices. It is well-known that the optimal value function of this problem is $U(x \mid \theta) = x^\top P(\theta) x$, where $P(\theta) \in \mathbb{R}^{n_x \times n_x}$ is the positive definite solution of an algebraic Riccati equation

$$A(\theta)^\top P(\theta) + P(\theta)A(\theta) - P(\theta)B(\theta)Q_u^{-1}B(\theta)^\top P(\theta) + Q_x = O_{n_x},$$

and the corresponding optimal control input can be calculated as $u = -Q_u^{-1}B(\theta)^\top P(\theta)x$.

In the preliminary in Section 2.3, we have shown that the optimal plant parameters θ should be designed differently for different sets of initial states. In this chapter, on the other hand, we minimize the value function $U(x \mid \theta)$ with respect to plant parameters for all possible initial states in $\mathbb{R}^{n_x}$ instead of choosing an arbitrary set of initial states. To achieve optimization, we minimize the determinant of $P(\theta)$ because the value expresses the rate of magnification when the matrix is seen as a linear map.

We now consider the system in Example 2.2. Recall the value function of the optimal control problem

$$U(x \mid \theta) = x^\top \begin{bmatrix} \frac{\sqrt{q_{11}r_{11}}}{2\theta_1} & 0 \\ 0 & \frac{\sqrt{q_{22}r_{22}}}{2\theta_2} \end{bmatrix} x.$$

The determinant of the matrix in the middle is readily calculated as

$$\det P(\theta) = \frac{\sqrt{q_{11}r_{11}q_{22}r_{22}}}{4\theta_1\theta_2}.$$

Minimizing the value with a constraint $\theta_1 + \theta_2 = 1$ yields the optimal plant parameters $\theta_1 = \theta_2 = 0.5$.

Remark 4.1. This method for linear systems can be easily extended to a case where the stochastic properties of the initial states are available. Suppose x is a random vector normally

distributed with the mean vector μ and the covariance matrix Σ. Then, the expectation value of the quadratic form $U(x \mid \theta) = x^\top P(\theta)x$ is given as

$$\mathbb{E}\left[x^\top P(\theta)x\right] = \mathrm{tr}(P(\theta)\Sigma) + \mu^\top P(\theta)\mu, \tag{4.1}$$

In particular, if the mean of x is zero, minimization of the expectation value of U becomes equivalent to minimization of the trace in (4.1) with respect to θ. Similar extensions can be investigated, and further analysis on this topic is a part of our future work.

For the cases with general objective functions, the value function can take various forms, and thus special considerations are needed for each case. Moreover, the HJB equations cannot be solved analytically in general. In fact, even though the objective function takes a quadratic form, the form of the value function might be different in the cases of nonlinear systems (see [70], for example). In the next section, we provide an optimal control law for the second-order system on $SE(3)$ with a specific objective function. One should be carefully noted that the assumption on the existence of analytical solution is usually invalid, and the analytical method can only be applied to the limited cases. However, minimization for all initial states is basically an intractable problem for the numerical method, which will be described in the next chapter. The analytical method here has another advantage that it provides us with the control law in the form of a function of the states, instead of a sequence of numerical values. We can analyze the fundamental properties of the controller such as the closed-loop stability and the region of attraction.

Remark 4.2. Unless the matrix $P(\theta)$ is positive definite for all parameters θ in the region of interest, we cannot ensure the minimization of U by the determinant minimization. For linear cases, it is proved that a unique positive definite solution matrix of the Riccati equation exists if and only if the system is (A, B) controllable [71].

4.2 Optimal Control on $SE(3)$

In this section, we develop an optimal control method for rigid body systems to control fully actuated hexarotors. The rigid body motion is described with a dynamical model on the special Euclidean group $SE(3)$. The dynamics must be constrained on the group, as we have discussed in Section 2.1, and thus we need to consider specific control laws.

4.2.1 Double-geodesic PD Controller on $SE(3)$

Prior to showing an analytic optimal control method, we present a modified version of a double-geodesic PD controller on $SE(3)$ proposed by Bullo and Murray [26]. This provides the basis of analytic optimal control on $SE(3)$ in a similar manner to LQR optimal controller for a second order system, which is technically a PD controller. In this

section, we assume that $\log(R)$ for a rotation matrix R is defined over $SO(3)\backslash\Pi$ where $\Pi = \{R \in SO(3) \mid \operatorname{tr} R = -1\}$, and the norm $\| \log(R)^\vee \|$ takes value within $(-\pi, \pi)$.

Consider a left invariant second order system on $SE(3)$ in equation (2.2). Let the total acceleration be $u_{\text{total}} = u_c - u_{ff}$. u_c is control input, and u_{ff} denotes internal drift to be compensated by feedforward control. This results in a system

$$\begin{aligned} \dot{g} &= g\widehat{V}^b \\ \dot{V}^b &= u_c - u_{ff}. \end{aligned} \tag{4.2}$$

For this system, the following proposition holds.

Proposition 4.1. (adapted from [26, Theorem 11]) Consider a second order system on $SE(3)$ in equation (4.2) and let K_ω, K_v, and K_d be the positive definite gain matrices. Then the control law

$$u_c = u_{ff} - \begin{bmatrix} R^\top K_v p \\ K_\omega \log(R)^\vee \end{bmatrix} - K_d V^b$$

exponentially stabilizes the state $g = (R, p)$ at the origin I_4 from any initial condition $g(0) = (R(0), p(0))$ with $tr(R(0)) \neq -1$ and for all K_ω and $\omega^b(0)$ such that

$$\lambda_{\min}(K_\omega) > \frac{\|\omega^b(0)\|^2}{\pi^2 - \| \log(R(0))^\vee \|^2}, \tag{4.3}$$

where $\lambda_{\min}(K_\omega)$ denotes the minimum eigenvalue of K_ω.

The proof of this proposition is given in [33]. The state error considered in this control law consists of the position error p and the attitude error $\log(R)^\vee$, and the gain matrices K_v and K_ω give weights to the position and attitude errors, respectively.

We would like to consider the acceleration characteristics of the vehicle, and hence the position error should be expressed in the vehicle body frame, that is, $R^\top p$. The following proposition shows the modified version of Proposition 4.1 according to this error in the body frame.

Proposition 4.2. Consider a second order system on $SE(3)$ in equation (4.2) and let K_ω, K_v, and K_d be the positive definite gain matrices. Then the control law

$$u_c = u_{ff} - \begin{bmatrix} K_v R^\top p \\ K_\omega \log(R)^\vee \end{bmatrix} - K_d V^b$$

exponentially stabilizes the state $g = (R, p)$ at the origin I_4 from any initial condition $g(0) = (R(0), p(0))$ with $tr(R(0)) \neq -1$ and for all K_ω and $\omega^b(0)$ such that (4.3).

Proof. The proof can be done in the same steps as in [33]. □

In the rest of this section, an optimal control law is derived based on this type of PD controller.

4.2.2 Double-geodesic Optimal PD Controller

We first define $q(g) := [(R^\top p)^\top \ (\log(R)^\vee)^\top]^\top$ to compute the state error from the origin. Then, we consider the following linear quadratic optimal control problem on $SE(3)$:

$$\min_{u_c(g,V^b)} J \quad \text{subject to} \quad \dot{g} = g\widehat{V}^b,\ \dot{V}^b = u_c - u_{ff}, \tag{4.4}$$

where

$$\begin{aligned} J &= \int_0^\infty L(g, V^b, u_c)dt \qquad (4.5)\\ &= \frac{1}{2}\int_0^\infty \left(\|q(g)\|^2_{M^{-\frac{1}{3}}} + \|V^b\|^2_{M^{\frac{1}{3}}} + \|u_c\|^2_M \right) dt, \\ u_{ff} &= M^{-\frac{1}{3}} \begin{bmatrix} \widehat{\omega}^b & O_3 \\ O_3 & \frac{1}{2}\widehat{\omega}^b + \frac{1-\alpha(\|\psi\|)}{\|\psi\|^2}(\widehat{\psi}\omega^b)^\wedge \end{bmatrix} M^{\frac{1}{3}} V^b. \qquad (4.6) \end{aligned}$$

Here, $\|x\|^2_A$ denotes a quadratic form $x^\top Ax$. u_{ff} is a feedforward input to cancel out the highly nonlinear terms induced by the structure and metric of the space. We use notations $\psi = \log(R)^\vee$ and $\alpha(y) = (y/2)\cot(y/2)$. The state feedback control input must satisfy $g \to I_4$, $V^b \to O_{6\times 1}$, and $u \to O_{6\times 1}$ as $t \to \infty$. M is a 6×6 positive definite diagonal matrix to give weight to each force direction and torque axis. The cube root of the diagonal matrix $M^{\frac{1}{3}}$ consists of the cube roots of each diagonal element, and $M^{-\frac{1}{3}}$ denotes the inverse of $M^{\frac{1}{3}}$.

We solve this problem directly by using the Hamilton-Jacobi-Bellman (HJB) equation. Let η be a scalar energy-like function as follows:

$$\begin{aligned} \eta &= L(g, V^b, u) + (\operatorname{grad} U) \cdot \begin{bmatrix} \dot{q}(g) \\ \dot{V}^b \end{bmatrix} \\ &= \frac{1}{2}\|q(g)\|^2_{M^{-\frac{1}{3}}} + \frac{1}{2}\|V^b\|^2_{M^{\frac{1}{3}}} + \frac{1}{2}\|u_c\|^2_M + \frac{\partial U}{\partial q}\cdot\dot{q}(g) + \frac{\partial U}{\partial V^b}\cdot(u_c - u_{ff}) \end{aligned}$$

The value function U must be a unique solution of the HJB equation, as discussed in Section 2.2 and found in literature such as [61, 72].

$$H(g, V^b, \operatorname{grad} U) := \min_{u_c \in TSE(3)} \eta = 0 \tag{4.7}$$

The terms depending on u are as follows:

$$\frac{1}{2}\|u_c\|_M^2 + \frac{\partial U}{\partial V^b} \cdot u_c. \tag{4.8}$$

By using (A.4), we can derive the following optimal control input $u_c^\star$ that minimizes (4.8).

$$u_c^\star = -M^{-1}\frac{\partial U}{\partial V^b} \tag{4.9}$$

Plugging (4.9) into (4.7), we finally obtain

$$\begin{aligned} H &= \frac{1}{2}\|q(g)\|_{M^{-\frac{1}{3}}}^2 + \frac{1}{2}\|V^b\|_{M^{\frac{1}{3}}}^2 + \frac{\partial U}{\partial q} \cdot \dot{q}(g) - \frac{\partial U}{\partial V^b} \cdot u_{ff} - \frac{1}{2}\left\|\frac{\partial U}{\partial V^b}\right\|_{M^{-1}}^2 \\ &= 0 \end{aligned} \tag{4.10}$$

as the HJB equation, which is the necessary and sufficient conditions of optimality.

We now solve this differential equation with respect to U. The following theorem is the main result of this section, which shows the closed-form solution of the optimal control problem (4.4).

Theorem 4.1. Consider the second order system on $SE(3)$ in equation (4.2) with u_{ff} in (4.6). The optimal control input

$$u_c^\star = -M^{-\frac{2}{3}}q - \sqrt{3}M^{-\frac{1}{3}}V^b \tag{4.11}$$

minimizes the cost function (4.5), and the corresponding value function is

$$U = \frac{\sqrt{3}}{2}\left(\|q\|^2 + \|V^b\|_{M^{\frac{2}{3}}}^2\right) + q^\top M^{\frac{1}{3}}V^b. \tag{4.12}$$

where $M^{\frac{2}{3}}$ and $M^{-\frac{2}{3}}$ denotes $(M^{\frac{1}{3}})^2$ and $((M^{\frac{1}{3}})^2)^{-1}$, respectively.

Proof. The closed-loop system expressed with q and V^b becomes

$$\begin{aligned} \dot{q} &= \begin{bmatrix} \dot{R}^\top p + R^\top \dot{p} \\ \dot{\psi} \end{bmatrix} \\ &= V^b + \begin{bmatrix} -\widehat{\omega}^b R^\top p \\ \frac{1}{2}\widehat{\psi}\omega^b + \frac{1-\alpha(\|\psi\|)}{\|\psi\|^2}\widehat{\psi}^2\omega^b \end{bmatrix} \\ &:= V^b + V_d, \\ \dot{V}^b &= -M^{-\frac{2}{3}}q - \sqrt{3}M^{-\frac{1}{3}}V^b - u_{ff}. \end{aligned}$$

From (4.12), we obtain

$$\frac{\partial U}{\partial q} = \sqrt{3}q^\top + V^{b\top} M^{\frac{1}{3}},$$
$$\frac{\partial U}{\partial V^b} = \sqrt{3}V^{b\top} M^{\frac{2}{3}} + q^\top M^{\frac{1}{3}}.$$

By using formulas (A.1), (A.2), and (A.3), the following equation holds:

$$\begin{aligned} q^\top \dot{q} &= q^\top V^b - \underbrace{(R^\top p)^\top \widehat{\omega}^b R^\top p}_{=0} + \frac{1}{2} \underbrace{\psi^\top \widehat{\psi}}_{=O_{1\times 3}} \omega^b + \frac{1-\alpha(\|\psi\|)}{\|\psi\|^2} \underbrace{\psi^\top \widehat{\psi}^2}_{=O_{1\times 3}} \omega^b \\ &= q^\top V^b. \end{aligned}$$

Plugging these into Hamiltonian (4.10) yields

$$\begin{aligned} H &= \frac{1}{2}\|q\|^2_{M^{-\frac{1}{3}}} + \frac{1}{2}\|V^b\|_{M^{\frac{1}{3}}} + (\sqrt{3}q^\top + V^{b\top} M^{\frac{1}{3}})\dot{q} - (\sqrt{3}V^{b\top} M^{\frac{2}{3}} + q^\top M^{\frac{1}{3}})u_{ff} - \frac{1}{2}\|q\|^2_{M^{-\frac{1}{3}}} \\ &\quad - \sqrt{3}q^\top V^b - \frac{3}{2}\|V^b\|^2_{M^{\frac{1}{3}}} \\ &= V^{b\top} M^{\frac{1}{3}} V_d - q^\top M^{\frac{1}{3}} u_{ff}. \end{aligned}$$

We can easily confirm the following relation

$$\begin{aligned} q^\top M^{\frac{1}{3}} u_{ff} &= u_{ff}^\top M^{\frac{1}{3}} q \\ &= V^{b\top} M^{\frac{1}{3}} \begin{bmatrix} \widehat{\omega}^{b\top} R^\top p \\ -\frac{1}{2}\widehat{\omega}^b \psi - \frac{1-\alpha(\|\psi\|)}{\|\psi\|^2}(\widehat{\psi}\omega^b)^\wedge \psi \end{bmatrix} \\ &= V^{b\top} M^{\frac{1}{3}} V_d, \end{aligned}$$

and thus H becomes 0. Therefore, the function U satisfies HJBE, and the associated optimal control input is given by (4.11). □

The detailed derivation of this optimal control law is described in Appendix A.3.

Remark 4.3. The feedforward term and the objective function are physically meaningful because an analogy to an LQR problem of linear double-integrator system exists. Consider a double-integrator system $\dot{x} = Ax + Bu$, where

$$A = \begin{bmatrix} 0 & 1 \\ 0 & 0 \end{bmatrix}, \ B = \begin{bmatrix} 0 \\ 1 \end{bmatrix},$$

$x = [x_1 \ x_2]^\top \in \mathbb{R}^2$, and $u \in \mathbb{R}$. Then, the optimal control input minimizing the objective

function

$$J = \frac{1}{2}\int_0^\infty \left(x^\top \begin{bmatrix} M^{-\frac{1}{3}} & 0 \\ 0 & M^{\frac{1}{3}} \end{bmatrix} x + Mu^2 \right) dt$$

is given by $u^\star = -\frac{1}{M}B^\top Px$, where $P \in \mathbb{R}^{2\times 2}$ is the positive definite solution of an algebraic Riccati equation

$$A^\top P + PA - PBM^{-1}B^\top P + \begin{bmatrix} M^{-\frac{1}{3}} & 0 \\ 0 & M^{\frac{1}{3}} \end{bmatrix} = O_2.$$

Note that we reuse the notation M on purpose, and $M \in \mathbb{R}$ only for this remark. By solving this quadratic equation, we finally obtain

$$P = \begin{bmatrix} \sqrt{3} & M^{\frac{1}{3}} \\ M^{\frac{1}{3}} & \sqrt{3}M^{\frac{2}{3}} \end{bmatrix},\ u^\star = -M^{-\frac{2}{3}}x_1 - \sqrt{3}M^{-\frac{1}{3}}x_2.$$

These solutions correspond to (4.11) and (4.12).

In general, however, the solution P cannot be expressed in a closed form, and we often resort to numerical methods based on eigenvalue decomposition [73]. In this work, the weight matrices are determined so as to find the closed-form solution, which is required to minimize the value function, of the optimal control problem. There may be possibilities to extend the analytic solution method to more general quadratic objective functions by using this analogy. This is part of the future work.

4.2.3 Stability Analysis

Although the optimal controller resembles the double geodesic PD controller on $SE(3)$ in Proposition 4.2, the resulting closed-loop system is different due to the existence of u_{ff}. We show exponential stability of the closed-loop system in the following theorem.

Theorem 4.2. Consider the dynamical system (4.2). The optimal control input (4.11) exponentially stabilizes the state (g, V^b) at $(I_4, O_{6\times 1})$ from any initial state as long as the trajectory does not pass through $\operatorname{tr} R = -1$.

Proof. We first show the positive definiteness of the value function U, which is the Lyapunov function candidate. Since M is diagonal and

$$U = \frac{1}{2}\begin{bmatrix} q \\ V^b \end{bmatrix}^\top \underbrace{\begin{bmatrix} \sqrt{3}I_6 & M^{\frac{1}{3}} \\ M^{\frac{1}{3}} & \sqrt{3}M^{\frac{2}{3}} \end{bmatrix}}_{P(M)} \begin{bmatrix} q \\ V^b \end{bmatrix} \tag{4.13}$$

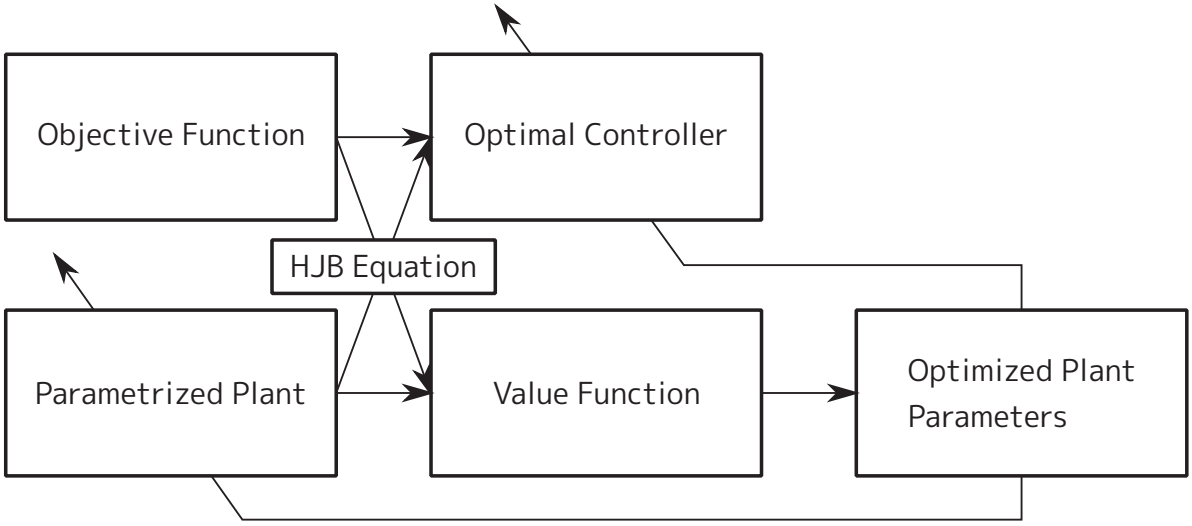

Fig. 4.1: Schematic of analytic joint optimization

holds, the determinant of the block matrix becomes

$$\det\left(\sqrt{3}I_6\sqrt{3}M^{\frac{2}{3}} - M^{\frac{1}{3}}M^{\frac{1}{3}}\right) = \det(2M^{\frac{2}{3}}) > 0$$

since $\det M > 0$. Therefore, U is positive definite. It is trivial to see from (4.7) that $\dot{U} = \frac{\partial U}{\partial q}\dot{q} + \frac{\partial U}{\partial V^b}\dot{V}^b$ is negative definite function since $L(g, V^b, u)$ is positive definite. Moreover, $\dot{U}$ is upper bounded with a quadratic function of q and V^b. Therefore, the value function U is a Lyapunov function, and by using [74, Theorem 3.6] we can show that the origin $q = V^b = O_{6\times 1}$ is exponentially stable. The stability is ensured from any initial state as long as the trajectory does not pass through $\operatorname{tr} R = -1$. □

The conditions on the initial state are not provided as concretely as those in Propositions 4.1 and 4.2. This is also a part of our future work.

These control laws are based on the geometrically natural representation of the rigid body pose and twist. In particular, the control input direction of the rotational part lies along the geodesic of $SO(3)$, which prevents the unnecessary rotation during the convergence. Other control laws based on the Euler angles or Roll-Pitch-Yaw angles cannot ensure this property.

4.3 Joint Optimization for Nongravity Case

4.3.1 Optimization

Many control schemes for fully actuated mechanical systems consider the decoupled wrench or acceleration as the control input, and the actuator input is calculated via inversion. It means that they simply cancel the relation between actuator inputs and system outputs. If the Jacobian matrix is nearly singular, the actuator input will be unexpectedly large due to

the matrix inversion. For example, we can consider the following cost for an optimal control to avoid this issue.

$$\left|\left|\Gamma^{-1}\begin{bmatrix}\dot{v}\\ \dot{\omega}\end{bmatrix}\right|\right|^2 = \begin{bmatrix}\dot{v}\\ \dot{\omega}\end{bmatrix}^\top \Gamma^{-\top}\Gamma^{-1}\begin{bmatrix}\dot{v}\\ \dot{\omega}\end{bmatrix}$$

Note that the inverse matrix Γ^{-1} maps the vehicle acceleration to the rotors thrust force vector. Here, $\Gamma^{-\top}\Gamma^{-1}$ can be interpreted as a weight matrix with the analogy to "$u^\top Ru$" of the well known LQR scheme. With this approach, we can design the behavior of the vehicle by modifying the structure to change Γ.

As we have in Corollary 3.3, $\Gamma\Gamma^\top$ is diagonal for PCTR structure. We now let $M = \mu(\Gamma\Gamma^\top)^{-1}$ so that $u^\top Mu$ evaluates the quadratic cost of the rotors thrust force vector $\tilde{f} \approx \Gamma^{-1}u$. μ can be chosen to adjust the ratio between the state and control input. The optimal control input and the corresponding value function for the fully actuated hexarotor are analytically derived as follows.

$$\begin{aligned} u_c^\star &= -\mu^{-\frac{2}{3}}(\Gamma\Gamma^\top)^{\frac{2}{3}}q - \sqrt{3}\mu^{-\frac{1}{3}}(\Gamma\Gamma^\top)^{\frac{1}{3}}V^b \\ U &= \frac{\sqrt{3}}{2}\left(\|q\|^2 + \|V^b\|_{\mu^{\frac{2}{3}}(\Gamma\Gamma^\top)^{-\frac{2}{3}}}\right) + \mu^{\frac{1}{3}}q^\top(\Gamma\Gamma^\top)^{-\frac{1}{3}}V^b \end{aligned} \tag{4.14}$$

As a recapitulation, we write the steps for the present joint optimization scheme (Fig. 4.1):

1. Parameterize the plant with parameters
2. Formulate an optimal control problem
3. Derive an analytic value function of the optimal control by solving the HJB equation
4. Interpret the value function as a function of plant parameters
5. Perform minimization of the value function with respect to plant parameters

Note that the scheme in this chapter requires the analytical solution of the optimal control problem, which is difficult to obtain in general. In fact, the analytical optimal controller on $SE(3)$ discussed in the last section cannot explicitly consider the force of gravity acting on the vehicle due to this limitation. To mitigate this issue, we will develop a numerical method in Chapter 5.

4.3.2 Optimal Design Example

By exploiting the quadratic form shown in (4.13), we can consider minimization of the value function for all initial states in the configuration space by minimizing the determinant of $P(M)$. According to the discussions in Section 4.1, this can be achieved by maximizing the determinant of $\Gamma\Gamma^\top$, which coincide with maximization of the DMM $w_d = \sqrt{\det(\Gamma\Gamma^\top)}$.

Thus, it is shown that the design optimization maximizing DMM is meaningful in the sense of the optimal control law discussed in the last section.

However, with only maximizing DMM, it is not possible to identify whether the vehicle can maintain its altitude while hovering. Obviously, the structure that can barely hover with the maximum thrust force is inappropriate because it cannot move in the upper direction. Such structure should be excluded from the candidate of optimal structure. Therefore, we introduce a constraint on rotor thrust force to consider the hovering capability. The nonlinear constraint we use is written as follows:

$$\frac{mG}{3\cos\beta\cos\gamma} \leq f_{\max},$$

where $f_{\max}$ is the maximum thrust force of each rotor. This condition means that the vehicle can accelerate at least G in the upper direction.

For given parameters in Table 3.2, the DMM of the hexarotor with SCTR and PCTR structures with respect to the rotor tilt angles β and γ is illustrated in Fig. 4.2. The optimum shown as a black cross mark in the figure is at $(\beta,\ \gamma) = (0,\ 0.8148)$, and the maximum value is $w_d = 1.43 \times 10^6$. The resulting matrix regarding the dynamic manipulability $(\Gamma\Gamma^\top)^{\frac{1}{2}}$ becomes

$$(\Gamma\Gamma^\top)^{\frac{1}{2}} = \begin{bmatrix} 2.0 & 0 & 0 & 0 & 0 & 0 \\ 0 & 2.0 & 0 & 0 & 0 & 0 \\ 0 & 0 & 2.667 & 0 & 0 & 0 \\ 0 & 0 & 0 & 60.35 & 0 & 0 \\ 0 & 0 & 0 & 0 & 60.35 & 0 \\ 0 & 0 & 0 & 0 & 0 & 36.77 \end{bmatrix}.$$

Note that the optimum is on the boundary of the inequality (4.3.2). The corresponding structure is visualized in Fig. 4.3. This result show that large tilt angles are necessary to achieve larger total DMM.

We can also consider minimization of the average of the value function U for a set of initial states. Note that, in this case, U becomes constant for all initial pose q and the Jacobian Γ if the initial twist is $V^b = O_{6\times1}$, and any structure can be the optimal structure.

4.3.3 Simulation

The optimal control input can be calculated by substituting the values of structural variables into (4.11). We compare results of the following simulations:

- Simulation 4A:
  Optimal control for the optimal structure ($w_d = 1.43 \times 10^6$) with large tilt angles $\beta = 0,\ \gamma = 0.8148$

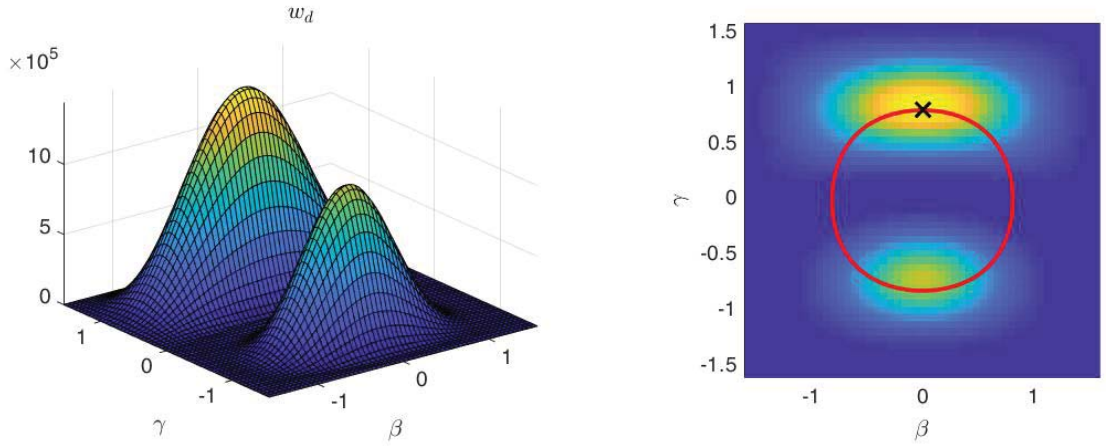

(a) SCTR

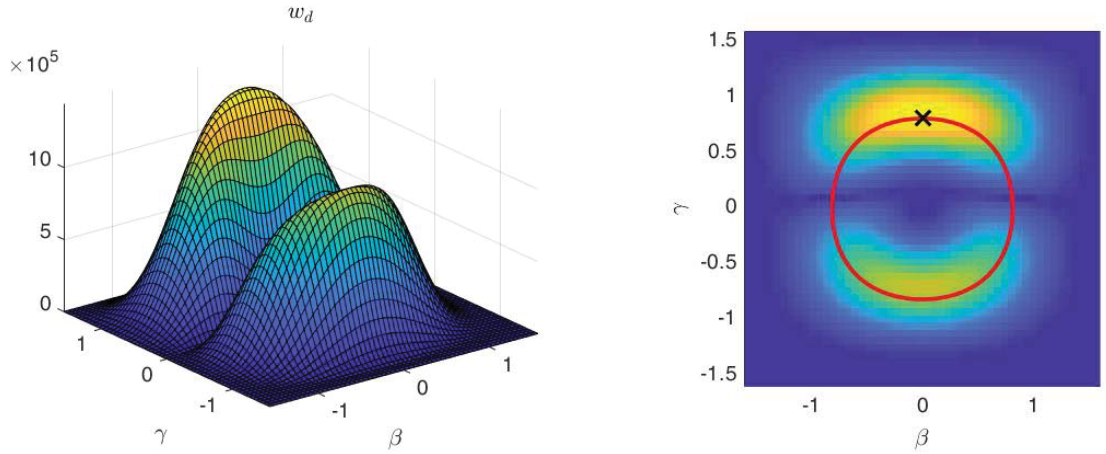

(b) PCTR

Fig. 4.2: DMM of the hexarotor. The surface plots on the left show the DMM w_d with respect to rotor tilt angles β and γ. The heat maps on the right are the top view of the surface plots.

- Simulation 4B:
  Optimal control for a suboptimal structure ($w_d = 1.14 \times 10^5$) with small tilt angles $\beta = \pi/10,\ \gamma = 0$

The initial state is $g_{oc}(0) = (p_{oc}(0), R_{oc}(0))$, $V_c^b(0) = [2\ 0\ 0.5\ 0\ 0\ 0]^\top$, where $p_{oc}(0) = [1\ 2\ -0.5]^\top$ and $R_{oc}(0) = R_x(\pi/8)R_y(\pi/10)$. We set $\alpha = 0.1$ for both simulations to quickly regulate the states.

The time responses of the state $q(g_{oc}), V_c^b$ and thrust force input $\tilde{f} \approx \Gamma^{-1}u$ are shown in Figs. 4.4, 4.5. The $\mathcal{L}_2$ norm of the thrust force input $\Gamma^{-1}u$ is also displayed in the figures. Note that $q(g_{oc}) \to O_{6\times 1}$ implies $g_{oc} \to ([0\ 0\ 0]^\top,\ I_3)$. For both cases, the state and input converge to the origin. In Simulation 4A, the value of the cost function is $\min_u J = 5.75$, whereas $\min_u J = 6.99$ in Simulation 4B. Since the structure in Simulation 4B has lower ability of horizontal acceleration, the convergence becomes slower than Simulation 4A. As

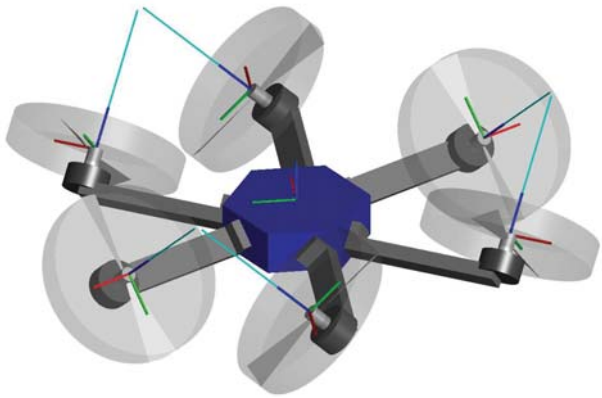

Fig. 4.3: Optimal hexarotor structure. The rotor tilt angles are $\beta = 0,\ \gamma = 0.8148$, and the DMM of this structure is $w_d = 1.43 \times 10^6$, which is 99% of the maximum value of w_d in the example.

we can confirm from the $\mathcal{L}_2$-norm of the control input, it also needs more control effort. These results mean that the minimum cost of the control can be further minimized by the structural design optimization, and they verify the effectiveness of the proposed joint optimization scheme.

Remark 4.4. The thrust force input $\Gamma^{-1}u$ is calculated without the gravity compensation input. Because of this, the result is only valid for the hexarotor system under zero gravity. In reality, however, the hexarotor system is subject to the force of gravity, and the energy consumption of rotors is mostly due to the gravity compensation. To overcome this problem, we will develop a numerical joint optimization method to explicitly consider the cost of the compensation in the next chapter.

4.4 Chapter Summary

In Section 4.2, we have newly proposed an analytic optimal control method for rigid body dynamics, which has closed-form solution of the value function and the corresponding optimal control input. Relying on the Hamilton-Jacobi-Bellman equation, Theorem 4.1 shows that the control law minimizes the objective function. Furthermore, Theorem 4.2 ensures exponential stability of the origin from almost every initial state.

Based on the optimal controller, we have developed an analytical method for joint optimization of structure and control in Section 4.3. The analytic value function of optimal control is reinterpreted as a function of plant parameters. An application to a fully actuated hexarotor is then studied, and it is shown that the minimization of the value function corresponds to maximization of dynamic manipulability of the hexarotor. At the end of the section, the optimality of the controller and plant parameters has been tested with simulations.

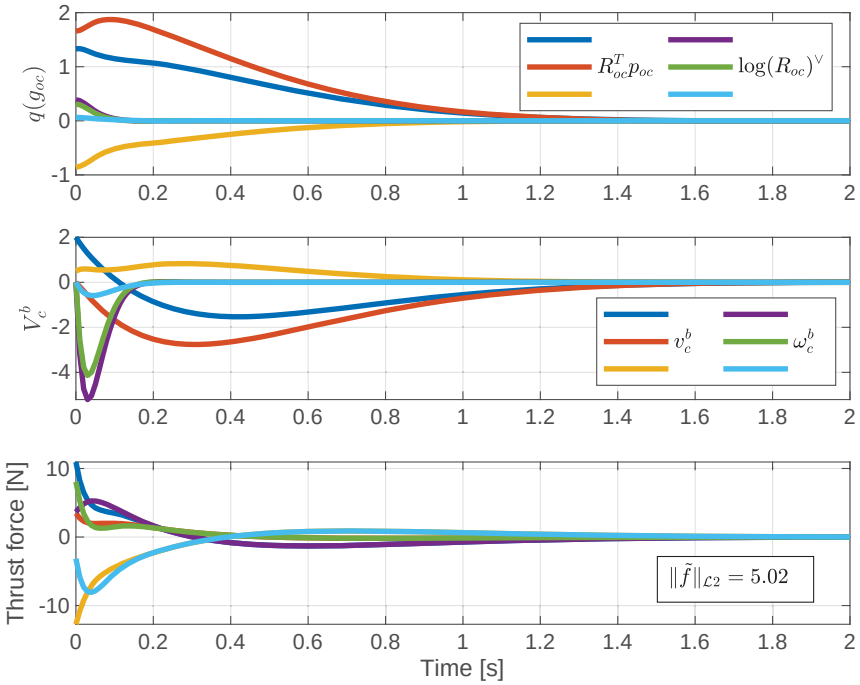

Fig. 4.4: Simulation 4A: The pose $q(g_{oc})$, twist V_c^b and the thrust input $\tilde{f} \approx \Gamma^{-1} u_c^\star$ are shown.

Issues to be tackled include generalization of the analytic optimal controller and a further analysis on the initial state conditions in Theorem 4.2.

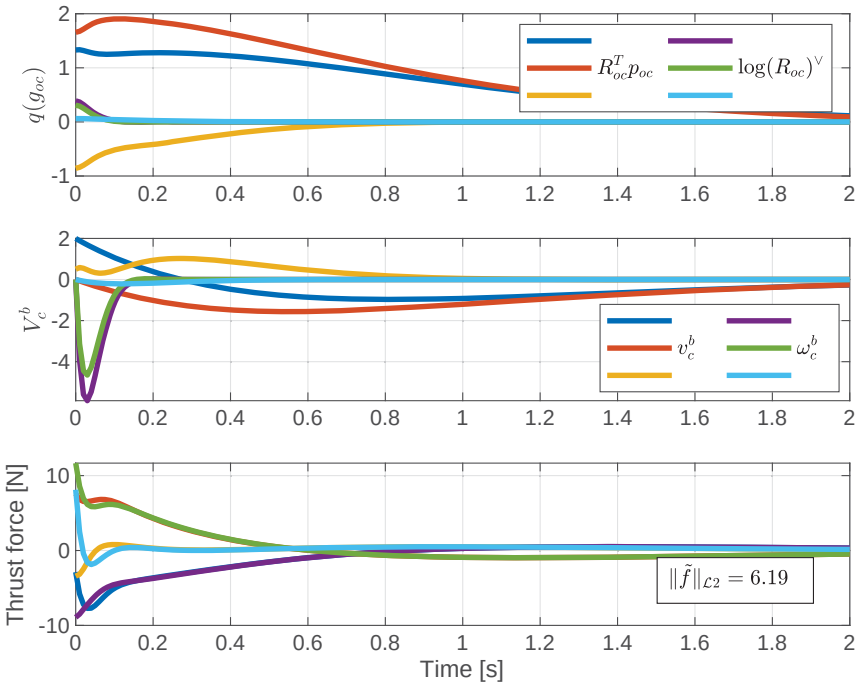

Fig. 4.5: Simulation 4B: The thrust force is larger than that of Simulation 4A (Fig. 4.4). The rate of convergence is also slower due to the poor ability of horizontal acceleration.

Chapter 5

Numerical Optimization Method

In this chapter, we develop a numerical optimal control method for the rigid body dynamics and extend the idea of joint optimization to more general cases. Because the explicit form of the value function for an optimal control problem is not readily available, the analytical method proposed in Chapter 4 cannot be used. Nevertheless, we can numerically evaluate the value function as the result of numerical optimal control described in Section 2.2. We draw attention to the fact and consider a numerical joint optimization method that utilizes numerical optimal controller as a source of the value function to minimize. For both control and parameter optimization, fast computation is the key to solve the problem efficiently. Motivated by them, we will develop a real-time nonlinear optimal control method specialized in the rigid body system in the 3-dimensional space in this chapter. Then, the method is used to perform NMPC and the joint optimization of the structure and control.

The rest of this chapter is organized as follows. Section 5.1 develops a numerical optimal control method for rigid body systems based on an NMPC scheme. In particular, our focus of the method is on the real-time execution of the NMPC, which is usually computationally intensive, on an embedded computer. The reduction of computational effort is done by the novel usage of a geometric integrator using the Cayley map on $SE(3)$ along with the recursive discretization technique, which allows us to reduce the number of the decision variables of the optimization problem. In Section 5.2, we apply the control method to a fully actuated hexarotor system and carry out an experiment with on-board computation of the NMPC. The result shows that the present method is real-time feasible and verifies the effectiveness of the proposed method. Then, the fast optimal controller is reused for the joint optimization of the structure and control for fully actuated hexarotor aerial vehicles in Section 5.3. By using the numerical methods, we can optimize the vehicle structure for different control tasks specified with objective functions of control and sets of initial states. Finally, Section 5.4 summarizes this chapter. This chapter is written based on the author's previous work [75,76] [1].

[1] ©2020 IEEE. Partly reprinted, with permission, from [76].

5.1 Numerical Optimal Control Method for a Rigid Body

In this section, we propose a fast and precise model predictive controller for rigid body dynamics by using exact discretization via a geometric integrator. The controller is used for both real-time control and the optimal parameter design of a fully actuated hexarotor.

5.1.1 Exact Discretization using Geometric Integrators

Forward-Euler Approximation

To motivate the need of exact discretization methods, we consider a simple forward-Euler approximation of the system dynamics in the vector space.

$$g_{k+1} = g_k + g_k \widehat{V}_k T, \tag{5.1}$$

It is well known that this method provides a good approximation if the sampling period T and the twist V are sufficiently small. However, the equation (5.1) does not guarantee that the resulting matrix g_{k+1} is constrained in the group.

Exponential Map

One simple approach to resolve this problem is to use the exponential map for $SE(3)$ to integrate the piecewise constant twist of a rigid body [58]. Let $V_k = \begin{bmatrix} v_k^\top & \omega_k^\top \end{bmatrix}^\top$ be the twist at the kth step, and assume that it is constant for the sampling period $T > 0$. The pose g_{k+1} is then computed as

$$g_{k+1} = g_k \exp(\widehat{V}_k T), \tag{5.2}$$

In other words, the exponential map generates the pose difference $g_{k+1} g_k^{-1}$ in $SE(3)$ from the constant velocity v_k and angular velocity ω_k. This geometric integration method is referred to as the Lie-Euler method [34]. (5.2) provides exact discrete time evolution of the rigid body kinematics and also mathematically constrains g on $SE(3)$, as shown in Fig. 5.1. We now vectorize the kinematic equation (5.2) as the vector form is more convenient in both the theory and computation than the matrix representation. Before showing our main results, we try to use the exponential map and its inverse, logarithm map [59], to obtain a vector form of (5.2). Applying (2.9) to (5.2) yields

$$\psi_{k+1} = \log(\exp(\widehat{\psi}_k) \exp(\widehat{V}_k T))^\vee. \tag{5.3}$$

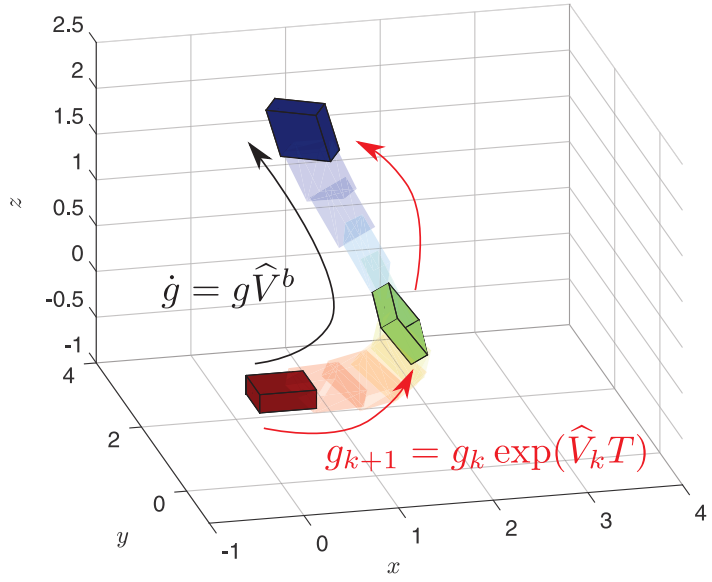

Fig. 5.1: Exact discretization of rigid body kinematics. The geometric integrator preserves the group structure during the process of integration.

The new state ψ_{k+1} can be expressed as a function of ψ_k and V_k by using the Baker-Campbell-Hausdorff formula [77]

$$\widehat{\psi}_{k+1} = \widehat{\psi}_k + \widehat{V}_k T + \frac{1}{2}\left[\widehat{\psi}_k, \widehat{V}_k T\right] + \frac{1}{12}\left[\widehat{\psi}_k, \left[\widehat{\psi}_k, \widehat{V}_k T\right]\right] + \frac{1}{12}\left[\widehat{V}_k T, \left[\widehat{\psi}_k, \widehat{V}_k T\right]\right] + \cdots,$$

where $[\cdot,\cdot]$ denotes the Lie bracket, $[\widehat{a}, \widehat{b}] = \widehat{a}\widehat{b} - \widehat{b}\widehat{a}$. It is reported that one can obtain the closed-form equation by using dual vectors [78]. However, calculation of log needs a transcendental function $\cos^{-1}$ to extract the angle from the rotation matrix, as mentioned in [39] and [58, Appendix A]. Moreover, $\log(g)$ is not unique for an element of $SE(3)$ because the rotation angle may take multiple values $\theta + 2\pi n$, where θ is a representative value of $\log(g)$ and $n \in \mathbb{Z}$, for a rotation matrix. These characteristics of the logarithm map make it difficult to obtain a simple discretized model to be used in the prediction part of NMPC.

Cayley Map

To overcome the problems of the logarithm map, we now discretize the rigid body motion based on the Cayley parameter for $SE(3)$. With an analogy to (5.3), the kinematic equation of a rigid body can be written in Cayley parametrization as follows:

$$\begin{aligned}\psi^{©}_{k+1} &= \begin{bmatrix}\xi^{©}_{k+1} \\ \eta^{©}_{k+1}\end{bmatrix} \\ &= \mathrm{Cay}^{-1}(\mathrm{Cay}(\widehat{\psi}^{©}_k)\,\mathrm{Cay}(\widehat{V}^{©}_k T))^{\vee}. \end{aligned} \tag{5.4}$$

This is a discrete-time kinematic equation with Cayley parametrization, and it represents the same time evolution as (5.2). The

We show the detailed closed-form equation of (5.4), which is not in the literature. The direct calculation yields

$$\xi^{©}_{k+1} = \frac{I_3 - \omega^{©}_k T \eta^{©\top}_k - \widehat{\omega}^{©}_k T}{1 - \eta^{©\top}_k \omega^{©}_k T} \xi^{©}_k + \frac{I_3 - \eta^{©}_k \omega^{©\top}_k T + \widehat{\eta}^{©}_k}{1 - \eta^{©\top}_k \omega^{©}_k T} v^{©}_k T, \tag{5.5}$$

$$\eta^{©}_{k+1} = \frac{I_3}{1 - \eta^{©\top}_k \omega^{©}_k T} \eta^{©}_k + \frac{I_3 + \widehat{\eta}^{©}_k}{1 - \eta^{©\top}_k \omega^{©}_k T} \omega^{©}_k T. \tag{5.6}$$

The corresponding trajectory of the pose on the Lie group $SE(3)$ can be calculated from $\psi^{©}$ through the Cayley map (2.10), and thus the trajectory can be constrained on the group. Moreover, the equations only require matrix and vector computation. Therefore, it is easy to compute closed forms of mathematical utilities such as the Jacobians of $\psi^{©}_{k+1}$ and the gradient of a function with respect to trajectories defined by this formula. These are useful for solving an optimal control problem efficiently.

Remark 5.1. The angular velocity parameter $\omega^{©}_k$ must satisfy $\eta^{©\top}_k \omega^{©}_k T \neq 1$; otherwise, the orientation at the $(k+1)$th step becomes unable to calculate.

Remark 5.2. For the case $\eta^{©\top}_k \omega^{©}_k T > 1$ where the orientation leaps across a singular orientation, the denominator $1 - \eta^{©\top}_k \omega^{©}_k T$ becomes negative. This might seem as if the rotation direction is inverted, but it does not affect the result of integration since rotation by the angles θ and $\theta - 2\pi$ gives the same orientation.

We now compare the discretization methods based on the Euler method and the Cayley map to emphasize the need of geometric integrators. We integrate the kinematic equation on $SE(3)$ in (2.1) with the constant body twist $V^b = [0.5\ 0\ 0\ 0.2\ 0.1\ 0.3]^\top$. The sampling period for both methods here is chosen as $T = 0.3$ s. Fig. 5.2 shows the time evolution of the pose starting from the origin shown with dark red color. The box is transformed according to the resulting matrix g interpreted as an affine transformation matrix in 3 dimensions. The figure depicts that the scale of the rigid body is no longer preserved, and the body is also skewed due to the broken orthogonality in the rotation matrix part of g. As a matter of fact, the Euler method renders the determinant of the rotation matrix up to 3.5 after 100 integration steps in this example, failing to constrain the kinematics on $SE(3)$.

5.1.2 Problem Settings

We now state the problem settings of the optimal control problem for a rigid body dynamical system expressed with the Newton-Euler equation in 3-dimensional space (2.4). It is shown in Section 2.1 that the system is written as a second-order system on $SE(3)$ in (2.5). Thus we can discretize the equation of motion by using the geometric integrator based on the Cayley

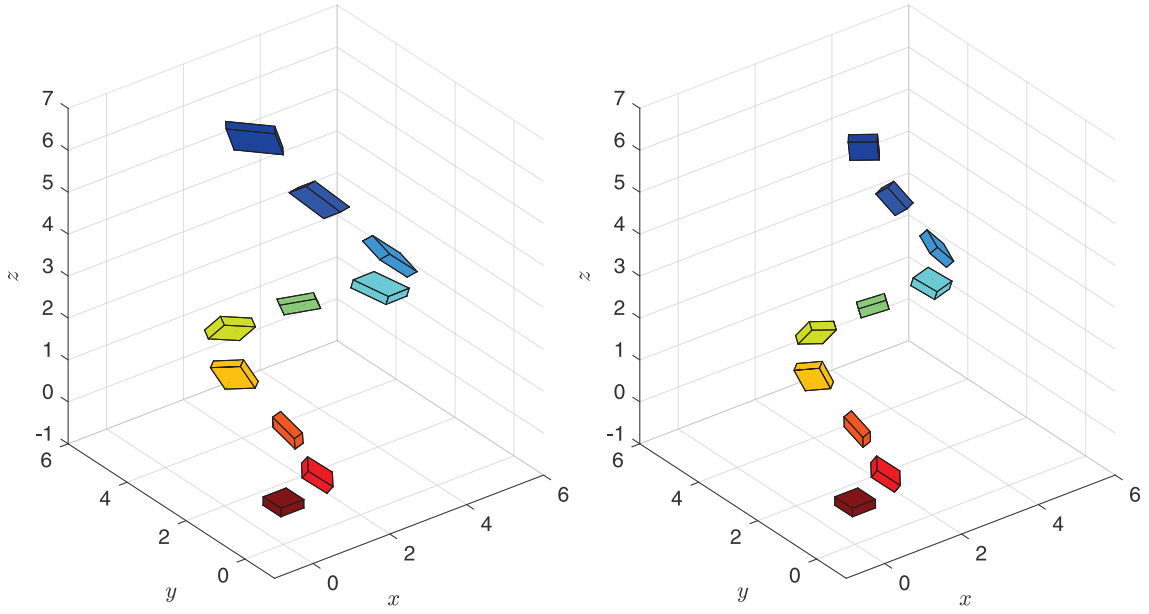

(a) Euler Approximation. (b) Cayley Map.

Fig. 5.2: Comparison of discretization methods. The pose of the rigid body is at the origin $g = I_4$ at $t = 0$ s (shown with dark red color), and it is driven by the constant twist. The body is drawn every 10 steps with the sampling period $T = 0.3$ for each step.

map for $SE(3)$. For simplicity, we neglect the second- or higher order terms regarding the continuous change in the body twist during discretization. This means that both the twist (linear and angular velocity) and the wrench (force and torque) do not change during a sampling period. Under this assumption, the whole discrete-time dynamical model of the second-order system on $SE(3)$ is expressed as follows:

$$\psi^{\copyright}_{k+1} = \mathrm{Cay}^{-1}(\mathrm{Cay}(\widehat{\psi}^{\copyright}_{k})\,\mathrm{Cay}(\widehat{V}^{\copyright}_{k}T))^{\vee}, \tag{5.7}$$

$$V^{\copyright}_{k+1} = V^{\copyright}_{k} + (u^{\copyright}_{k} + u^{\copyright}_{\mathrm{grav},k})T. \tag{5.8}$$

Here, the gravitational acceleration term $u^{\copyright}_{\mathrm{grav},k}$ is calculated by applying the transformation (5.11) to u_{grav}.

Remark 5.3. The assumption on constant twist and acceleration may cause numerical errors in the trajectory prediction. Because we use a model predictive control scheme later in this section, the error can be treated as a disturbance affecting the twist, and it can be attenuated by the feedback nature of model predictive control. If the higher order terms are needed, we can directly compute them by considering the Taylor series expansion of the Cayley map in the same manner as in [79]. We can also improve the accuracy of the trajectory by using shorter sampling periods in the transient state. These improvements are part of our future work.

We now consider nonlinear model predictive control of the discrete-time rigid body dy-

namics (5.7) and (5.8). For simplicity, we use the same value T for the control period and the sampling time of the prediction horizon. We solve the following nonlinear programming problem at each control period:

$$J = \frac{1}{2}\sum_{k=1}^{N}\left(\|\psi_k^{\copyright}\|_{Q_p}^2 + \|V_k^{\copyright}\|_{Q_v}^2 + \|u_{k-1}^{\copyright} - u_{\mathrm{term}}^{\copyright}\|_{Q_u}^2\right) \tag{5.9}$$

$$\min_{\substack{\psi_1^{\copyright},\ldots,\psi_N^{\copyright},\\ V_1^{\copyright},\ldots,V_N^{\copyright},\\ u_0^{\copyright},\ldots,u_{N-1}^{\copyright}}} J \quad \text{subject to (5.7), (5.8), } u_{\mathrm{lb}}^{\copyright} \le u_k^{\copyright} \le u_{\mathrm{ub}}^{\copyright}.$$

The objective function J is a quadratic form of the Cayley parameters, and box constraints on the acceleration input are considered. Here, we use the notation $\|x\|_A^2 = x^\top Ax$. Q_p, Q_v, and Q_u are positive semidefinite 6×6 weight matrices for the pose, twist, and acceleration parameters, respectively. We assume that the initial states $\psi_0^{\copyright}$ and $V_0^{\copyright}$ are given, and terminal conditions are not specified. The control objective is to achieve $g_k \to I_4$ by $\psi_k^{\copyright} \to O_{6\times1}, V_k^{\copyright} \to O_{6\times1}$. In the objective function, $u_{\mathrm{term}}^{\copyright} = [0\ 0\ \frac{G}{2}\ 0\ 0\ 0]^\top$ denotes the equilibrium input at the desired terminal state $g = I_4, V = O_{6\times1}$. We consider the input cost $\frac{1}{2}\|u_{k-1}^{\copyright} - u_{\mathrm{term}}^{\copyright}\|_{Q_u}^2$ to ensure that the incremental cost becomes zero at the desired terminal state and to induce $u^{\copyright} \to u_{\mathrm{term}}^{\copyright}$.

The state and input time series are now stacked into vectors as follows:

$$\boldsymbol{\psi}^{\copyright} = \begin{bmatrix}\psi_1^{\copyright}\\ \psi_2^{\copyright}\\ \vdots\\ \psi_N^{\copyright}\end{bmatrix},\ \boldsymbol{V}^{\copyright} = \begin{bmatrix}V_1^{\copyright}\\ V_2^{\copyright}\\ \vdots\\ V_N^{\copyright}\end{bmatrix},\ \boldsymbol{u}^{\copyright} = \begin{bmatrix}u_0^{\copyright} - u_{\mathrm{term}}^{\copyright}\\ u_1^{\copyright} - u_{\mathrm{term}}^{\copyright}\\ \vdots\\ u_{N-1}^{\copyright} - u_{\mathrm{term}}^{\copyright}\end{bmatrix}.$$

We next rewrite the objective function (5.9) using these time series vectors as

$$J = \frac{1}{2}\left(\boldsymbol{\psi}^{\copyright\top}\boldsymbol{Q}_p\boldsymbol{\psi}^{\copyright} + \boldsymbol{V}^{\copyright\top}\boldsymbol{Q}_v\boldsymbol{V}^{\copyright} + \boldsymbol{u}^{\copyright\top}\boldsymbol{Q}_u\boldsymbol{u}^{\copyright}\right). \tag{5.10}$$

Here, $\boldsymbol{Q}_p, \boldsymbol{Q}_v$, and $\boldsymbol{Q}_u$ are defined as

$$\boldsymbol{Q}_p = I_N \otimes Q_p,\ \boldsymbol{Q}_v = I_N \otimes Q_v,\ \boldsymbol{Q}_u = I_N \otimes Q_u,$$

where $\otimes$ denotes the Kronecker product such that

$$I_N \otimes Q_p = \mathrm{blkdiag}(\underbrace{Q_p, \ldots, Q_p}_{N}).$$

In addition to the relation between $\log(g)$ and $\mathrm{Cay}^{-1}(g)$ in (2.11) and (2.12), we also need to derive the relation between the actual linear/angular acceleration $u = [u_{\mathrm{tr}}^\top\ u_{\mathrm{rot}}^\top]^\top \in \mathbb{R}^6$

and the corresponding acceleration in Cayley parametrization $u^{\copyright} = [u_{\mathrm{tr}}^{\copyright\top}\ u_{\mathrm{rot}}^{\copyright\top}]^\top \in \mathbb{R}^6$. We obtain the following equations by taking the time derivatives of (2.11) and (2.12):

$$\begin{aligned} u_{\mathrm{tr}}^{\copyright} &= \frac{dv^{\copyright}}{dt} \\ &= \begin{cases} \mathcal{A}(\omega)u_{\mathrm{tr}} + \mathcal{B}(v,\omega)u_{\mathrm{rot}} & \text{for } \|\omega\| \neq 0 \\ \frac{1}{2}u_{\mathrm{tr}} & \text{for } \|\omega\| = 0 \end{cases}, \end{aligned} \tag{5.11}$$

$$\begin{aligned} u_{\mathrm{rot}}^{\copyright} &= \frac{d\omega^{\copyright}}{dt} \\ &= \begin{cases} \left(\frac{\omega\omega^\top}{(1+\cos\|\omega\|)\|\omega\|^2} - \frac{\tan\frac{\|\omega\|}{2}}{\|\omega\|}\frac{\widehat{\omega}^2}{\|\omega\|^2} \right) u_{\mathrm{rot}} & \text{for } \|\omega\| \neq 0 \\ \frac{1}{2}u_{\mathrm{rot}} & \text{for } \|\omega\| = 0 \end{cases}. \end{aligned} \tag{5.12}$$

Here, $\mathcal{A}$ is defined in (2.11), and $\mathcal{B}(v,\omega)$ is a nonlinear matrix derived by collecting the terms of u_{rot} from $\frac{d}{dt}(\mathcal{A}(\omega)v)$. Similarly, we can also obtain the inverse transformation, which is used to compute the actual acceleration input u from the virtual control input $u^{\copyright}$. These transformations are not mentioned in the related research that uses the Cayley map such as [37], but they are required in applications.

Remark 5.4. It is easy to see from (2.12) that $\|\eta^{\copyright}\| \to \infty$ as $\|\eta\| \to \pi$. This means that the Cayley parameter cannot express the rotation by π rad in any axes, i.e., $\mathrm{tr}(R) = -1$, and the parametrization becomes singular at such orientations. Related to this problem, numerical errors become large if the attitude of the rigid body is near the singular orientations due to the tangent function in (2.11) and (2.12). A dual quaternion [80] can be used to express the pose globally without such state-dependent errors, although it is not unique for a pose and raises the same issue as the logarithm map.

Remark 5.5. The Cayley parameter $\psi^{\copyright} \in \mathfrak{se}(3)$ can be uniquely determined for a pose $g \in SE(3)$ except for the singular orientations described in Remark 5.4. Stabilization of the origin $\psi^{\copyright} = O_{6\times 1}$ results in the pose regulation $g \to I_4$.

5.1.3 Reduction of Computational Effort

We employ the recursive discretization technique [38, Chapter 10] to eliminate the states $\psi_k^{\copyright}$ and $V_k^{\copyright}$ from (5.9). Recursively applying (5.7) and (5.8), we obtain

$$V_{k+1}^{\copyright}(V_0^{\copyright}, \boldsymbol{u}^{\copyright}) = V_0^{\copyright} + \sum_{j=0}^{k}(u_j^{\copyright} + u_{\mathrm{grav},j}^{\copyright}(\psi_j^{\copyright}, V_j^{\copyright}))T, \tag{5.13}$$

$$\psi_{k+1}^{\copyright}(\psi_0^{\copyright}, V_0^{\copyright}, \boldsymbol{u}^{\copyright}) = f(\dots f(f(\psi_0^{\copyright}, V_0^{\copyright}), V_1^{\copyright})\dots, V_k^{\copyright}), \tag{5.14}$$

where $f(\psi_k^{\copyright}, V_k^{\copyright}) = \psi_{k+1}$. The objective function (5.9) is then rewritten as a function that takes only the initial conditions $\psi_0^{\copyright}, V_0^{\copyright}$ and the input sequence $\boldsymbol{u}^{\copyright}$. The resulting nonlinear

optimization problem becomes as follows:

$$\min_{\boldsymbol{u}^{\copyright}} J(\psi_0^{\copyright}, V_0^{\copyright}, \boldsymbol{u}^{\copyright}) \quad \text{subject to } u_{\mathrm{lb}}^{\copyright} \leq u_k^{\copyright} \leq u_{\mathrm{ub}}^{\copyright}. \tag{5.15}$$

In this case, the number of decision variables of the NMPC problem is reduced from $18N$ to $6N$. Moreover, the dynamics constraints (5.7) and (5.8) are no longer needed since they are satisfied during the calculation of (5.13) and (5.14).

Instead of using finite-difference approximations, we compute the closed-form gradient of the objective function (5.9) with respect to the input time series $\boldsymbol{u}^{\copyright}$ by utilizing (5.13) and (5.14). This is because centered finite-difference approximations evaluate the objective function $12N$ times, that is, twice the number of decision variables. They usually take more time than the analytic computation due to the repetitive recursive integration of (5.7) with (5.14).

From (5.10), the analytic gradient is readily available as follows:

$$\frac{\partial J}{\partial \boldsymbol{u}^{\copyright}} = \boldsymbol{\psi}^{\copyright\top} \boldsymbol{Q}_p \frac{\partial \boldsymbol{\psi}^{\copyright}}{\partial \boldsymbol{u}^{\copyright}} + \boldsymbol{V}^{\copyright\top} \boldsymbol{Q}_v \frac{\partial \boldsymbol{V}^{\copyright}}{\partial \boldsymbol{u}^{\copyright}} + \boldsymbol{u}^{\copyright\top} \boldsymbol{Q}_u.$$

The Jacobian matrices $\frac{\partial \boldsymbol{\psi}^{\copyright}}{\partial \boldsymbol{V}^{\copyright}}$ and $\frac{\partial \boldsymbol{V}^{\copyright}}{\partial \boldsymbol{u}^{\copyright}}$ are calculated as block lower triangular matrices in the following equations:

$$\frac{\partial \boldsymbol{\psi}^{\copyright}}{\partial \boldsymbol{u}^{\copyright}} = \begin{bmatrix} O_6 & \cdots & \cdots & O_6 \\ \frac{\partial \psi_2^{\copyright}}{\partial u_0^{\copyright}} & O_6 & \cdots & O_6 \\ \vdots & \ddots & \ddots & \vdots \\ \frac{\partial \psi_N^{\copyright}}{\partial u_0^{\copyright}} & \cdots & \frac{\partial \psi_N^{\copyright}}{\partial u_{N-2}^{\copyright}} & O_6 \end{bmatrix}, \quad \frac{\partial \boldsymbol{V}^{\copyright}}{\partial \boldsymbol{u}^{\copyright}} = \begin{bmatrix} \frac{\partial V_1^{\copyright}}{\partial u_0^{\copyright}} & \cdots & \cdots & O_6 \\ \frac{\partial V_2^{\copyright}}{\partial u_0^{\copyright}} & \frac{\partial V_2^{\copyright}}{\partial u_1^{\copyright}} & \cdots & O_6 \\ \vdots & \ddots & \ddots & \vdots \\ \frac{\partial V_N^{\copyright}}{\partial u_0^{\copyright}} & \cdots & \frac{\partial V_N^{\copyright}}{\partial u_{N-2}^{\copyright}} & \frac{\partial V_N^{\copyright}}{\partial u_{N-1}^{\copyright}} \end{bmatrix}. \tag{5.16}$$

From (5.13) and (5.14), we have recurrence formulas of the block components as follows:

$$\begin{aligned} \frac{\partial u_{\mathrm{grav},n+1}^{\copyright}}{\partial u_m^{\copyright}} &= \left.\frac{\partial u_{\mathrm{grav}}^{\copyright}}{\partial \psi^{\copyright}}\right|_{\substack{\psi^{\copyright}=\psi_n^{\copyright} \\ V^{\copyright}=V_n^{\copyright}}} \cdot \frac{\partial \psi_n^{\copyright}}{\partial u_m^{\copyright}} + \left.\frac{\partial u_{\mathrm{grav}}^{\copyright}}{\partial V^{\copyright}}\right|_{\substack{\psi^{\copyright}=\psi_n^{\copyright} \\ V^{\copyright}=V_n^{\copyright}}} \cdot \frac{\partial V_n^{\copyright}}{\partial u_m^{\copyright}}, \\ \frac{\partial V_{n+1}^{\copyright}}{\partial u_m^{\copyright}} &= \frac{\partial V_n^{\copyright}}{\partial u_m^{\copyright}} + \frac{\partial u_{\mathrm{grav},n}^{\copyright}}{\partial u_m^{\copyright}} T, \\ \frac{\partial \psi_{n+1}^{\copyright}}{\partial u_m^{\copyright}} &= \left.\frac{\partial f}{\partial \psi^{\copyright}}\right|_{\substack{\psi^{\copyright}=\psi_n^{\copyright} \\ V^{\copyright}=V_n^{\copyright}}} \cdot \frac{\partial \psi_n^{\copyright}}{\partial u_m^{\copyright}} + \left.\frac{\partial f}{\partial V^{\copyright}}\right|_{\substack{\psi^{\copyright}=\psi_n^{\copyright} \\ V^{\copyright}=V_n^{\copyright}}} \cdot \frac{\partial V_n^{\copyright}}{\partial u_m^{\copyright}} \end{aligned}$$

for $n \geq m+2,\ m \geq 0$, and

$$\frac{\partial u_{\mathrm{grav},m+1}^{\copyright}}{\partial u_m^{\copyright}} = O_6,\ \frac{\partial V_{m+1}^{\copyright}}{\partial u_m^{\copyright}} = T I_6,\ \frac{\partial \psi_{m+1}^{\copyright}}{\partial u_m^{\copyright}} = O_6.$$

Here, the states $\psi_k^{\copyright}$ and $V_k^{\copyright}$ are precalculated by (5.13) and (5.14) and plugged into Jacobian matrices $\frac{\partial u_{\mathrm{grav}}^{\copyright}}{\partial \psi^{\copyright}}$, $\frac{\partial u_{\mathrm{grav}}^{\copyright}}{\partial V^{\copyright}}$, $\frac{\partial f}{\partial \psi^{\copyright}}$, and $\frac{\partial f}{\partial V^{\copyright}}$. Therefore, the gradient can be computed with only

the initial state $\psi_0^{\copyright}$, $V_0^{\copyright}$ and the control input sequence $\boldsymbol{u}^{\copyright}$. Moreover, with the sparse structure of the Jacobian matrices $\frac{\partial \boldsymbol{\psi}^{\copyright}}{\partial \boldsymbol{u}^{\copyright}}$ and $\frac{\partial \boldsymbol{V}^{\copyright}}{\partial \boldsymbol{u}^{\copyright}}$, the total computation time for matrix multiplication can be reduced to less than half of that for dense matrix multiplication.

5.1.4 Acceleration Input Constraint

The input constraints should be imposed on the physical acceleration u, but the control input is its corresponding Cayley parameter $u^{\copyright}$, which has no physical meaning. As we have shown in (5.11) and (5.12), the transformation between u and $u^{\copyright}$ requires the twist $V = [v^\top \ \omega^\top]^\top$, which is a part of the state. This means that the simple box constraints on the actual acceleration u turn into complicated nonlinear constraints on $u^{\copyright}$, and this is undesirable.

Although we cannot strictly constrain the actual acceleration, we can approximate the input constraints when the angular velocity ω is sufficiently small. Here, we use the relation between u and $u^{\copyright}$ in (5.11) and (5.12) for $\|\omega\| = 0$. The approximated lower and upper bounds u_{lb} and u_{ub} of the actual acceleration become as follows:

$$\tilde{u}_{\mathrm{lb}} \approx 2u_{\mathrm{lb}}^{\copyright}, \ \tilde{u}_{\mathrm{ub}} \approx 2u_{\mathrm{ub}}^{\copyright}.$$

As we will see in the next section, this approximation is computationally efficient and behaves well in both the transient and steady states.

5.1.5 On-board Verification of Feasibility

We have implemented the NMPC algorithm on a Raspberry Pi 3 Model B+ single-board computer (ARMv8 CPU, 1.4 GHz) in C++. We have used the low-storage Broyden-Fletcher-Goldfarb-Shanno algorithm [81] with box constraints (L-BFGS-B algorithm [82]) implemented in NLopt [83] library to solve the problem (5.15). The dynamics of a rigid body are simulated by using the discretized model (5.5), (5.6), and (5.8), and the nonlinear programming problem (5.15) is solved at each step. We exploit the sparsity of Jacobian matrices in (5.16) to compute the analytic gradient efficiently.

Remark 5.6. We use standard nonlinear optimization algorithms to minimize J, instead of using LGVI-based methods. This is because both the initial and terminal states are constrained in LGVI-based methods, and imposing some input constraints may result in ill-conditioned finite-time control problems. In contrast, the terminal state is not constrained in our approach, and thus such an issue merely arises as long as the constraints are well-conditioned.

In this section, we show numerical examples for the following two applications:

- Simulation 5A: Spacecraft with input saturation.
  The dynamical model (5.8) and the objective function (5.9) are calculated without gravity, i.e., $G = 0\,\mathrm{m\,s^{-2}}$. The acceleration input is constrained by using the approximation shown in the last section.

- Simulation 5B: A fully actuated aerial vehicle under gravity.
  The dynamical model and the objective function are calculated with gravitational acceleration constant $G = 9.8\,\mathrm{m\,s^{-2}}$. The control input is not constrained.

Both systems can be modeled as second-order fully actuated systems on $SE(3)$ [25], [84]. For both cases, the weight matrices in the objective function are $Q_p = Q_v = Q_u = I_6$. The initial state is given by $\psi_0^{\copyright} = \mathrm{Cay}^{-1}(g_0)$ and $V_0^{\copyright} = O_{6\times 1}$, where $g_0 \in SE(3)$ is the initial pose. The control objective is to achieve $g_k \to I_4$ by $\psi_k^{\copyright} \to O_{6\times 1}, V_k^{\copyright} \to O_{6\times 1}$.

Simulation 5A

In Simulation 5A, we consider optimal pose regulation of spacecraft with input saturation. This can also be identified with a dynamical system of a fully actuated aerial vehicle with gravity compensation applied. The input is constrained by $u_{\mathrm{ub}}^{\copyright} = [0.3\ 0.3\ 0.3\ 0.2\ 0.2\ 0.2]^\top$ and $u_{\mathrm{lb}}^{\copyright} = -u_{\mathrm{ub}}^{\copyright}$, that is, $u_{\mathrm{ub}} \approx [0.6\ 0.6\ 0.6\ 0.4\ 0.4\ 0.4]^\top$. The gravitational acceleration constant is set to $G = 0$, and accordingly, $u_{\mathrm{term}}^{\copyright} = u_{\mathrm{grav},k}^{\copyright} = O_{6\times 1}$. The initial pose is defined as $g_0 = (R_0, p_0)$, where $R_0 = R_x(\frac{\pi}{4})R_z(\frac{\pi}{6})$ and $p_0 = [10\ 0\ 0]^\top$. The duration of the prediction horizon is 1 s, and it is divided into $N = 20$ periods (i.e., $T = 0.05$ s).

Figure 5.3 shows the optimal trajectory of the pose g and the corresponding Cayley parameter $\psi^{\copyright}$. The colors of boxes in Fig. 5.3 (c) indicate the time on the trajectories. The initial and terminal poses are displayed with dark red and dark blue boxes, respectively. Fig. 5.4(a) shows the acceleration parameter input $u^{\copyright}$. The pose $g = \mathrm{Cay}(\widehat{\psi}^{\copyright})$ converges to the identity under input constraints. The physical acceleration u calculated from the acceleration parameter $u^{\copyright}$ is shown in Fig. 5.4. Although the approximated lower bound $\tilde{u}_{\mathrm{lb}}$ is violated at some steps, as illustrated in Fig. 5.4(b), the error is sufficiently small and is not critical in practice. The computation time is far less than the sampling period, as it is shown in Fig. 5.6, and the present method successfully achieves real-time computation of NMPC on board.

As seen in Fig. 5.3 (b), the proposed controller exhibits desirable rotational behavior that is similar to that of the analytical control law discussed in Section 4.2. This is because the Cayley map for $SE(3)$ also provides with a geometrically intrinsic representation of the rigid body pose.

Simulation 5B

In Simulation 5B, we consider control of a fully actuated aerial vehicle without prior gravity compensation. The gravitational acceleration constant is set to $G = 9.8\,\mathrm{m\,s^{-2}}$. From (2.5)

and (5.11), the equilibrium input at the desired terminal state is then given as $u^{\copyright}_{\mathrm{term}} = [0\ 0\ 4.9\ 0\ 0\ 0]^{\top}$. When the control input is only applied to counter the force of gravity, the input cost equals to $\frac{1}{2}\|u^{\copyright}_{\mathrm{grav},k} + u^{\copyright}_{\mathrm{term}}\|^2_{Q_u}$. This value is positive except for $\psi^{\copyright}_k = O_6, V_k = O_6$, and we can say that the cost for gravity compensation is also included in the objective function (5.9). The initial pose is $R_0 = I_3,\ p_0 = [10\ 6\ 0]^{\top}$, and the acceleration input is not constrained in this simulation. The prediction horizon duration is 2 s, and it is divided into $N = 20$ periods (i.e., $T = 0.1$ s). We have selected the prediction horizon longer than that of Simulation 5A to improve stability.

Figure 5.5 shows the optimal pose trajectory and control input. The rigid body decelerates by tilting the body in the opposite direction of travel. This notable behavior is the result of considering the gravity compensation cost. The sum of squared norm of $u^{\copyright}_0 - u^{\copyright}_{\mathrm{term}}$ is 46.03 when we utilize the body tilt with the acceleration input in the $+z$-direction of the body frame. If we force the controller to use only the horizontal acceleration by constraining the rotational input $u^{\copyright}_{\mathrm{rot}}$ to be always zero, the value becomes 74.81. This result shows that the most efficient maneuver under gravity is not the parallel motion. It is also shown that our present NMPC method and the objective function can deal with the external force, which is difficult to consider in analytic solution methods.

The measured computation time for the optimization is shown in Fig. 5.7. The optimization takes longer time than that of Simulation 5A because computation regarding $u^{\copyright}_{\mathrm{grav}}$ is additionally required in this case. It is still applicable to real-time applications since the computation time remains less than half of the control period.

Discussion on Computation Time

Note that long computation time is observed in the first period of the simulations A and B. We can avoid this by setting a proper initial guess of the input sequence. In practical applications, this is a minor issue because we can compute the initial input for the initial state before turning the actuators on.

We have experimented for several other cases with different sets of N and T to see how they affect the computation time. The results are summarized in Table 5.1. We can see that the longer prediction horizon leads to longer computation, and the required time is not only affected by the number of prediction steps N, but also by the sampling period T.

As seen in Table 5.1, we cannot afford N larger than 20 in this case, since the computation time significantly increases with increasing N. To achieve real-time computation for a long prediction horizon together with a fine time resolution, we may need to combine our proposed techniques with more efficient NMPC algorithms such as the continuation/GMRES method [85] or the differential dynamic programming approach or differential dynamic programming approach [86]. We can also consider non-uniform sampling time, as discussed in [87] and [88], to use a fine sampling time resolution in the transient state while sampling coarsely in the steady state, which can achieve a long horizon with a small N. Since our discretization

Table 5.1: Summary of the computation time on a Raspberry Pi embedded computer.

Settings	Minimum [ms]	Median [ms]	Maximum [ms]
Simulation 5A $N = 10$ $T = 100$ ms	0.28	0.29	2.05
Simulation 5A $N = 20$ $T = 50$ ms	0.84	1.04	11.81
Simulation 5A $N = 20$ $T = 100$ ms	0.16	1.52	14.77
Simulation 5A $N = 40$ $T = 100$ ms	1.11	8.87	130.63
Simulation 5B $N = 20$ $T = 50$ ms	7.22	9.35	16.98
Simulation 5B $N = 20$ $T = 100$ ms	4.79	13.12	49.89
Simulation 5B $N = 40$ $T = 100$ ms	17.24	101.77	460.26

method based on the Cayley map is geometrically exact, it is easy to apply it to the non-uniform-sampling NMPC without being concerned about the variable numerical precision due to approximations. Such additional techniques would be used to further improve the computational performance, and they are part of our future work.

In this section, we have presented a fast NMPC method for rigid body dynamics that can run on an embedded computer in real time. We have combined the following methods to speed up the nonlinear optimization:

- Geometrically exact discretization based on the Cayley map: it allows us to pick coarse sampling intervals and reduces the required number of prediction steps.
- The recursive discretization technique [38]: it reduces the number of decision variables by eliminating the sequence of states from the objective function and constraints.
- The analytic gradient of the objective function: with the Cayley-map-based discretization, the gradient is easily calculated, and the sparsity of intermediate matrices can be exploited to speed up matrix multiplication.

Future work includes NMPC with a singularity-free representation of the rigid body pose, the stability analysis, nonlinear state constraints with reduced computational effort,

and nonuniform sampling intervals to consider a long prediction horizon with a small number of prediction steps.

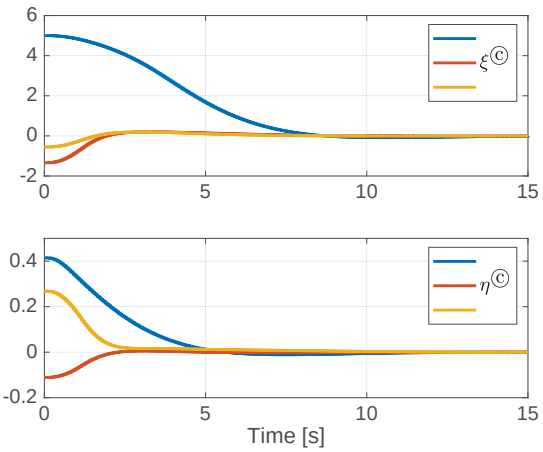

(a) Pose trajectory.

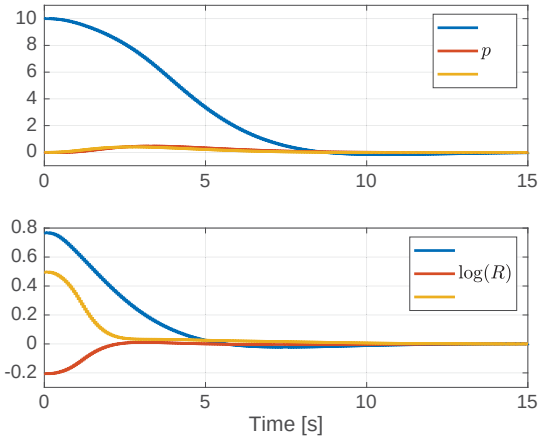

(b) Pose trajectory.

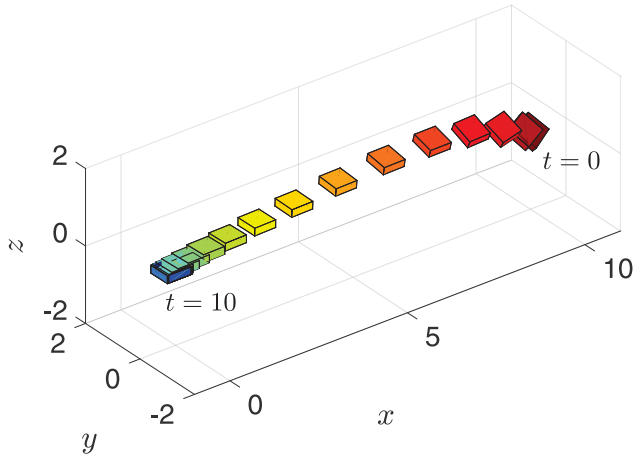

(c) Visualization of the trajectory.

Fig. 5.3: Time evolution of pose (Simulation 5A): The convergence of the Cayley parameter $\psi^{©} = \left[\xi^{©\top}\ \eta^{©\top}\right]^{\top}$ implies the convergence of the pose $g = \mathrm{Cay}(\widehat{\psi^{©}})$ to the identity.

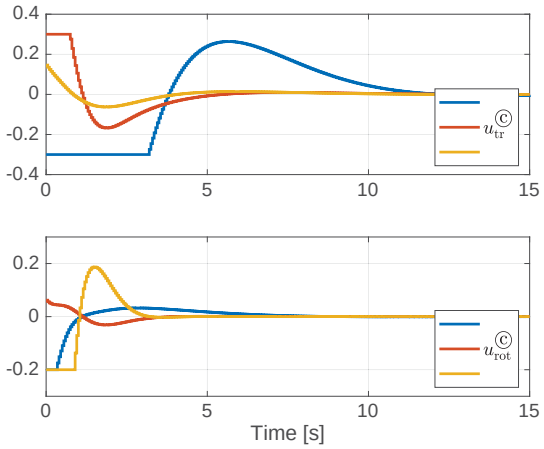

(a) Control input.

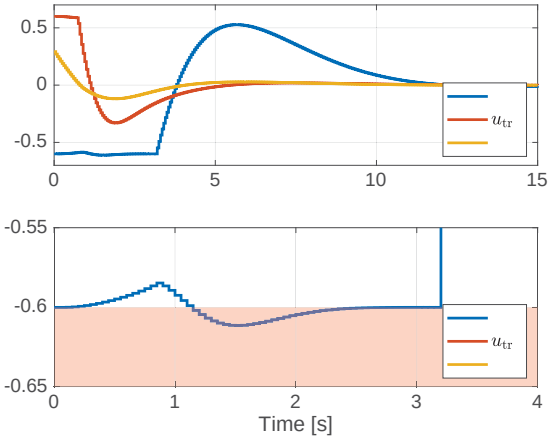

(b) Linear acceleration u_{tr}.

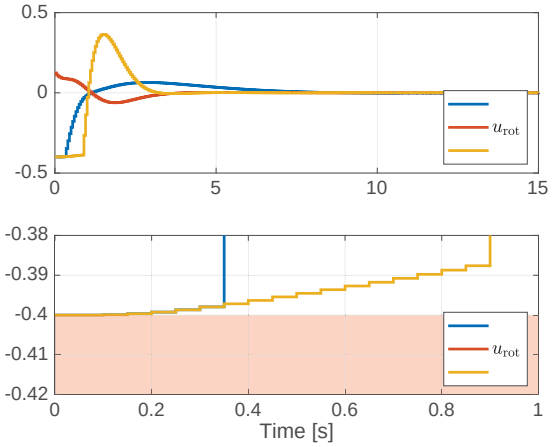

(c) Angular acceleration u_{rot}.

Fig. 5.4: Time evolution of input (Simulation 5A): Note that the control input $u^{©} = \left[u_{\mathrm{tr}}^{©\top}\ u_{\mathrm{rot}}^{©\top}\right]^{\top}$ in (a) does not represent the physical acceleration. In (b), the linear acceleration u_{tr} violates the approximated constraint shown in the red region. However, the approximation error is sufficiently small and not critical in practice.

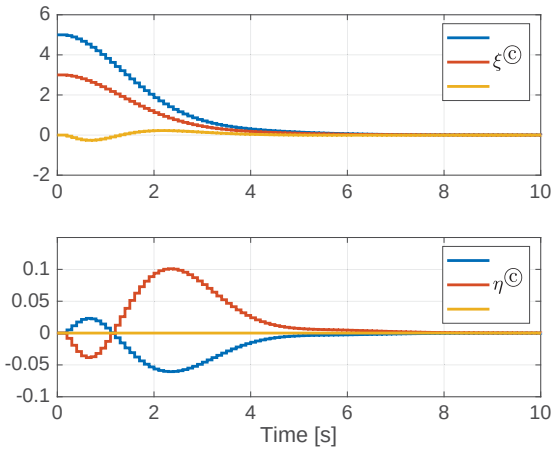

(a) Pose trajectory.

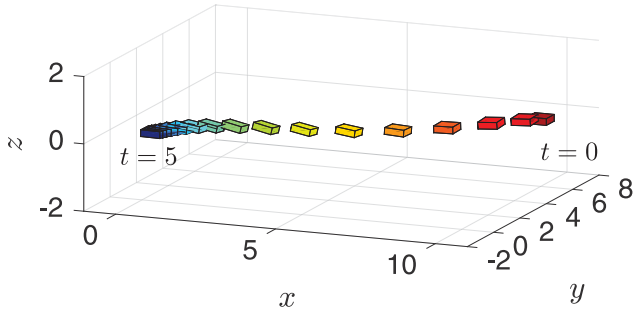

(b) Visualization of the trajectory.

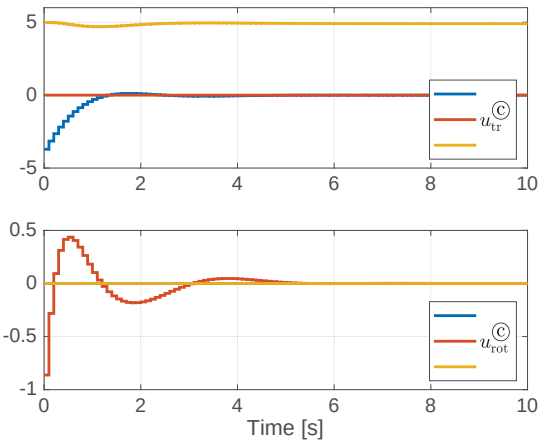

(c) Control input.

Fig. 5.5: Time evolution of pose and input (Simulation 5B): The rigid body decelerates by tilting the body in the opposite direction of travel. This behavior is achieved by considering the cost for gravity compensation.

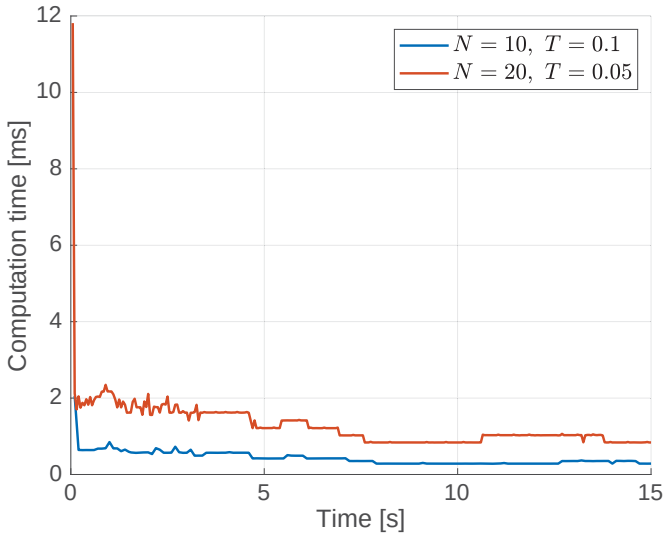

Fig. 5.6: Computation time for each sampling period (Simulation 5A). The proposed NMPC method is feasible in real time on a Raspberry Pi single-board computer.

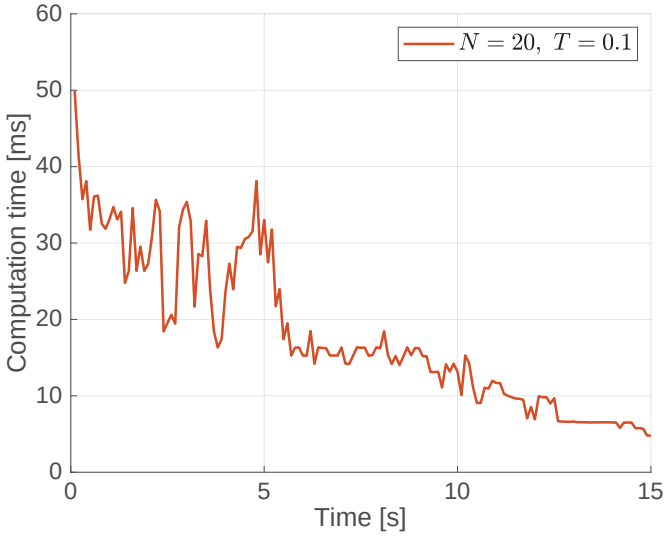

Fig. 5.7: Computation time for each sampling period (Simulation 5B). The computational time is longer than that of Simulation 5A, but it is still tractable in real time.

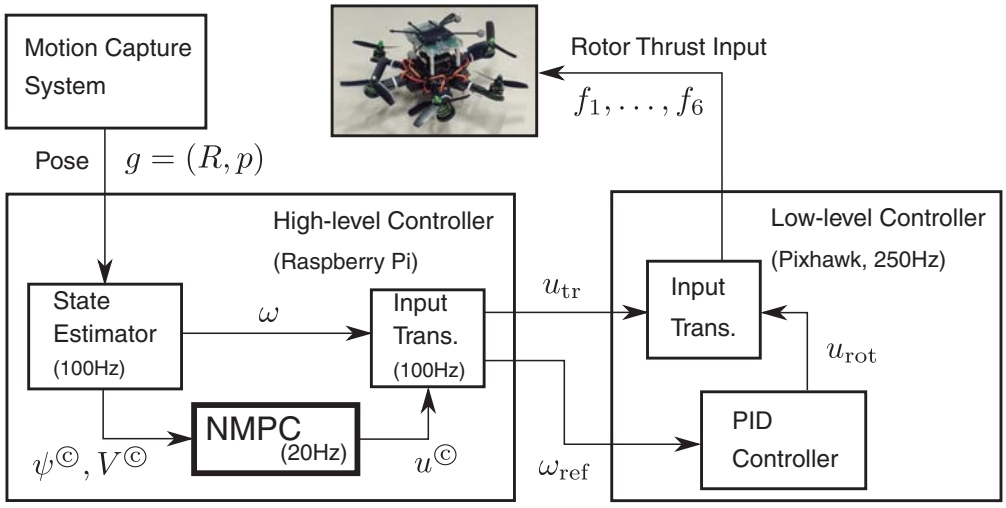

Fig. 5.8: Block diagram of the NMPC experiment. The present NMPC method is implemented on the high-level controller.

5.2 Experimental Verification

In this section, we apply the proposed NMPC method to a fully actuated hexarotor system and conduct a pose control experiment. The objective of the experiment is to show the real-time feasibility of the proposed method and with some input constraints and the force of gravity considered.

5.2.1 Experimental Setup

We use an experimental vehicle and its testbed described in Section 3.4. The NMPC algorithm presented in Section 5.1 is implemented on the Raspberry Pi 3B+ embedded computer used in the feasibility validation in Section 5.1.

Fig. 5.8 shows the block diagram of the experimental system. The high-level controller running on the Raspberry Pi estimates the current state at 100 Hz and calculates the NMPC input at 20 Hz ($T = 0.05$ s). The computed NMPC input $u^{\copyright}$ is converted to the real acceleration vector u by using the inverse maps of (5.11) and (5.12). The Pixhawk Mini implements the low-level controller, which controls the linear acceleration $u_{\mathrm{tr}} = [a_{x\mathrm{ref}}\ a_{y\mathrm{ref}}\ a_{z\mathrm{ref}}]^{\top}$ and the angular velocity ω by a feed-forward and PID controller, respectively.

The pose of the vehicle is measured by an OptiTrack motion capture system by observing the reflective markers on the body, and the information is sent to the high-level controller via UDP on the wireless LAN at the rate 100 Hz. As mentioned in Section 3.4, the pose information from the motion capture system to the vehicle has a latency of approximately 0.15 s. Due to this latency and the relatively long control period of NMPC, the attitude dynamics easily become unstable when we use angular acceleration as the control input. It is especially critical if modeling errors of force and torque exist, which can include unmodeled

rotor dynamics or the aerodynamic behavior such as the ground effect. As the verification of the real-time NMPC is the objective of this experiment, we do not directly command the angular acceleration as the input. Instead, we control the angular velocity with the low-level controller. The angular velocity input is calculated by (5.8) with the estimated current state and the NMPC input.

In this experiment, the vehicle is first commanded to stay at the initial pose $(R, p) = (I_3, [0\ 0\ 0.8]^\top)$, and then at $t \approx 15$ s and 25 s, the reference y coordinate is changed to -1 and 1, respectively. The reference position is set by shifting the origin. The origins of the attitude and twist are $R = I_3$ and $V = O_{6\times1}$, respectively. The objective function is the same as that of simulations defined in (5.10). We set the weight matrix for the pose to $Q_p = 5I_6$ in order to penalize the position error, and $Q_v = Q_u = I_6$ for the twist and the control input. According to the simulation results in the last section, the prediction horizon is defined by $N = 20$ and $T = 0.05$ s. The gravitational acceleration constant is set to $G = 9.8\,\mathrm{m\,s^{-2}}$ to explicitly compensate for the force of gravity. We constrain the horizontal linear acceleration $a_{x\mathrm{ref}}$ and $a_{y\mathrm{ref}}$ in an interval $[-1, 1]$ by restricting the corresponding Cayley parameters in $u_{tr}^{\copyright}$ to an interval $[-0.5, 0.5]$.

5.2.2 Result

Figure 5.9 shows the result of this experiment. The pose trajectory and the control input are displayed in Figs. 5.9(a) and 5.9(b), respectively. The pose successfully converges to the step reference in the y coordinate. It shows the similar behavior as Simulation 5B in the last section, which utilizes the body tilt and the thrust force in the upright direction to accelerate horizontally. In Fig. 5.10(a), the time response of the y-acceleration to the reference value is presented. We can confirm that the acceleration input constraint in y axis is activated from $t \approx 15$ to 15.5 and from $t \approx 25$ to 26. The computation time for NMPC shown in Fig. 5.10(b) remains at approximately 0.01 s during the experiment. This time is sufficiently shorter than the control period 0.05 s, and the result verifies that the present NMPC method is real-time feasible also in the experimental setup with a low-cost single-board computer. This result is notable because there are only a few studies that report experiments of the real-time mobile robot control by on-board NMPC computation. By combining the exact discretization method and the recursive discretization technique, we have achieved reduction of the decision variables and the fast analytic computation of the objective function gradient.

Remark 5.7. The experiment shows local stability in presence of disturbances such as unmodeled dynamics of the battery or rotors. Although the stability is not proved yet, the stabilizing constraint technique discussed in [38, Chapter 5] could be applied to our case. The main challenge is that we need to explicitly consider the external force, namely the force of gravity, in the stability analysis.

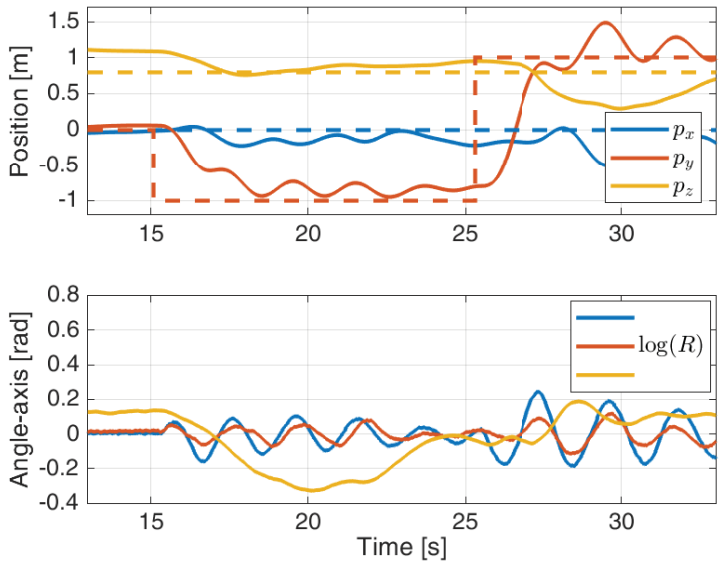

(a) Pose trajectory

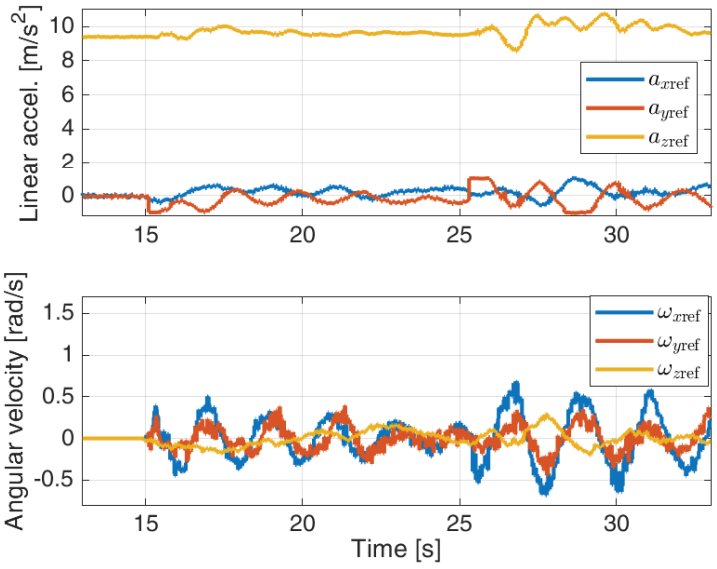

(b) Control input

Fig. 5.9: Result of the experiment with a fully actuated hexarotor. The pose trajectory and the control input are displayed in (a) and (b), respectively.

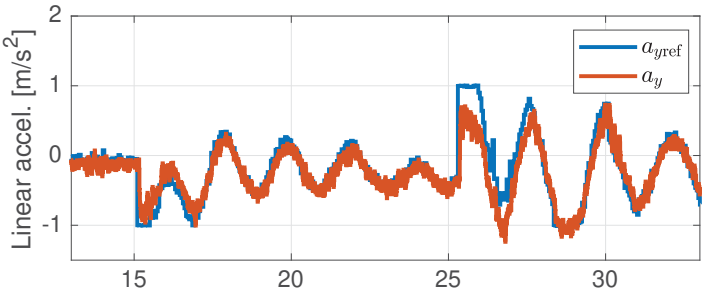

(a) Response of acceleration

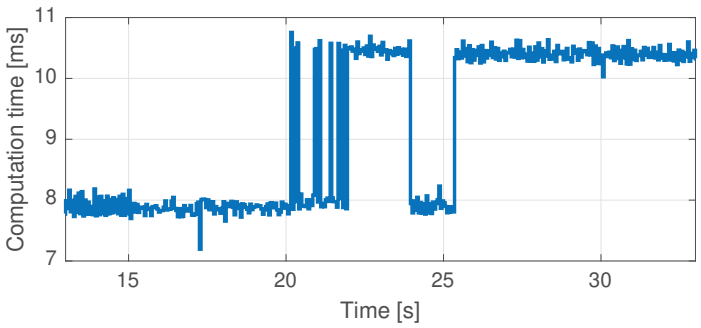

(b) Computation time

Fig. 5.10: Result of the experiment with a fully actuated hexarotor. (a) shows that the vehicle can quickly respond to the acceleration input. The computation time for NMPC shown in (b) confirms that the present NMPC method is also real-time feasible in the experiment.

5.3 Numerical Joint Optimization Method

In this section, we develop a numerical joint optimization method based on the numerical optimal control discussed in the last section. We show that this novel method can deal with more general objective functions and dynamics. With the fast computation of optimal control input, we are also able to reduce the computation time of the plant parameter optimization.

5.3.1 Method

Since the exact form of value function is unknown in this case, we can only evaluate the value function by computing the optimal control input. We consider a discrete set of initial states X_0 and minimize the average value of the cost resulting from the numerical optimal control (5.10) for each initial state in X_0.

Now we consider how to minimize the simulated minimum cost over the domain of plant parameters by using some optimization algorithms. The problem is that computing the gradient of the value function from simulation results can take significant amount of time. Moreover, the smoothness of the value function is not guaranteed, and thus we cannot simply use gradient-based algorithms. Another demand is that we would like to obtain a global minimum if it is possible. From the view of these issues, we employ particle swarm optimization (PSO) [89] algorithm for this problem. PSO is a gradient-free optimization algorithm, which moves multiple candidate solutions called "particles" around the solution space with simple rules. Performing simulations for each particle is basically not the best idea to implement because the computational time may easily explode when the number of particles increases. However, with our fast computation method of optimal control for a rigid body system shown in Section 5.1, it can be solved in short amount of time.

The control input is not constrained in this section.

5.3.2 Result

We carry out optimization of the fully actuated hexarotors with PCTR, SCTR, and generically-tilted-rotor (GTR) structures in this section. The GTR structure is the structure that the rotors are independently tilted. The plant parameters for the GTR structure are tilt angles β and γ for each rotor, and thus there exist 12 parameters.

Now, we consider 3 different use-case scenarios of fully actuated hexarotors. The structural parameters are optimized for the following objective function:

$$J = \frac{1}{2}\sum_{k=1}^{N}\left(\|\psi_k^{\copyright}\|_{I_6}^2 + \|V_k^{\copyright}\|_{I_6}^2 + \|u_{k-1}^{\copyright}\|_{M}^2\right),$$
$$M = \mu(\Gamma\Gamma^\top)^{-1},$$

where the matrix $\Gamma \in \mathbb{R}^{6\times6}$ is defined in (3.6) as the Jacobian matrix from the thrust force input to the vehicle acceleration. The input weight matrix M is chosen to penalize the direction in which large thrusts are required to accelerate. $\mu > 0$ can be set to adjust the cost ratio between the state error and the control input, and set to $\mu = 1$ in the examples in this section. This choice of the input weight matrix is the same as that of the analytical method for hexarotors developed in Section 4.3.

The following task specifications are expressed as sets of initial states:

1. Vertical lift-up
   The initial states are on the z axis at the z coordinates $\{-10, -9, \ldots, 10\}$, and $R = I_3, V = O_{6\times1}$ to consider position control only in the vertical direction. We expect a trivial optimal structure, which is a standard underactuated hexarotor in Fig. 1.1.

2. Short-distance transportation
   The scenario of transportation within small areas such as a factory or a park involves position control in every direction. This control task can be described by 182 points uniformly placed according to the polar coordinates on a sphere with the radius 4 m.

3. Aerial manipulation
   Aerial manipulation applications such as building inspection [4] and assembly in the air [5] should consider the effect of contact with objects. When the vehicle collides with an object, the velocity becomes discontinuous in time. To create a structure that responds quickly to such disturbances, we choose non-zero velocity in horizontal directions as the initial state. This control task is described by 21 points uniformly placed on a circle on xy-velocity plane with the radius 6 m/s.

The set of initial states is approximated with finite elements, and we minimize the average value of the value function with respect to the plant parameters.

We use mechanical constants of the experimental vehicle in Table 3.2. To determine the effect of the prediction horizon duration, we consider two cases: $(N, T) = (10, 1)$ and $(20, 0.2)$. The former aims to obtain moderate input by using the long prediction horizon, while latter expects quicker state convergence.

Vertical Lift-up

The optimal rotor tilt angles are computed as $\beta = 3.263 \times 10^{-7}$ and $\gamma = 1.706 \times 10^{-7}$, which are almost zeros. This means that the optimal structure for the vertical lift-up task is the standard hexarotor structure shown in Fig. 1.1, which corresponds to the intuition.

Short-distance Transportation

The rotor tilt angles of the optimal PCTR structure are computed as $\beta_P = 0.1813$ and $\gamma_P = 0.0560$. For the SCTR structure, we obtain the optimal rotor tilt angles as $\beta_S = -0.0035$ and

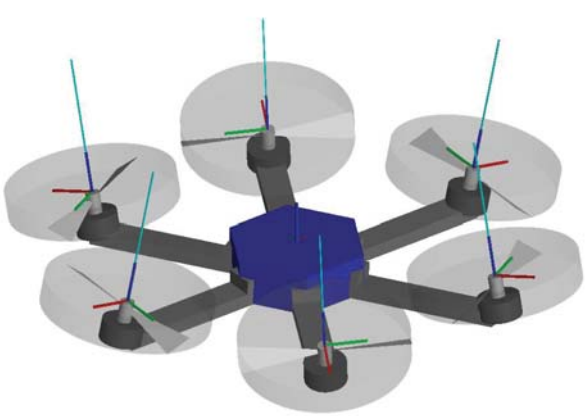

(a) PCTR (avg. cost: 12.6831)

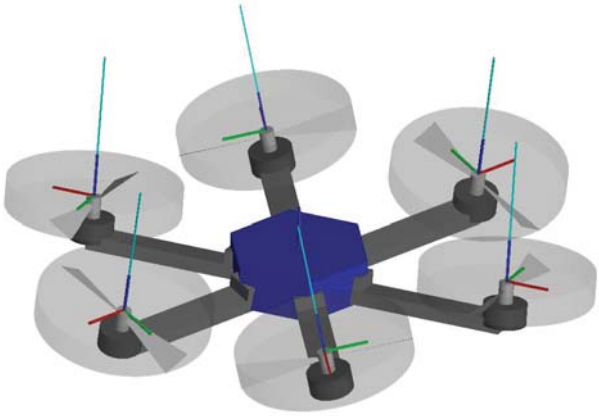

(b) SCTR (avg. cost: 12.6892)

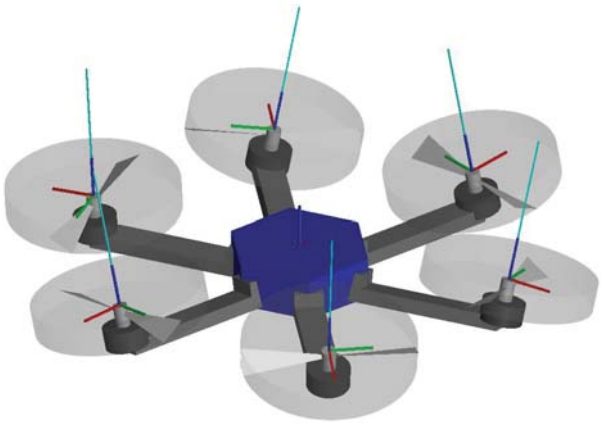

(c) GTR (avg. cost: 12.8692)

Fig. 5.11: Hexarotor structure optimized for short-distance transportation $(N, T) = (10, 1)$.

$\gamma_S = 0.1764$. The average costs for these structures are 12.6831 and 12.6892, respectively, and they are almost identical. Similar results are obtained for the short-horizon case $(N, T) = (20, 0.2)$, where $(\beta_P, \gamma_P) = (-0.0162, 0.0678)$ and $(\beta_S, \gamma_S) = (0.0019, -0.0729)$. Note that the costs cannot be compared across different conditions on the prediction horizon.

Figures 5.11 and 5.12 shows the optimal structures for the short-distance transportation scenario with $(N, T) = (10, 1)$ and $(20, 0.2)$, respectively. An important finding here is that the pose regulation does not require large rotor tilt angles even if the vehicle need to accelerate horizontally. The same conclusion can be drawn by the form of the value function (4.14) for the nongravity case discussed in Section 4.3, where the cost for the pose does not depend on the hexarotor structure.

Aerial Manipulation

Figures 5.13 and 5.14 show the optimal structures for $(N, T) = (10, 1)$ and $(20, 0.2)$, respectively. For the long-horizon case $(N, T) = (10, 1)$, we obtain the optimal structures

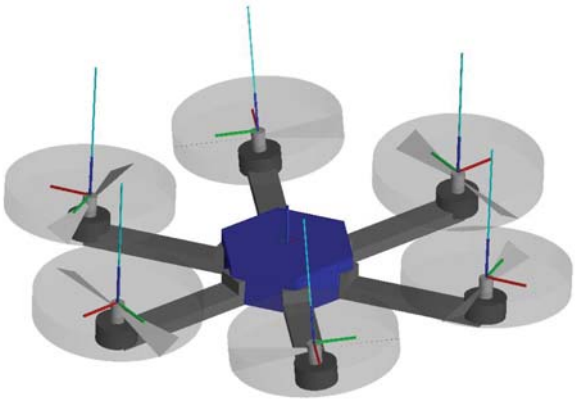

(a) PCTR (avg. cost: 31.0472)

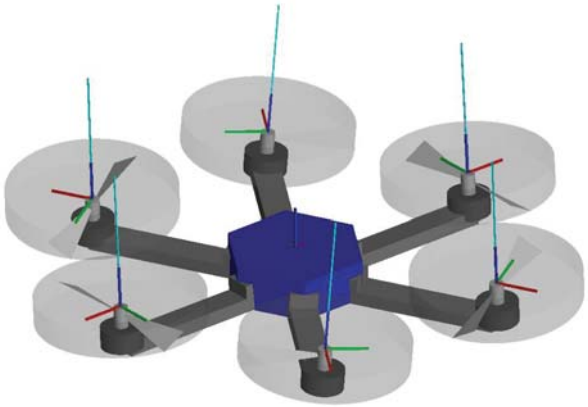

(b) SCTR (avg. cost: 31.0370)

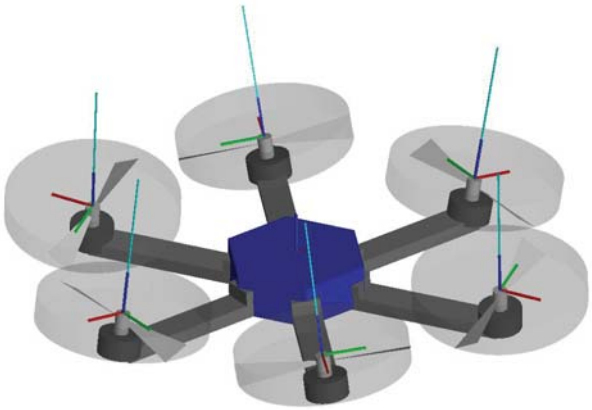

(c) GTR (avg. cost: 31.1714)

Fig. 5.12: Hexarotor structure optimized for short-distance transportation $(N, T) = (20, 0.2)$.

$(\beta_P, \gamma_P) = (0.4487, 0.1404)$ and $(\beta_S, \gamma_S) = (0.0415, -0.4550)$. Since the average costs of control are almost equal, we can select either the PCTR or SCTR optimal structure in this example. Affected by the force of gravity, the rotor tilt angles are not as large as those calculated in Section 4.3. To compensate for larger initial twist, we may need larger rotor tilt angles.

5.3.3 Discussion

Figure 5.15 shows optimal trajectories starting from the given initial states. In Fig. 5.15 (a), we can confirm that the vehicle utilizes the body tilt to accelerate towards the origin. In contrast to the conclusion of the analytical solution in Section 4.3, the optimal structure for pose control subject to the force of gravity is shown to be nearly underactuated Fig. 5.15 (b) shows that the optimal hexarotor rejects the large initial velocity by using both the body tilt and the horizontal acceleration input. Note that the conclusions here may change according

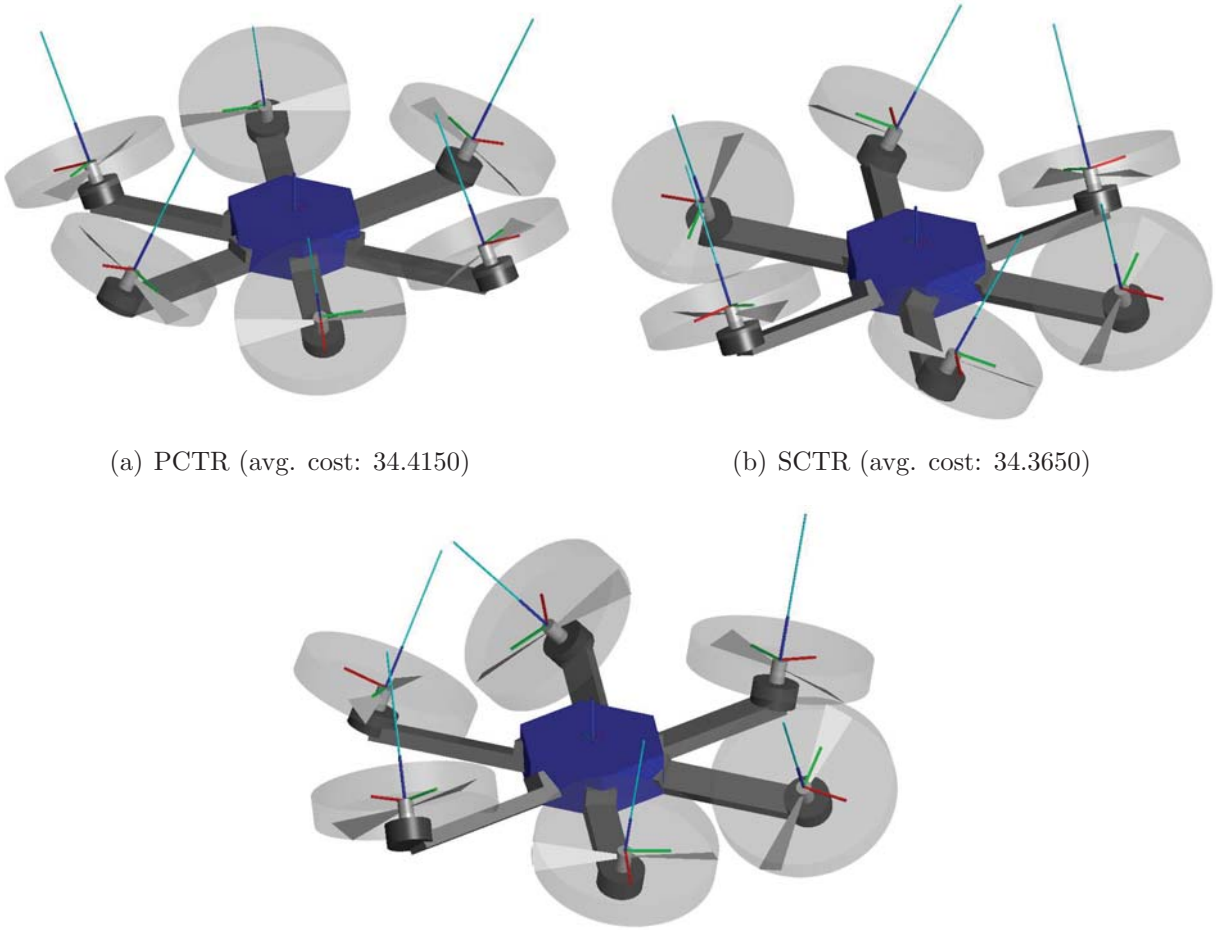

(a) PCTR (avg. cost: 34.4150)

(b) SCTR (avg. cost: 34.3650)

(c) GTR (avg. cost: 37.5608)

Fig. 5.13: Hexarotor structure optimized for aerial manipulation $(N, T) = (10, 1)$.

to the weight parameters for each element of the pose, twist, and input. These parameters are, however, considered as part of the task specification, which can be arbitrarily set to design the desired behavior.

In all the cases, the average costs of the optimized GTR structures fail to overtake those of optimal SCTR or PCTR structures, although GTR includes both SCTR and PCTR structures. This is because the convergence of the parameters is slow due to the high dimensional solution space. Larger number of the stall iterations parameter for PSO and sufficient computation time may solve this issue.

Although some structures that outperforms SCTR and PCTR structures might exist, structures without symmetry have several problems. In particular, feasibility of the control input and existence of the equilibrium input are the most critical issues. Relevant issues about the hovering ability are studied in literature such as [90] and [91]. However, it is not investigated well for structures with generically tilted rotors at present. It is also difficult to manufacture such structures since the rotors may easily interfere with other components of the vehicle.

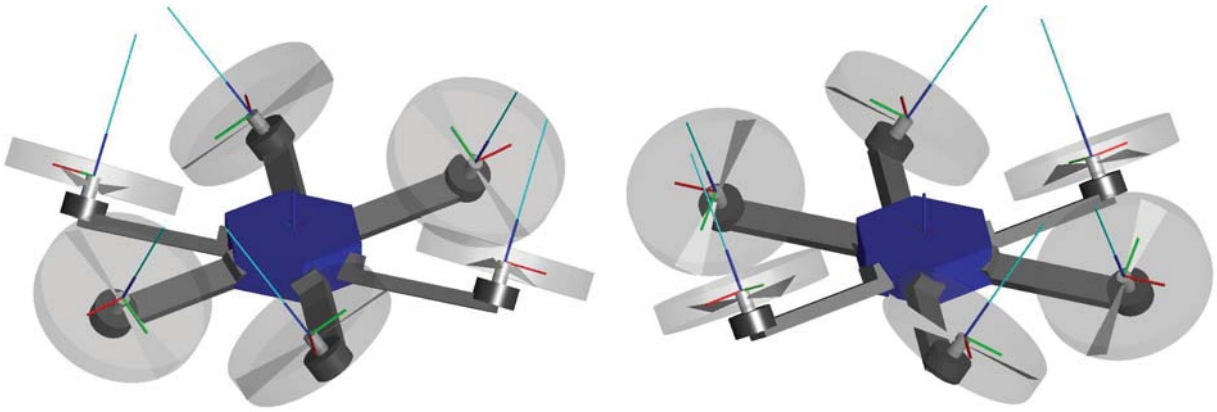

(a) PCTR (avg. cost: 42.6102)

(b) SCTR (avg. cost: 42.6216)

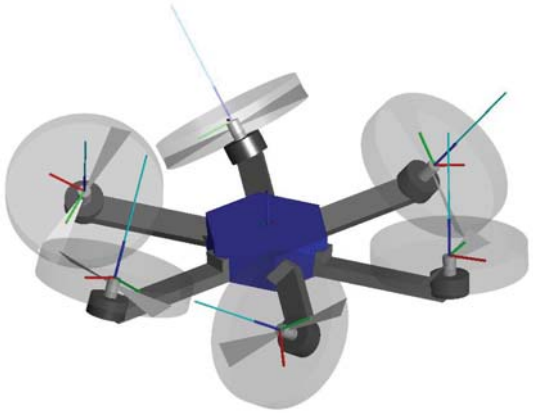

(c) GTR (avg. cost: 43.4146)

Fig. 5.14: Hexarotor structure optimized for aerial manipulation $(N, T) = (20, 0.2)$.

The proposed method is different from that of [12], where the vehicle trajectory is given, and the parameters of the control law are not optimized together with the UAV design. Our method can be compared with the previous method in [12] from the following two viewpoints:

1. The proposed method generates the optimal trajectory from the initial point, while the reference trajectory is given in the previous method.

2. The proposed method can be considered as the cost minimization of a feedback-controlled structure, while the previous method as that of a feedforward-controlled structure.

5.4 Chapter Summary

In Section 5.1, we have developed a real-time NMPC method specialized in the rigid body system. First, the Cayley map for $SE(3)$ is used to obtain a geometrically exact discrete-time dynamical model of the rigid body kinematics. Second, the recursive discretization technique

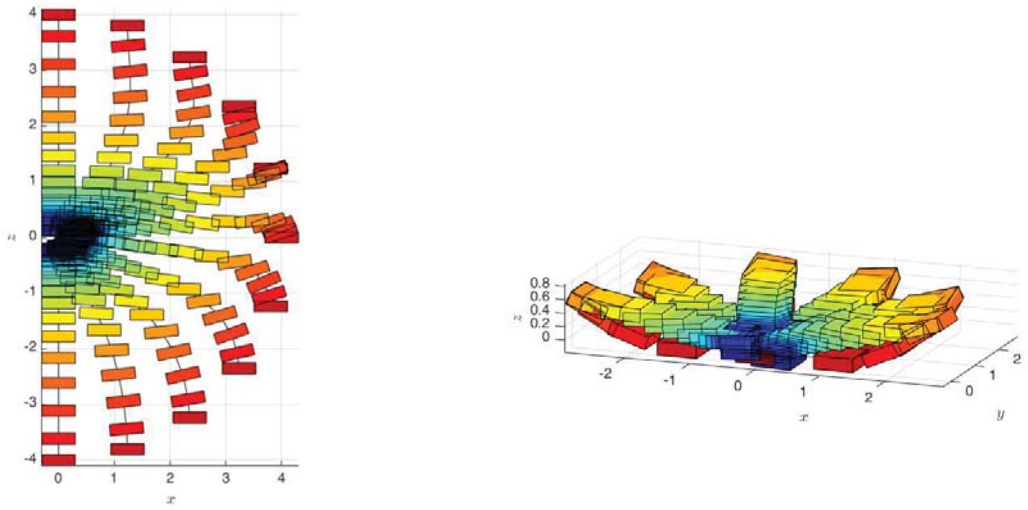

(a) Short-distance transportation (b) Aerial manipulation

Fig. 5.15: Samples of optimal trajectories. The prediction horizon is set to $(N, T) = (20, 0.2)$, and the hexarotor structures are SCTR in this figure. The colors of boxes indicate the time on the trajectories. The initial and terminal poses are illustrated with dark red and dark blue boxes, respectively.

is combined with the geometric integrator to reduce the number of decision variables of the optimal control problem while maintaining the accuracy of the solution trajectory. It is then shown that the proposed method is real-time feasible by simulations.

In Section 5.2, the proposed fast NMPC method is applied to a fully actuated hexarotor system. The experimental setup of the hexarotor flight control is described. The result shows that the proposed approach is also feasible in real time with the experimental setup considering input constraints and the force of gravity.

In Section 5.3, we reuse the fast numerical optimal control method presented in Section 5.1 to realize the idea of joint optimization of the structure and control in a numerical way. We suppose that a control task is described with an objective function of control and a set of initial states. Three different scenarios, the vertical lift-up, short-distance transportation, and aerial manipulation, are modeled as different sets of initial states. The fast optimal controller is then used to evaluate the value function, which is the minimum value of the objective function. The average value of the value function over the set of initial states is minimized with respect to the rotor tilt angles, and we have finally obtained the optimal structures for each control task in presence of the force of gravity.

Chapter 6

Conclusions

6.1 Dissertation Summary

In this dissertation, we have investigated joint optimization of the structure and control of fully actuated unmanned aerial vehicles based on minimization of the value function of the optimal control problem. The feature of the proposed method is that we can obtain the optimal control law and the optimal plant parameters simultaneously. Both analytical and numerical methods are developed in this work, and they are used to determine the optimal rotor tilt angles for different control tasks, which are specified by the objective function and the set of initial states. We have first introduced the preliminaries to rigid body dynamics and optimal control problems. Based on the fundamentals, we have defined joint optimization of the structure and control by showing simple examples of parametrized linear systems.

We have then defined a dynamical model of a fully actuated hexarotor system, which we have considered the optimization throughout this dissertation. A fully actuated hexarotor is an unmanned aerial vehicle that has fully actuated inputs for the translational and rotational motion in 3-dimensional space. The rotors are tilted and fixed, and the relation between the wrench applied to the center of mass and the rotor thrust force depends on the location and orientation of the rotors. We have shown that the nonplanar hexarotor structure can be simplified and transformed into a planar structure without changing the relation by analyzing the dynamical model. This property greatly reduces the complexity of the design optimization problem. The experimental system is introduced, and a preliminary experiment is carried out, showing that the vehicle can indeed independently generate the force and torque.

Next, we have developed an analytical method of joint optimization for a fully actuated hexarotor under zero gravity. An optimal control problem is solved via the Hamilton-Jacobi-Bellman equation, and the optimal control input is obtained analytically. We have also obtained the corresponding analytical value function, which we consider minimization with respect to plant parameters. An application to a fully actuated hexarotor shows that the

optimal design in this case corresponds to maximization of dynamic manipulability of the hexarotor. The analytical method has an advantage that it generates the optimal control input as a function of the state. Simulations show that the proposed joint optimization scheme effectively reduces the effort of control.

Since the analytical method only deals with the specific dynamical model and the objective function, we cannot consider the force of gravity acting on the vehicle when we apply the method to the hexarotor design. To remedy this issue, we have also developed a numerical method for the joint optimization problem. The optimal control problem is solved by developing an NMPC scheme tailored for the real-time control of the rigid body dynamics. We have used a geometric integrator based on the Cayley map for $SE(3)$ to reduce the number of decision variables of the finite-horizon discrete-time optimal control problem. On-board simulations and an experiment show that the present approach is feasible in real time, although the problem is comparatively complex as we consider the force of gravity and the input constraints. The optimal control method is then used to determine the optimal structure for the given control task. The approximate value function can be obtained through the optimal trajectory that is computed during NMPC, and we minimize the function for a given set of initial states with respect to the plant parameters. The result has more practical structures than that obtained by the analytical method because the numerical method explicitly considers the input cost for gravity compensation.

6.2 Future Work

The main further direction is to generalize the method to control and design multi-agent aerial vehicles systems such as a cooperative transportation system or a formation control system. For such systems, the number of design parameters increases, and the problem could be interesting because the optimal parameters could be determined in an unpredictable way. The main challenge to this future problem is the complexity of the system, which we cannot expect the analytical solution to the optimal control problem and fast computation of numerical methods with the current approach. These issues should be solved with technical improvements.

From the technical aspect, we have several issues to be tackled. One of them is generalization of the analytical optimal controller on $SE(3)$ presented in Section 4.2. We have shown the analogy to the LQR controller, which might be helpful to tackle this problem. Moreover, a stability analysis and further performance improvements of the numerical optimal controller should be tackled. Although the stabilizing constraint approach discussed in [38] could be applied to our system, we need to explicitly consider the external force of gravity, which constantly inhibits the system dynamics from stabilizing. The computational performance can be improved for a long prediction horizon by combining present approach with lower time-complexity algorithms such as the C/GMRES method [85] or differential

dynamic programming approach [86]. Furthermore, we can incorporate nonuniform sampling periods for the prediction horizon, as discussed in [87] and [88], to evaluate the system dynamics finely in the transient state and coarsely in the steady state.

Bibliography

[1] Japan's Ministry of Economics and Industry. Strucural change in economical society and policy challenges by 2050 (in japanese). `https://www.meti.go.jp/shingikai/sankoshin/2050_keizai/pdf/001_04_00.pdf`, accessed 2020-01-20.

[2] Japan's Ministry of Health, Labour and Welfare. Occupational injury statistics (in japanese). `https://www.mhlw.go.jp/bunya/roudoukijun/anzeneisei11/rousai-hassei/`, accessed 2020-01-20.

[3] R. Jannoura, K. Brinkmann, D. Uteau, C. Bruns, and R.G. Joergensen. Monitoring of crop biomass using true colour aerial photographs taken from a remote controlled hexacopter. *Biosystems Engineering*, Vol. 129, pp. 341–351, 2015.

[4] D. Roca, S. Lagüela, L. Díaz-Vilariño, J. Armesto, and P. Arias. Low-cost aerial unit for outdoor inspection of building fa cades. *Automation in Construction*, Vol. 36, pp. 128–135, 2013.

[5] G. Heredia, A.E. Jimenez-Cano, I. Sanchez, D. Llorente, V. Vega, J. Braga, J.A. Acosta, and A. Ollero. Control of a multirotor outdoor aerial manipulator. In *Proc. of the 2014 IEEE/RSJ International Conference on Intelligent Robots and Systems*, pp. 3417–3422, 2014.

[6] H.W. Wopereis, T.D. van der Molen, T.H. Post, S. Stramigioli, and M. Fumagalli. Mechanism for perching on smooth surfaces using aerial impacts. In *Proc. of the 2016 IEEE International Symposium on Safety, Security, and Rescue Robotics*, pp. 154–169, 2016.

[7] H. Yang and D. Lee. Dynamics and control of quadrotor with robotic manipulator. In *Proc. of the 2014 IEEE International Conference on Robotics and Automation*, pp. 5544–5549, 2014.

[8] G. Jiang and R. Voyles. A nonparallel hexrotor UAV with faster response to disturbances for precision position keeping. In *Proc. of the 2014 IEEE International Symposium on Safety, Security and Rescue Robotics*, 2014.

[9] J.I. Giribet, R.S. Sánchez-Peña, and A.S. Ghersin. Analysis and design of a tilted rotor hexacopter for fault tolerance. *IEEE Transactions on Aerospace and Electronic Systems*, Vol. 52, No. 4, pp. 1555–1567, 2016.

[10] D. Toratani. Research and development of double tetrahedron hexa-rotorcraft (Dot-HR). In *Proc. of the 28th Congress of the International Council of the Aeronautical Sciences*, 2012.

[11] D. Kotarski, P. Piljek, and M. Krznar. Mathematical modelling of multirotor UAV. *International Journal of Theoretical and Applied Mechanics*, Vol. 1, pp. 233–238, 2016.

[12] S. Rajappa, M. Ryll, H.H. Bülthoff, and A. Franchi. Modeling, control and design optimization for a fully-actuated hexarotor aerial vehicle with tilted propellers. In *Proc. of the 2015 IEEE International Conference on Robotics and Automation*, pp. 4006–4013, 2015.

[13] K. Okuma, D. Iwakura, K. Nonami, and D. Fujiwara. Analysis and design of nonplanar hexarotor helicopter [in Japanese]. In *Proc. of the Robotics and Mechatronics Conference 2013*, 2013.

[14] H. Mehmood, T. Nakamura, and E.N. Johnson. A maneuverability analysis of a novel hexarotor UAV concept. In *Proc. of the 2016 International Conference on Unmanned Aircraft Systems*, pp. 437–446, 2016.

[15] H. Mehmood and E.N. Johnson. A daisy-chain control design for a multirotor UAV with direct force capabilities. In *Proc. of the 2017 AIAA Guidance Navigation, and Control Conference*, 2017.

[16] B. Crowther, A. Lanzon, M. Maya-Gonzalez, and D. Langkamp. Kinematic analysis and control design for a nonplanar multirotor vehicle. *Journal of Guidance, Control, and Dynamics*, Vol. 34, No. 4, pp. 1157–1171, 2011.

[17] E. Kaufman, K. Caldwell, D. Lee, and T. Lee. Design and development of a free-floating hexrotor UAV for 6-DOF maneuvers. In *Proc. of the 2014 IEEE Aerospace Conference*, 2014.

[18] T. Shimizu, S. Suzuki, T. Kawamura, H. Ueno, and H. Murakami. Proposal of 6DOF multicopter and verification of its controllability. In *Proc. of the SICE Annual Conference 2015*, pp. 810–815, 2015.

[19] B. Convens, K. Merckaert, M.M. Nicotra, R. Naldi, and E. Garone. Control of fully actuated unmanned aerial vehicles with actuator saturation. In *Proc. of the 20th World Congress of the International Federation of Automatic Control*, pp. 13254–13259, 2017.

[20] S. Park, J. Her, J. Kim, and D. Lee. Design, modeling and control of omni-directional aerial robot. In *Proc. of the 2016 IEEE/RSJ International Conference on Intelligent Robots and Systems*, pp. 1570–1575, 2016.

[21] M. Ryll, G. Muscio, F. Pierri, E. Cataldi, G. Antonelli, F. Caccavale, and A. Franchi. 6D physical interaction with a fully actuated aerial robot. In *Proc. of the 2017 IEEE International Conference on Robotics and Automation*, pp. 5190–5195, 2017.

[22] K. Kiso, T. Ibuki, M. Yasuda, and M. Sampei. Structural optimization of hexrotors based on dynamic manipulability and the maximum translational acceleration. *Proc. of the 2015 IEEE Multi-Conference on Systems and Control*, pp. 774–779, 2015.

[23] Y. Tadokoro, T. Ibuki, and M. Sampei. Maneuverability analysis of a fully-actuated hexrotor UAV considering tilt angles and arrangement of rotors. In *Proc. of the 20th World Congress of the International Federation of Automatic Control*, pp. 9311–9316, 2017.

[24] Y. Tadokoro, T. Ibuki, and M. Sampei. Dynamic manipulability analysis and design optimization of a fully-actuated hexrotor UAV with symmetric-coplanar-tilted-rotor structure. *Transactions of Society of Instrument and Control Engineers*, Vol. 53, No. 8, pp. 480–489, 2017. (in Japanese).

[25] Y. Tadokoro, T. Ibuki, and M. Sampei. Classification and structural evaluation of fully-actuated hexrotor UAVs. In *Proc. of the 2018 American Control Conference*, pp. 1945–1950, 2018.

[26] F. Bullo and R.M. Murray. Proportional derivative (PD) control on the Euclidean group. In *Proc. of 3rd European Control Conference*, pp. 1091–1097, 1995.

[27] T. Lee, M. Leok, and N.H. McClamroch. Geometric tracking control of a quadrotor UAV on SE(3). In *Proc. of the 49th IEEE Conference on Decision and Control*, pp. 5420–5425, 2010.

[28] J. Baillieul. Geometric methods for nonlinear optimal control problems. *Journal of Optimization Theory and Applications*, Vol. 25, No. 4, pp. 519–548, 1978.

[29] A.M. Bloch, J. Baillieul, P. Crouch, and J. Marsden. *Nonholonomic Mechanics and Control*. Springer-Verlag, 2003.

[30] T. Lee, M. Leok, and N.H. McClamroch. Optimal attitude control of a rigid body using geometrically exact computations on SO(3). *Journal of Dynamical and Control Systems*, Vol. 14, No. 4, pp. 465–487, 2008.

[31] C. Liu, S. Tang, and J. Guo. Intrinsic optimal control for mechanical systems on Lie group. *Advances in Mathematical Physics*, Vol. 2017, pp. 1–8, 2017. Article ID: 6302430.

[32] Y. Tadokoro, T. Ibuki, and M. Sampei. Joint optimization of geometric control and structure of a fully-actuated hexrotor based on an analytic HJBE solution. In *Proc. of the 57th IEEE Conference on Decision and Control*, pp. 1186–1191, 2018.

[33] F. Bullo and R.M. Murray. Proportional derivative (PD) control on the Euclidean group. *CDS Technical Report*, Vol. 95, , 1995.

[34] E. Hairer, C. Lubich, and G. Wanner. *Geometric Numerical Integration*. Springer Verlag, 2nd edition, 2006.

[35] T. Lee, M. Leok, and N.H. McClamroch. Computational geometric optimal control of rigid bodies. *Communications in Information and Systems*, Vol. 8, No. 4, pp. 435–462, 2008.

[36] M. Kobilarov and J.E. Marsden. Discrete geometric optimal control on Lie groups. *IEEE Transactions on Robotics*, Vol. 27, No. 4, pp. 641–655, 2011.

[37] M. Kobilarov. Discrete optimal control on Lie groups and applications to robotic vehicles. In *Proc. of the 2014 IEEE International Conference on Robotics and Automation*, pp. 5523–5529, 2014.

[38] L. Grüne and J. Pannek. *Nonlinear Model Predictive Control*. Springer Verlag, 2011.

[39] J.M. Selig. Cayley maps for SE(3). In *Proc. of the 12th IFToMM World Congress*, 2007.

[40] M. Mehndiratta and E. Kayacan. Reconfigurable fault-tolerant NMPC for Y6 coaxial tricopter with complete loss of one rotor. In *Proc. of 2018 IEEE Conference on Control Technology and Applications*, pp. 774–780, 2018.

[41] R. Quirynen, K. Berntorp, and S. Di Cairano. Embedded optimization algorithms for steering in autonomous vehicles based on nonlinear model predictive control. In *Proc. of the 2018 American Control Conference*, pp. 3251–3256, 2018.

[42] I.K. Erunsal, A. Martinoli, and R. Ventura. Decentralized nonlinear model predictive control for 3D formation of multirotor micro aerial vehicles with relative sensing and estimation. In *Proc. of 2019 International Symposium on Multi-Robot and Multi-Agent Systems*, pp. 176–178, 2019.

[43] E. Rossi, M. Bruschetta, R. Carli, Y. Chen, and M. Farina. Online nonlinear model predictive control for tethered UAVs to perform a safe and constrained maneuver. In *Proc. of 18rd European Control Conference*, pp. 3996–4001, 2019.

[44] J. Dentler. *Real-time Model Predictive Control of Cooperative Aerial Manipulation*. PhD thesis, University of Luxembourg, 2018.

[45] M. Kamel, M. Burri, and R. Siegwart. Linear vs nonlinear MPC for trajectory tracking applied to rotary wing micro aerial vehicles. In *Proc. of the 20th World Congress of the International Federation of Automatic Control*, pp. 3463–3469, 2017.

[46] D. Bicego, J. Mazzetto, R. Carli, M. Farina, and A. Franchi. Nonlinear model predictive control with actuator constraints for multi-rotor aerial vehicles. 2019. arXiv:1911.08183 [cs.RO].

[47] G. Garimella and M. Kobilarov. Towards model-predictive control for aerial pick-and-place. In *Proc. of the 2015 IEEE International Conference on Robotics and Automation*, pp. 4692–4697, 2015.

[48] G. Garimella, M. Sheckells, and M. Kobilarov. Robust obstacle avoidance for aerial platforms using adaptive model predictive control. In *Proc. of the 2017 IEEE International Conference on Robotics and Automation*, pp. 5876–5882, 2017.

[49] N.S. Khot, V.B. Venkayya, and F.E. Eastep. Optimal structural modifications to enhance the active vibration control of flexible structures. *AIAA Journal*, Vol. 24, No. 8, pp. 1368–1374, 1986.

[50] M. Milman, M. Salama, R.E. Scheid, R. Bruno, and J.S. Gibson. Combined control-structural optimization. *Computational Mechanics*, Vol. 8, No. 1, pp. 1–18, 1991.

[51] H. Asada, J. Park, and S. Rai. A control-configured flexible arm: Integrated structure/control design. In *Proc. of the 1991 IEEE International Conference on Robotics and Automation*, pp. 2356–2362, 1991.

[52] S. Rai. Design optimization of robots based on time optimal control. In *Proc. of the 1998 IEEE International Conference on Robotics and Automation*, pp. 913–919, 1998.

[53] T. Iwasaki, S. Hara, and H. Yamauchi. Dynamical system design from a control perspective: Finite frequency positive-realness approach. *IEEE Transactions on Automatic Control*, Vol. 48, No. 8, pp. 1337–1354, 2003.

[54] K. Hiramoto and K. Grigoriadis. Integrated design of structural and control systems with a homotopy like iterative method. In *Proc. of the 2005 American Control Conference*, pp. 2510–2515, 2005.

[55] G. Bastos Jr. and O. Brüls. An integrated control-structure design for manipulators with flexible links. In *Proc. of the IFAC Conference on Modelling, Identification and Control of Nonlinear Systems*, pp. 156–161, 2015.

[56] S. Ha, S. Coros, A. Alspach, J.M. Bern, J. Kim, and K. Yamane. Computational design of robotic devices from high-level motion specifications. *IEEE Transactions on Robotics*, Vol. 34, No. 5, pp. 1240–1251, 2018.

[57] J. Xu, P. Shi, C. Lim, C. Cai, and Y. Zou. Integrated structural parameter and robust controller design for attitude tracking maneuvers. *IEEE/ASME Transactions on Mechatronics*, Vol. 21, No. 5, pp. 2490–2498, 2016.

[58] R.M. Murray, Z. Li, and S.S. Sastry. *A Mathematical Introduction to Robotic Manipulation*. CRC Press, 1994.

[59] J. Gallier and D. Xu. Computing exponentials of skew symmetric matrices and logarithms of orthogonal matrices. *International Journal of Robotics and Automation*, Vol. 18, No. 1, pp. 10–20, 2003.

[60] H. Schaub, P. Tsiotras, and J.L. Junkins. Principal rotation representations of proper NxN orthogonal matrices. *International Journal of Engineering Science*, Vol. 33, No. 15, pp. 2277–2295, 1995.

[61] D.E. Kirk. *Optimal Control Theory: An Introduction*. Prentice Hall, 1970.

[62] J. Seddon. *Basic Helicopter Aerodynamics*. BSP Professional Books, 1990.

[63] T. Yoshikawa. Dynamic manipulability of robot manipulators. *Proc. of the 1985 IEEE International Conference of Robotics and Automation*, pp. 1033–1038, 1985.

[64] J.R. Silvester. Determinants of block matrices. *The Mathematical Gazette*, Vol. 84, No. 501, pp. 460–467, 2000.

[65] HolyBro. 3DR Pixhawk Mini. `http://www.holybro.com/product/pixhawk-mini/`, accessed 2019-11-11.

[66] The MathWorks, Inc. Raspberry Pi support from Simulink - hardware support. `https://www.mathworks.com/hardware-support/raspberry-pi-simulink.html`, accessed 2019-11-11.

[67] The MathWorks, Inc. PX4 autopilots support from Embedded Coder - hardware support. `https://www.mathworks.com/hardware-support/px4-autopilots.html`, accessed 2019-11-11.

[68] Natural Point, Inc. Optitrack - motion capture system. `https://optitrack.com/`, accessed 2019-11-11.

[69] Dronecode Project. MAVLink: Marshalling / communication library for drones. `https://github.com/mavlink/mavlink`, accessed 2019-11-11.

[70] A. Saccon, J. Hauser, and A.P. Aguiar. Exploration of kinematic optimal control on the Lie group SO(3). *Proc. of the 8th IFAC Symposium on Nonlinear Control Systems*, pp. 1302–1307, 2010.

[71] P. Lancaster and L. Rodman. Existence and uniqueness theorems for the algebraic Riccati equation. *International Journal on Control*, Vol. 32, No. 2, pp. 285–309, 1979.

[72] A. Bressan. Viscocity solutions of Hamilton-Jacobi equations and optimal control problems. *Lecture Note Dept. of Math., Pennsylvania State University*, 2011.

[73] W.F. Arnold and A.J. Laub. Generalized eigenproblem algorithms and software for algebraic Riccati equations. *Proceedings of the IEEE*, Vol. 72, No. 12, pp. 1746–1754, 1984.

[74] H.K. Khalil. *Nonlinear Control*. Prentice Hall, 2015.

[75] Y. Tadokoro, Y. Taya, T. Ibuki, and M. Sampei. Nonlinear model predictive control of a fully-actuated UAV on SE(3) using acceleration characteristics of the structure. In *Proc. of the 12th Asian Control Conference*, pp. 283–288, 2019.

[76] Y. Tadokoro, Y. Taya, T. Ibuki, and M. Sampei. Real-time model predictive control of rigid body motion via discretization using the Cayley map. *IEEE Access*, Vol. 8, No. 1, pp. 17149–17159, 2020.

[77] J.M. Selig. *Geometrical Methods in Robotics*. Springer Verlag, 1996.

[78] D. Condurache and I.A. Ciureanu. Closed form of the Baker-Campbell-Hausdorff formula for the Lie algebra of rigid body displacements. In *Proc. of the 9th ECCOMAS Thematic Conference on Multibody Dynamics*, pp. 307–314, 2019.

[79] J. Solà. Quaternion kinematics for the error-state Kalman filter. 2017. arXiv:1711.02508 [cs.RO].

[80] J.R. Dooley and J.M. McCarthy. On the geometric analysis of optimum trajectories for cooperating robots using dual quaternion coordinates. In *Proc. of the 1993 IEEE International Conference on Robotics and Automation*, pp. 1031–1036, 1993.

[81] J. Nocedal. Updating quasi-Newton matrices with limited storage. *Mathematics of Computation*, Vol. 35, No. 151, pp. 773–782, 1980.

[82] R.H. Byrd, P. Lu, J. Nocedal, and C. Zhu. A limited memory algorithm for bound constrained optimization. *SIAM Journal on Scientific Computing*, Vol. 16, No. 5, pp. 1190–1208, 1995.

[83] S.G. Johnson. The NLopt nonlinear-optimization package. `http://github.com/stevengj/nlopt`, accessed 2019-09-25.

[84] T. Lee, N.H. McClamroch, and M. Leok. Optimal control of a rigid body using geometrically exact computations on SE(3). In *Proc. of the 45th IEEE Conference on Decision and Control*, pp. 2710–2715, 2006.

[85] T. Ohtsuka. A continuation/GMRES method for fast computation of nonlinear receding horizon control. *Automatica*, Vol. 40, No. 4, pp. 563–574, 2004.

[86] Y. Tassa, N. Mansard, and E. Todorov. Control-limited differential dynamic programming. In *Proc. of the 2014 IEEE International Conference on Robotics and Automation*, pp. 1168–1175, 2014.

[87] Y. Cao and W. Chen. Variable sampling-time nonlinear model predictive control of satellites using magneto-torquers. *Systems Science & Control Engineering*, Vol. 2, pp. 773–782, 2014.

[88] O. Gomozov, J.P.F. Trovão, X. Kestelyn, and M.R. Dubois. Adaptive energy management system based on a real-time model predictive control with nonuniform sampling time for multiple energy storage electric vehicle. *IEEE Transactions on Vehicular Technology*, Vol. 66, No. 7, pp. 5520–5530, 2017.

[89] J. Kennedy and R. Eberhart. Particle swarm optimization. In *Proc. of IEEE International Conference on Neural Networks*, Vol. IV, pp. 1942–1948, 1995.

[90] G. Michieletto, M. Ryll, and A. Franchi. Fundamental actuation properties of multirotors: Force-moment decoupling and fail-safe robustness. *IEEE Transactions on Robotics*, Vol. 34, No. 3, pp. 702–715, 2018.

[91] R. Matsuda, T. Ibuki, and M. Sampei. A hoverability analysis method for multirotor uavs with a case study on fault tolerance. In *Proc. of the 57th IEEE Conference on Decision and Control*, pp. 4264–4269, 2018.

Publications

Journal Papers

[1] Yuichi Tadokoro, Tatsuya Ibuki and Mitsuji Sampei. Dynamic Manipulability Analysis and Design Optimization of a Fully-actuated Hexrotor UAV with Symmetric-Coplanar-Tilted-Rotor Structure. *Transactions of Society of Instrument and Control Engineers*, Vol. 53, No. 8, pp. 480–489, 2017. [Sections 3.1 and 3.3]

[2] Yuichi Tadokoro, Yuki Taya, Tatsuya Ibuki and Mitsuji Sampei. Real-time Model Predictive Control of Rigid Body Motion via Discretization Using the Cayley Map. *IEEE Access*, Vol. 8, No. 1, pp. 17149–17159, 2020. [Chapter 5]

Refereed Conference Papers

[1] Y. Tadokoro, T. Ibuki and M. Sampei. Maneuverability Analysis of a Fully-Actuated Hexrotor UAV Considering Tilt Angles and Arrangement of Rotors. In *Proc. of the IFAC World Congress 2017*, pp. 1833–1838, Toulouse, France, 2017. [Sections 3.1 and 3.3]

[2] Y. Tadokoro, T. Ibuki and M. Sampei. Classification and Structural Evaluation of Fully-Actuated Hexrotor UAVs. In *Proc. of the 2018 American Control Conference*, pp. 1945–1950, Milwaukee, Wisconsin, USA, 2018. [Sections 3.2 and 3.3]

[3] Y. Tadokoro, T. Ibuki and M. Sampei. Joint Optimization of Geometric Control and Structure of a Fully-actuated Hexrotor based on an Analytic HJBE Solution. In *Proc. of the 57th IEEE Conference on Decision and Control*, pp. 1186–1191, Miami Beach, Florida, USA, 2018. [Chapter 4]

[4] Y. Tadokoro, Y. Taya, T. Ibuki and M. Sampei. Nonlinear Model Predictive Control of a Fully-actuated UAV on SE(3) using Acceleration Characteristics of the Structure. In *Proc. of the 12th Asian Control Conference*, pp. 283–288, Kitakyushu, Japan, 2019. [Section 5.1]

Other Publications (Refereed Conference Papers)

[1] R. Matsuda, Y. Tadokoro, T. Ibuki and M. Sampei. Experimental Verification of Inverse Optimal Control for Inverted Pendulum Stabilization on a Quadrotor. In *SICE Annual Conference 2016*, 2016.

[2] K. Nitta, K. Higuchi, Y. Tadokoro and J. Rekimoto. Shepherd Pass: Ability Tuning for Augmented Sports using Ball-Shaped Quadcopter. In *Proc. of the 12th International Conference on Advances in Computer Entertainment Technology 2015*, No. 11, 2015.

[3] T. Ibuki, Y. Tadokoro, Y. Fujita and M. Sampei. 3D Inverted Pendulum Stabilization on a Quadrotor via Bilinear System Approximations. In *Proc. of the 2015 IEEE Multi-Conference on Systems and Control*, pp. 513–518, 2015.

Appendix A

Appendix

A.1 Mathematical Formulas

□ $x^\top Sx = 0$ **if** $S^\top = -S$

Consider an $n \times n$ skew-symmetric matrix S, and let $x \in \mathbb{R}^n$. Then, the quadratic form of x associated with S becomes zero. This property directly follows from the transpose of the scalar value

$$x^\top Sx = (x^\top Sx)^\top = -x^\top Sx = 0. \tag{A.1}$$

□ $a \times b = \widehat{a}b$

The product of a skew-symmetric matrix in $\mathfrak{so}(3)$ and a 3-dimensional real vector corresponds with the cross product of two vectors:

$$a \times b = \widehat{a}b = -\widehat{b}a, \tag{A.2}$$

where $a = [a_1\ a_2\ a_3]^\top \in \mathbb{R}^3$ and $b = [b_1\ b_2\ b_3]^\top \in \mathbb{R}^3$. In particular, $\widehat{a}a = O_{3\times 1}$ holds because $a \times a = O_{3\times 1}$.

□ **Time derivative of the logarithm map**

The time derivative of the logarithm map between the group G and the algebra $\mathfrak{g}$ is calculated by the following equation [33, Theorem 2]:

$$\frac{d}{dt}\log(g) = \sum_0^\infty \frac{(-1)^n \mathrm{B}_n}{n!}\,\mathrm{ad}^n_{\log(g)}\,V^b,$$

where $g \in G$, $\{\mathrm{B}_n\}$ are the Bernoulli number, ad_X is the adjoint representation of the algebra element $X \in \mathfrak{g}$, and $V^b = \dot{g}g^{-1}$.

The explicit expression of the derivative for $SO(3)$ is known as follows [33, Lemma 3]:

$$\frac{d}{dt}\log(R) = \left(I_3 + \frac{1}{2}\log(R) + (1 - \alpha(\|\log(R)^\vee\|))\frac{\log(R)^2}{\|\log(R)^\vee\|^2}\right)\omega^b, \tag{A.3}$$

where $R \in SO(3)$, $\alpha(y) = y/2\cot(y/2)$, and $\omega^b = \dot{R}R^{-1}$.

□ $\operatorname{argmin}_x \frac{1}{2}x^\top Ax - x^\top b = A^{-1}b$

Let $x \in \mathbb{R}^n$ and $b \in \mathbb{R}^n$. Suppose that $A \in \mathbb{R}^{n\times n}$ is positive definite, and define $c(x) = \frac{1}{2}x^\top Ax - x^\top b$. Then, the necessary condition of minimum

$$\frac{\partial c(x)}{\partial x} = x^\top A - b^\top = 0, \tag{A.4}$$

yields $x = A^{-1}b$. At this point x, $c(x)$ takes minimum value because of the convexity.

A.2 Decomposed DMM

In Theorem 3.3, we have shown that the DMM of the hexarotor with SCTR or PCTR structure at the special output point can be decomposed in to elements about six translational and rotational axes. The following are the explicit forms of the elements: For SCTR structure, the decomposed DMMs are

$$\begin{aligned}
\sigma_{tx}^2 = \sigma_{ty}^2 &= \frac{3(\kappa^2 A^2 + r^2\,\mathrm{C}_{\beta_S}^2\,\mathrm{C}_{\gamma_S}^2\,\mathrm{S}_{\gamma_S}^2 + \kappa A r\,\mathrm{C}_{\beta_S}\,\mathrm{S}_{2\gamma_S})}{m^2(\kappa^2 A + r^2\,\mathrm{C}_{\beta_S}^2\,\mathrm{C}_{\gamma_S}^2 + \kappa r\,\mathrm{C}_{\beta_S}\,\mathrm{S}_{2\gamma_S})},\\
\sigma_{tz}^2 &= \frac{6\,\mathrm{C}_{\beta_S}^2\,\mathrm{C}_{\gamma_S}^2}{m^2},\\
\sigma_{rx}^2 = \sigma_{ry}^2 &= \frac{3(\kappa^2 A + r^2\,\mathrm{C}_{\beta_S}^2\,\mathrm{C}_{\gamma_S}^2 + \kappa r\,\mathrm{C}_{\beta_S}\,\mathrm{S}_{2\gamma_S})}{\mathcal{I}_h^2},\\
\sigma_{rz}^2 &= \frac{6(r^2\,\mathrm{S}_{\gamma_S}^2 + \kappa^2\,\mathrm{C}_{\beta_S}^2\,\mathrm{C}_{\gamma_S}^2 - \kappa r\,\mathrm{C}_{\beta_S}\,\mathrm{S}_{2\gamma_S})}{\mathcal{I}_v^2},
\end{aligned}$$

where $A = (1 - \mathrm{C}_{\beta_S}^2\,\mathrm{C}_{\gamma_S}^2)$. Likewise, we have the following elements for PCTR structure:

$$\begin{aligned}
\sigma_{tx}^2 = \sigma_{ty}^2 &= \frac{3(1 - \mathrm{C}_{\beta_P}^2\,\mathrm{C}_{\gamma_P}^2)}{m^2},\\
\sigma_{tz}^2 &= \frac{6\,\mathrm{C}_{\beta_P}^2\,\mathrm{C}_{\gamma_P}^2}{m^2},\\
\sigma_{rx}^2 = \sigma_{ry}^2 &= \frac{3(\kappa^2(1 - \mathrm{C}_{\beta_P}^2\,\mathrm{C}_{\gamma_P}^2) + r^2\,\mathrm{C}_{\beta_P}^2\,\mathrm{C}_{\gamma_P}^2 + \kappa r\,\mathrm{C}_{\beta_P}\,\mathrm{S}_{2\gamma_P})}{\mathcal{I}_h^2},\\
\sigma_{rz}^2 &= \frac{6(r^2\,\mathrm{S}_{\gamma_P}^2 + \kappa^2\,\mathrm{C}_{\beta_P}^2\,\mathrm{C}_{\gamma_P}^2 - \kappa r\,\mathrm{C}_{\beta_P}\,\mathrm{S}_{2\gamma_P})}{\mathcal{I}_v^2}.
\end{aligned}$$

These equations are obtained by direct calculation.

A.3 Derivation of the Analytical Optimal Controller

First, we consider the candidate of the value function as follows:

$$U = \begin{bmatrix} q \\ V \end{bmatrix}^\top \begin{bmatrix} K_{11} & K_{12} \\ K_{12} & K_{22} \end{bmatrix} \begin{bmatrix} q \\ V \end{bmatrix}.$$

This candidate has a similar form as the objective function. We assume that the matrices $K_{11}, K_{12}, K_{22} \in \mathbb{R}^{3\times 3}$ are block diagonal and positive definite.

$$K_{11} = \begin{bmatrix} K_{11\mathrm{T}} & O_3 \\ O_3 & K_{11\mathrm{R}} \end{bmatrix},\ K_{12} = \begin{bmatrix} K_{12\mathrm{T}} & O_3 \\ O_3 & K_{12\mathrm{R}} \end{bmatrix},\ K_{22} = \begin{bmatrix} K_{22\mathrm{T}} & O_3 \\ O_3 & K_{22\mathrm{R}} \end{bmatrix}$$

The feedforward input term regarding the internal drift is assumed to take the following form:

$$u_{ff} = \begin{bmatrix} K_M^{-1}\widehat{\omega}(K_M v) \\ -\frac{1}{2}K_J^{-1}\widehat{\omega}(K_J\omega) + \frac{1-\alpha(\|\psi\|)}{\|\psi\|^2}K_J^{-1}\left((\widehat{\psi}\omega)^\wedge(K_J\omega)\right) \end{bmatrix},$$

where K_M and K_J are positive definite matrices, and

$$\frac{dV}{dt} = u_c - u_{ff}.$$

Now, we calculate the components of the derivative of the value function candidate one

by one.

$$
\begin{aligned}
V^\top K_{12}\frac{dq}{dt} &= \|V\|^2_{K_{12}} - v^\top K_{12\mathrm{T}}\widehat{\omega}R^\top p - \frac{1}{2}\omega^\top K_{12\mathrm{R}}\widehat{\psi}\omega + \frac{1-\alpha(\|\psi\|)}{\|\psi\|^2}\omega^\top K_{12\mathrm{R}}\widehat{\psi}^2\omega \\
q^\top K_{12}\frac{dV}{dt} &= q^\top K_{12}u_c - p^\top RK_{12\mathrm{T}}K_M^{-1}\widehat{\omega}(K_M v) + \frac{1}{2}\psi^\top K_{12\mathrm{R}}K_J^{-1}\widehat{\omega}(K_J\omega) \\
&\quad + \frac{1-\alpha(\|\psi\|)}{\|\psi\|^2}\psi^\top K_{12\mathrm{R}}K_J^{-1}\left((\widehat{\omega}\psi)^\wedge(K_J\omega)\right) \\
&= q^\top K_{12}u_c + v^\top K_M\widehat{\omega}(K_M^{-1}K_{12\mathrm{T}}R^\top p) + \frac{1}{2}\omega^\top K_J(K_J^{-1}K_{12\mathrm{R}}\psi)^\wedge\omega \\
&\quad - \frac{1-\alpha(\|\psi\|)}{\|\psi\|^2}\omega^\top K_J(K_J^{-1}K_{12\mathrm{R}}\psi)^\wedge(\widehat{\psi}\omega) \\
q^\top K_{11}\frac{dq}{dt} &= q^\top K_{11}V - p^\top RK_{11\mathrm{T}}\widehat{\omega}R^\top p - \frac{1}{2}\psi^\top K_{11\mathrm{R}}\widehat{\psi}\omega + \frac{1-\alpha(\|\psi\|)}{\|\psi\|^2}\psi^\top K_{11\mathrm{R}}\widehat{\psi}^2\omega \\
V^\top K_{22}\frac{dV}{dt} &= V^\top K_{22}u_c - v^\top K_{22\mathrm{T}}K_M^{-1}\widehat{\omega}(K_M v) + \frac{1}{2}\omega^\top K_{22\mathrm{R}}K_J^{-1}\widehat{\omega}(K_J\omega) \\
&\quad + \frac{1-\alpha(\|\psi\|)}{\|\psi\|^2}\omega^\top K_{22\mathrm{R}}K_J^{-1}\left((\widehat{\omega}\psi)^\wedge(K_J\omega)\right) \\
&= V^\top K_{22}u_c - (K_M^{-1}K_{22\mathrm{T}}v)^\top\widehat{\omega}(K_M v) + \frac{1}{2}(K_J^{-1}K_{22\mathrm{R}}\omega)^\top\widehat{\omega}(K_J\omega) \\
&\quad + \frac{1-\alpha(\|\psi\|)}{\|\psi\|^2}(\widehat{\omega}\psi)^\top\left((K_J\omega)^\wedge(K_J^{-1}K_{22\mathrm{R}}\omega)\right)
\end{aligned}
$$

Here, we have used (A.2) to swap the order of the cross product. We then utilize (A.1) to obtain the conditions on matrices K_{11}, K_{12}, and K_{22} to eliminate higher order terms of ψ and V. The conditions are summarized below.

$$
V^\top K_{12}\frac{dq}{dt} + q^\top K_{12}\frac{dV}{dt} = \|V\|^2_{K_{12}} + q^\top K_{12}u_c \quad \text{if} \quad K_{12} = \begin{bmatrix} aK_M & O_3 \\ O_3 & bK_J \end{bmatrix} \tag{A.5}
$$

$$
V^\top K_{22}\frac{dV}{dt} = V^\top K_{22}u_c \quad \text{if} \quad K_{22} = \begin{bmatrix} cK_M^2 & O_3 \\ O_3 & dK_J^2 \end{bmatrix} \tag{A.6}
$$

$$
q^\top K_{11}\frac{dq}{dt} = q^\top K_{11}V \quad \text{if} \quad K_{11} = \begin{bmatrix} eI_3 & O_3 \\ O_3 & fI_3 \end{bmatrix} \tag{A.7}
$$

We assume that these conditions hold.

We now have the Hamiltonian of this optimal control problem

$$
\begin{aligned}
H &= L + \frac{dU}{dt} \\
&= \frac{1}{2}q^\top Q_p q + \frac{1}{2}V^\top Q_v V + \frac{1}{2}u_c^\top Q_u u_c + V^\top K_{12} + q^\top K_{12}u_c + V^\top K_{22}u_c + q^\top K_{11}V,
\end{aligned}
$$

and the corresponding optimal control input is

$$u_c^* = -Q_u^{-1}\left(K_{12}q + K_{22}V\right).$$

By plugging this input back into the original Hamiltonian, we obtain the HJB equation as follows:

$$\begin{aligned} H = &\frac{1}{2}q^\top Q_p q + \frac{1}{2}V^\top Q_v V + \frac{1}{2}q^\top K_{12}^2 Q_u^{-1} q + \frac{1}{2}V^\top K_{22}^2 Q_u^{-1} V + q^\top K_{12}K_{22}Q_u^{-1}V + V^\top K_{12}V \\ &- q^\top K_{12}Q_u^{-1}K_{12}q - q^\top K_{12}K_{22}Q_u^{-1}V - V^\top K_{22}Q_u^{-1}K_{12}q - V^\top K_{22}Q_u^{-1}K_{22}V + q^\top K_{11}V \\ = &\frac{1}{2}q^\top\left(Q_p + K_{12}^2Q_u^{-1} - 2K_{12}^2Q_u^{-1}\right)q + \frac{1}{2}V^\top\left(Q_v + K_{22}^2Q_u^{-1} + 2K_{12} - 2K_{22}^2Q_u^{-1}\right)V \\ &+ q^\top\left(K_{12}K_{22}Q_u^{-1} - K_{12}K_{22}Q_u^{-1} - K_{22}Q_u^{-1}K_{12} + K_{11}\right)V \\ = &\,0. \end{aligned}$$

This equation yields the following three conditions:

$$\begin{aligned} Q_p - K_{12}^2Q_u^{-1} &= 0 \\ Q_d + 2K_{12} - K_{22}^2Q_u^{-1} &= 0 \\ K_{11} - K_{12}K_{22}Q_u^{-1} &= 0. \end{aligned}$$

From the assumptions (A.5), (A.6), and (A.7), we obtain

$$Q_p - \begin{bmatrix} a^2K_M^2 & O_3 \\ O_3 & b^2K_J^2 \end{bmatrix} Q_u^{-1} = 0 \tag{A.8}$$

$$Q_d + \begin{bmatrix} 2aK_M - c^2K_M^4 & O_3 \\ O_3 & 2bK_J - d^2K_J^4 \end{bmatrix} Q_u^{-1} = 0 \tag{A.9}$$

$$\begin{bmatrix} eI_3 & O_3 \\ O_3 & fI_3 \end{bmatrix} - \begin{bmatrix} acK_M^3 & O_3 \\ O_3 & bdK_J^3 \end{bmatrix} Q_u^{-1} = 0. \tag{A.10}$$

Additionally, if

$$\begin{bmatrix} K_M^3 & O_3 \\ O_3 & K_J^3 \end{bmatrix} = Q_u,$$

the closed-form solution of the system of equations can be calculated.

From (A.10), we obtain

$$\begin{bmatrix} eI_3 & O_3 \\ O_3 & fI_3 \end{bmatrix} - \begin{bmatrix} acI_3 & O_3 \\ O_3 & bdI_3 \end{bmatrix} Q_u Q_u^{-1} = 0,$$

and this yields

$$e = ac,\ f = bd.$$

The condition (A.9) yields

$$Q_d = \begin{bmatrix} (c^2 - 2a)I_3 & O_3 \\ O_3 & (d^2 - 2b)I_3 \end{bmatrix} \begin{bmatrix} K_M & O_3 \\ O_3 & K_J \end{bmatrix},$$

and similarly, we obtain from (A.8) that

$$Q_p = \begin{bmatrix} a^2 I_3 & O_3 \\ O_3 & b^2 I_3 \end{bmatrix} \begin{bmatrix} K_M^{-1} & O_3 \\ O_3 & K_J^{-1} \end{bmatrix}.$$

By setting $a = b = 1$ and $c = d = e = f = \sqrt{3}$, we finally acquire the closed-form value function

$$U = \frac{1}{2} \begin{bmatrix} q \\ V \end{bmatrix}^\top \begin{bmatrix} \sqrt{3} I_6 & Q_u^{\frac{1}{3}} \\ Q_u^{\frac{1}{3}} & \sqrt{3} Q_u^{\frac{2}{3}} \end{bmatrix} \begin{bmatrix} q \\ V \end{bmatrix}.$$

All the assumptions used in the derivation are made in order to obtain the closed-form solution.